**From the holdings of the Department of Special Collections , Princeton University Library, Princeton, NJ**

These documents are either in the public domain, or can only be used for educational and research purposes (Fair use) as per U.S. Copyright law (text below). By accessing this file, all users agree that their use falls in the public domain or within fair use as defined by the copyrightlaw. We do not charge any permission or usage fees for the publication of images of material inour collections, including those provided by Princeton University Library, via our website, catalog, or directly from staff.For more information regarding copyright, credit, and citation please review the information onthe Copyright, Credit and Citation Guidelines page of our website.
https://library.princeton.edu/special-collections/policies/copyright-credit-and-citation-guidelines. If you have any questions, including how to order higher-quality images from the collection, contact Special Collections Public Services via our Ask Us! Form. https://library.princeton.edu/special-collections/ask-us

---

Doctoral Dissertations, 2011-2026 Atmospheric and Oceanic Sciences

2018

# Parameterizing the Melting of Icebergs in Global Climate Models

FitzMaurice, Anna

Princeton, NJ : Princeton University

---

http://arks.princeton.edu/ark:/88435/dsp01x920g055m

*U.S. Copyright law: The copyright law of the United States (Title 17, §108, United States Code) governs the making of photocopies or other reproductions of copyrighted material. Under certain conditions specified in the law, libraries and archives are authorized to furnish a photocopy or other reproduction. One of these specified conditions is that the photocopy or reproduction is not to be used for any purpose other than private study, scholarship, or research. If a user makes a request for, or later uses, a photocopy or reproduction for purposes in excess of fair use that user may be liable for copyright infringement. This institution reserves the right to refuse to accept a copying order if, in its judgment, fulfillment of the order would involve a violation of copyright law. https://www.copyright.gov/title17/title17.pdf*

# Parameterizing the Melting of Icebergs in Global Climate Models

Anna FitzMaurice

A Dissertation
Presented to the Faculty
of Princeton University
in Candidacy for the Degree
of Doctor of Philosophy

Recommended for Acceptance
by the Program in
Atmospheric and Oceanic Sciences
Adviser: Dr Robert Hallberg

April 2018

© Copyright by Anna FitzMaurice, 2018.

All rights reserved.

# Abstract

Icebergs account for approximately half the freshwater flux into the ocean from the polar ice sheets, and play a major role in the distribution of melt water in the ocean, but their melting is currently parameterized in a rudimentary way in global climate models. In this thesis, a combination of observations, laboratory experiments, and numerical modeling is used to suggest improved iceberg melt rate parameterizations. This work is further introduced and motivated in Chapter 1.

In Chapter 2, an observational record of icebergs in a Greenland fjord is used to show that icebergs subject to strongly sheared flows predominantly move with the vertical average of the ocean currents. If, as typical in iceberg parameterizations, only the surface ocean velocity is taken into account, iceberg speed and basal melt may have errors in excess of 60%. These results emphasize the need for parameterizations to consider ocean properties over the entire iceberg draft.

A series of laboratory experiments conducted to determine the dependence of submarine iceberg side melting on a background flow is described in Chapter 3. It is shown that two distinct regimes of melting exist depending on the flow magnitude and consequent behavior of melt plumes (side-attached or side-detached), with correspondingly different meltwater spreading characteristics. These results are subsequently extended to ice blocks melting in a two-layer vertically sheared flow.

Finally, an idealized numerical configuration is used in Chapter 4 to compare the three-equation parameterization of melt, developed for application under ice shelves, and the standardly used bulk parameterization of iceberg basal melt. The results suggest an updated velocity-independent version of this parameterization for use in calculating the basal melt rate of tabular icebergs, to account for the changes in ocean properties caused by the physical presence of a large iceberg in the ocean. The results of this thesis and their implications are discussed in Chapter 5.

# Acknowledgements

Before beginning this thesis, I would like to briefly thank those people to whom it owes its existence. Firstly, my advisors, my committee, and the AOS administrative staff for the extensive academic support they have given me. Dr Robert Hallberg for his longterm encouragement and accommodation of my academic meandering. Dr Claudia Cenedese for the countless insightful comments she made on my work and for her unwavering confidence in me. Dr Sonya Legg for her mentorship and consistently astute academic advice. Dr Fiamma Straneo for taking me on as a guest student and providing me with the direction and motivation to complete my PhD. Dr Alistair Adcroft for numerous enlightening discussions and for agreeing to read this work in its entirety.

Secondly, for something in between academic support and friendship, I would like to thank AOS post-docs Adele Morrison and Alon Stern. One at the beginning, the other at the end of my PhD, they both dedicated nontrivial amounts of their time to teach me how to be a better scientist, and help me succeed.

Lastly, I would like to thank my friends and family. I owe my thanks to so many graduate students and post-docs in the AOS department, but in particular I would like to mention Nick Lutsko, Natasha Henschke, Hannah Zanowski, and Charlotte Laufkötter for being the best harem a girl could wish for; my year, Youmi Oh and Zhaoyi Shen, for their warmth and companionship; Jon Balkind and Sid Mishra-Sharma for providing me with outside sanity; and Morgan Quimby, for getting me to take things one step at a time. Finally; my parents, brother, sister, and sister-in-law, I would like to thank for the enduring emotional support they have given me, their encouragement, their humour, and their unfailing dependability.

# Contents

Abstract . . . . . iii

Acknowledgements . . . . . iv

List of Figures . . . . . viii

**1 Introduction** **1**

1.1 Context . . . . . 1

1.2 Motivation . . . . . 3

**2 Observations: Icebergs in a Greenland Fjord** **6**

2.1 Introduction . . . . . 6

2.2 Background . . . . . 7

2.2.1 Modelling of Iceberg Motion . . . . . 7

2.2.2 Modelling of Iceberg Melt . . . . . 7

2.3 Data . . . . . 9

2.3.1 Iceberg Record . . . . . 9

2.3.2 Ocean Velocity and Wind Data . . . . . 11

2.3.3 Behavior of Icebergs in Sermilik Fjord . . . . . 14

2.4 Model . . . . . 14

2.4.1 Forcing Terms . . . . . 17

2.4.2 Iceberg Shape . . . . . 18

2.4.3 Drag Coefficients and Temporal Equilibration . . . . . 19

2.5 Results . . . 23
2.5.1 Typical Iceberg Transit Profiles . . . 23
2.5.2 Error Incurred from Neglecting Vertical Shear . . . 25
2.5.3 Discussion . . . 28
2.6 Conclusions . . . 29

**3 Laboratory Experiments: Ice Melting in a Background Flow 31**
3.1 Part I: Ice Melting in a Homogeneous Flow . . . 31
3.2 Background . . . 32
3.3 Methods . . . 34
3.3.1 Experimental Configuration . . . 34
3.3.2 Calculation of SMR . . . 36
3.4 Results . . . 37
3.5 Parameterizing Side Melt . . . 40
3.5.1 Model . . . 40
3.5.2 Parameterization Constants . . . 41
3.5.3 Comments on the Experimental Limitations . . . 43
3.5.4 Application to Observations . . . 44
3.6 Discussion . . . 46
3.7 Conclusions . . . 49
3.8 Part II: Ice Melting in a Sheared Flow . . . 50
3.9 Methods . . . 51
3.10 Results . . . 53
3.11 Discussion . . . 55
3.12 Conclusions . . . 59

**4 Numerical Simulations: Basal Melt of Tabular Icebergs 61**
4.1 Introduction . . . 61

4.2 Methods . . . . . 64
4.2.1 Ocean Model . . . . . 64
4.2.2 Ice Model . . . . . 65
4.2.3 Numerical Experiments . . . . . 65
4.3 Results . . . . . 66
4.3.1 Control Run . . . . . 66
4.3.2 Perturbation Experiments . . . . . 66
4.4 Discussion . . . . . 72
4.4.1 Theoretical Comparison of Melt Rate Parameterizations . . . 73
4.4.2 Dependence of Basal Conditions on Upstream Flow Properties 79
4.4.3 Restricting Parameter Space . . . . . 82
4.4.4 Proposed Melt Rate Parameterization Adaptations . . . . . 86
4.5 Conclusions . . . . . 88

**5 Conclusion** **91**
5.1 Summary of Findings . . . . . 91
5.2 Implications . . . . . 96

**Bibliography** **99**

# List of Figures

2.1 Top: A five-day segment from the PIES record, with automatically detected iceberg transit events shaded in blue, and their parabolic fits shown in red. The red dashed line indicates the average depth of the interface between the upper Polar Water and lower Atlantic Water layers in the fjord, for reference. Bottom: The corresponding period in the ocean velocity (shading) and wind (solid black line) data. The dashed vertical lines indicate the point of closest passage of the icebergs to the PIES, with the depth of the lines denoting the iceberg draft. . 10

2.2 Top row: Schematic views of a shallow iceberg (left) and a deep iceberg (right) passing over the PIES. Shallow icebergs are seen over a smaller area associated with the green circle in the left panels of the rows below, while deep icebergs intersect with the ensonified cone over a larger area (red circle in the left panels of the rows below). Middle row and bottom rows, Left: A bird's eye view of the region ensonfied by the PIES (blue circle), with an artificial iceberg (magenta square) passing overhead (trajectory shown in black, with crosses indicating the timesteps at which the artificial PIES emits a ping). Middle row and bottom rows, Right: The ping record that the PIES would produce (i.e. the distance associated with the first reflection, either from the air-sea interface or from the bottom of the iceberg), and the iceberg speed and draft range calculated from the parabola fitted to this record (magenta). . . . . 12

2.3 Left: Bathymetry and large-scale ocean circulation in south-east Greenland, with the red box marking Sermilik Fjord. Center: Location of the ADCP (yellow circle), PIES (red circle), and weather station (blue star) in Sermilik Fjord. Right: Sample profile of an iceberg passing over the PIES visible in early echos recorded by the sensor (black crosses), with concurrent along-fjord ocean velocity data (shading) and along-fjord wind data (red line). The solid black line indicates the parabolic fit to the early echos (from which the iceberg speed is obtained), with time 0 defined as the start of the fit, and the vertical dashed black line marking the minimum draft of the iceberg. 13

2.4 Dependence of observed iceberg speed $u$ (from parabolic fit to PIES record) on: (A) integrated ocean velocity over the iceberg draft $\bar{u}$ (dashed line indicates best fit); (B) along-fjord wind speed $u_a$ during its passage over the sensor; and (C) iceberg draft as deduced from the model in Section 2.4. The vertical dashed line marks the average depth (180 m (Jackson et al. 2014)) of the interface between the upper layer of Polar Water and the deeper layer of Atlantic Water in the fjord. . . 15

2.5 A schematic of the different iceberg shapes considered, with the draft $D$ and freeboard $F$ labeled, and the velocities of the air $u_a$ and ocean $u_o(z)$ illustrated. . . . . 18

2.6 Top left: A comparison, for different values of the oceanic drag coefficient $C_o$, of the iceberg velocity directly measured using iceberg tracker data (Sutherland et al. 2014) and the model-predicted velocity of icebergs moving in the fjord at that time, from concurrent ADCP data. Bottom left: Ocean velocity data for the period over which the iceberg velocity was measured. The estimated draft of the iceberg on which the GPS tracker was placed is 300 m. Right: The correlation between the observed and modeled iceberg speeds for the entire PIES record, as a function of the drag coefficient ratio $C_o/C_a$. . . . . 21

2.7 Top left: The PIES record and concurrent ADCP ocean velocity data for an iceberg passing the sensor during a period when the fjord flow was accelerating. The curvature of the PIES record is observed to increase over the observation period, indicating that the iceberg is accelerating. Bottom left: A comparison of the ocean velocity averaged over the iceberg's draft and the iceberg's speed (calculated from the curvature of the PIES record) over the event shown in the above panel. Right: The correlation between the observed and modeled iceberg speeds for the entire PIES record, as a function of the averaging time period used before the iceberg transit event. . . . . 22

2.8 Distributions of observed and modelled iceberg speed and drafts: (A) Observed minimum iceberg draft; (B) modelled iceberg draft; (C) observed iceberg speed; and (D) modelled iceberg speed. . . . . 24

2.9 Correlation between observed and modelled iceberg speed, using the one-dimensional simplified model of iceberg motion. . . . . 24

2.10 Example profiles of along-fjord velocities felt by icebergs. In each panel, the iceberg draft and velocity (from model-supplemented observations) are illustrated by the vertical blue line. The profile in black is the average ocean velocity during the passage of the iceberg over the sensor and the 6 hour period prior to its passage, with the extrapolated velocity in the top 40 m of the water column marked by the dashed extension of this profile, and the vertical average velocity over the iceberg draft marked by the black star. The wind speed and direction during the event are indicated by the red arrow (scaled by factor 5). The horizontal dashed lines indicate the average interface depth between the upper PW and deeper AW layers in the fjord (Jackson et al. 2014). . . . . 26

2.11 Dependence of error in iceberg velocity and melt on ocean shear. Panel A: Definition of surface speed $u_s$, average speed $\bar{u}$, and basal speed $u_b$ for an iceberg of draft $D$. Panel B: Error in iceberg speed due to applying the surface velocity as opposed to the depth-varying velocity in the model, as a function of the difference between the iceberg and the surface current $|u_s - \bar{u}|$. Panel C: Error in iceberg basal melt rate due to using the surface velocity rather than the basal velocity, as a function of the difference between the iceberg and the basal current $|\bar{u} - u_b|$. The best fits in (B) and (C) are marked with dashed lines, and the corresponding correlation coefficients labelled. . . . . 28

3.1 Schematic (not to scale) of the laboratory setup. (A) Side-view of the ice block suspended in the working part of the flume. (B) Birdseye view of the ice block, with the surface expression of a downstream melt plume hatched. . . . . 35

3.2 Left: Side (blue crosses) and basal (red crosses) SMRs as a function of ambient flow speed, calculated from tracking the ice edge in each of these regions in the experiment videos. The updated side melt parameterization (solid line) and laboratory error (gray shading) of the SMRs calculated from the mass loss over the course of the experiments, as discussed in Section 3.4 and seen in Figure 3.4, are shown for reference. Right: Total side and basal melt volumes as a function of ambient flow speed, calculated by scaling the SMR in the left panel by the experiment length and the side/basal area, respectively. The proportion of the basal melt to the total melt is shown by the gray circles. . . . . 37

3.3 Left: Side views of ice blocks after melting for 15 min in a homogeneous flow of (A) 0.5 cm $s^{-1}$, (B) 2 cm $s^{-1}$, and (C) 4.7 cm $s^{-1}$. Scale shown by ruler with 5 cm intervals. Right: Schematic representations of left panels. . . . . 39

3.4 Dependence of SMR on flow speed, split into regions (A) both plumes attached, (B) upstream plume detached, downstream plume attached, and (C) both plumes detached. The parameterization proposed in equation 3.5 for an average ice temperature of -15°C is shown in black, and the shaded region depicts the experimental error (calculated from two standard deviations of 3 repeated experiments). The dashed extension of the detached regime curve is the standard parameterized value of $M_b = Ku^{0.8}(T_o - T_i)/L^{0.2}$ (where $K = 0.75$ °$C^{-1}$ $m^{0.4}$ $d^{-1}$ $s^{0.8}$, $T_o = 20$°C, $T_i = -15$°C, and $L = 0.1$ m in the laboratory setting). . . 40

3.5 Left: Sample profiles of along-fjord velocities felt by two icebergs in Sermilik Fjord, from FitzMaurice et al. (2016), in (A) a linearly sheared flow and (B) a barotropic flow. The solid vertical line indicates the iceberg draft and velocity, and the profile (thin black line) is the average ocean velocity during and leading up to the iceberg's observation, with the dashed extension of this profile illustrating the extrapolated velocity in the top 40 m of the water column. Depths at which the relative velocity of the ocean is sufficiently low that we would anticipate an attached plume are shaded in yellow, and depths where it is high enough for the melt plume to detach are shaded in red. We assume a plume speed of 0.05 m $s^{-1}$ following the modelling of melting ice faces by Sciascia et al. (2013), which is consistent with the plume speed of 0.07 m $s^{-1}$ observed next to a grounded iceberg by Josberger and Neshyba (1980). Right: Schematics of plume regimes for (A) detached and (B) attached plumes corresponding to linearly sheared flow and barotropic flows, respectively. . . . . 46

3.6 A comparison of the old (gray) and new (green) parameterized iceberg side melt rates for the 90 icebergs in the observational record presented in Chapter 2, assuming a plume speed of 0.05 m $s^{-1}$ (Sciascia et al. 2013; Josberger and Neshyba 1980). The reference curves show the melt rate parameterizations as a function of the relative ice-ocean velocity for the typical temperatures of the upper and lower layers in the fjord (1°C and 3°C, respectively (Straneo et al. 2010)), for an iceberg of the mean draft $\bar{D}$ in the observational record and aspect ratio 1, where the iceberg draft influences the proportion of the iceberg in each of the warm lower and cool upper fjord layers. The left panel assumes an internal ice temperature $T_i = -4$°C, while the right panel assumes $T_i = -15$°C. It can be seen that the main difference exists between the parameterizations in the attached plume regime, when the relative ice-ocean velocity is less than the plume speed, and that the difference between the parameterizations in this regime is a strong function of the internal ice temperature. . . . . 47

3.7 A schematic (not to scale) of the laboratory setup for the vertically sheared flow experiments. (A) A side-view of the ice block suspended in the working part of the flume. (B) A birdseye view of the ice block, with a downstream surface layer of melt plume waters. . . . . 52

3.8 (A) Measured submarine side melt rate $M$ in the vertically sheared flow experiments, overlaid on the non-linear parameterization for iceberg side melt in a homogenous flow proposed in the first half of this chapter (FitzMaurice et al. 2017). The coloring of the top and bottom halves of the squares indicates the top and bottom layer velocities in that experiment, varying from 0 cm $s^{-1}$ (white) to 3.7 cm $s^{-1}$ (black). The lettering in the legend indicates which of these velocities would ordinarily be in the attached plume regime (A), and which would be in the detached plume regime (D). The star is the center point of the dashed line between the side melt rates $M(u_{\text{ave}} = 1.5$ cm $s^{-1})$ and $M(u_{\text{ave}} = 3.3$ cm $s^{-1})$, and illustrates that $\bar{M} = \frac{1}{2}\Big(M(u_{\text{ave}} = 1.5$ cm $s^{-1}) + M(u_{\text{ave}} = 3.3$ cm $s^{-1})\Big)$ is lower than the measured side melt rate $M$. (B) Non-dimensionalized difference $\Delta M$ between the measured submarine side melt rate and the submarine side melt rate predicted by averaging the side melt rate in each of the two layers, as a function of the non-dimensionalized difference in the layer speeds $\mathrm{d}\tilde{u} = \max\big(u_{\max} - \max(u_{\min}, w), 0\big)$. $\Delta M$ is non-dimensionalized with the experiment's average melt rate $\bar{M}$, and $\mathrm{d}\tilde{u}$ is non-dimensionalized with the experiment's maximum flow velocity $u_{\max}$. In both (A) and (B), the gray shading indicates the estimated experimental error in the measured side melt rate. . . . . 56

3.9 Top: Schematic of an ice block in a two-layer vertically sheared flow in which (A) $u_1 = u_2$, (B) $u_1 < u_2$, and (C) $u_1 > u_2$. In (A), the flow is predominantly around the ice block, whereas in (B)/(C) it is deflected up/down into the lower velocity layer. Bottom: Photos of the ice block after 15 minutes of melting for (A) $u_1 = u_2 = 3.3$ cm $s^{-1}$, (B) $u_1 = 0,\ u_2 = 3.3$ cm $s^{-1}$, and (C) $u_1 = 3.3,\ u_2 = 0$ cm $s^{-1}$. . . . . 57

3.10 The maximum value of the non-dimensionalized oceanic deflection parameter $d\tilde{u}$ (calculated using the maximum and minimum relative ice-ocean velocities over the iceberg draft in equation 3.10) and the corresponding percentage by which the side melt rate $M_s$ may be underestimated due to the neglect of shear for the 90 icebergs observed in the PIES record of Chapter 2. . . . . 59

4.1 (A) A bird's eye snapshot of the modeled channel flow $u$ with an iceberg of radius 20 km situated at $(x, y) = (250, 500)$ km. The inner black ring indicates the location of the flat iceberg base at depth 400 m, and the iceberg sides slope linearly upwards from this to the surface, such that the surface iceberg area is denoted by the outer black ring. The black dashed box indicates the area represented in the right-hand panel. (B) The mean melt rate over the iceberg base and sides as modeled by the three-equation parameterization. (C) A vertical snapshot of the salinity stratification, prior to melting being switched on (the iceberg is masked in gray). (D) Snaphsot of the downstream SST after melting is switched on. . . . . 67

4.2 (A) The in-situ basal melt rate (triangles) calculated using the three-equation parameterization, plotted as a function of the model-calculated upstream flow speeds. The parameterizations of $M_b$ as a function of speed at different $C$ for an iceberg of radius 20 km melting in a flow at the upstream temperature are shown for reference (solid lines). (B) The in-situ basal melt rate now plotted as a function of the model-calculated basal flow speed and temperature, and the freezing temperature $T_f$ used in place of the ice temperature $T_i$ (dashed lines). The errorbars represent two standard deviations of the melt rate over the six-month duration of the run. . . . . 68

4.3 (A) The in-situ basal melt rate (triangles) calculated using the three-equation parameterization, plotted as a function of the upstream flow temperature. The parameterizations of $M_b$ as a function of temperature at different $C$ for an iceberg of radius 20 km melting in a flow at the upstream flow speed are shown for reference (solid lines). (B) The in-situ basal melt rate now plotted as a function of the model-calculated basal flow temperature, with reference curves plotted using the model-calculated basal flow speed and temperature, and the freezing temperature $T_f$ used in place of the ice temperature $T_i$ (dashed lines). The errorbars represent two standard deviations of the melt rate over the six-month duration of the run. . . . . 69

4.4 (A) The in-situ basal melt rate (triangles) calculated using the three-equation parameterization, plotted as a function of the iceberg radius. The parameterizations of $M_b$ as a function of $R$ at different $C$ for an iceberg melting in a flow at the upstream flow speed and temperature are shown for reference (solid lines). (B) The in-situ basal melt rate again plotted as a function of the iceberg radius, but with reference curves plotted using the model-calculated basal flow speed and temperature, and the freezing temperature $T_f$ used in place of the ice temperature $T_i$ (dashed lines). The errorbars represent two standard deviations of the melt rate over the six-month duration of the run. . . 71

4.5 A schematic illustrating that it is the basal plume properties $u_b, T_b$ that control an iceberg's melt rate, rather than the upstream free flow properties $u_o, T_o$. . . . . 73

4.6 A comparison of the three-equation model heat transfer coefficient $\gamma_{T,\mathrm{3EM}}$ (blue line) and the bulk model heat transfer coefficient $\gamma_{T,\mathrm{bulk}}$ (red line) as a function of the iceberg radius $R$ for a flow speed of $u = 0.02$ ms$^{-1}$. Note that the values of $\gamma_T$ have been scaled by factor 86400 to produce melt rates in units of m d$^{-1}$. At small $R$, $\gamma_{T,\mathrm{bulk}}$ is more physically relevant, while when $R$ is large (certainly when $R > R_d$), $\gamma_{T,\mathrm{3EM}}$ is more physical. In between, a matching region should exist between the two heat transfer coefficients (gray shading). A hypothetical matching is illustrated by the black dashed line. The black star indicates the location in parameter space of the control numerical experiment conducted in Section 4.3. . . . . 78

4.7 Top Row: The average model-calculated iceberg basal speed as a function of (A) the upstream free flow speed, (B) the upstream temperature, and (C) the iceberg radius. Bottom Row: The average model-calculated iceberg basal temperature as a function of (D) the upstream free flow speed, (E) the upstream temperature, and (F) the iceberg radius. The curves in (B) and (E) are the linear lines of best fit. They are described by the equations $u_b = 0.004T_o + 0.02$ and $T_b = 0.7T_o - 1.2$, respectively. In all panels, the errorbars represent two standard deviations of the observed quantity over the six-month duration of the run. . . . . 79

4.8 Row 1: Side plot of the six-month average zonal velocity field $u$ for $f/5$, control $f$, $5f$. Row 2: The magnitude of the basal velocity (left) and basal temperature (right) as a function of the ratio of the iceberg lengthscale to the Rossby deformation radius $L/R_d$. The Rossby deformation radius $R_d$ is 75 km, 30 km, 15 km, 8 km, and 3 km in the $f/5$, $f/2$, $f$, $2f$, and $5f$ runs, respectively, and the iceberg radius is held fixed at 20 km. The control run $f = -1.4 \times 10^{-4}$ s$^{-1}$ is circled in green in both figures. . . . . 83

4.9 The cumulative density function for iceberg number (red) and iceberg melt (blue), as a function of iceberg radius. The solid blue line represents equation 4.37, obtained if a length-independent model of melt such as the three-equation parameterization is used, and the dotted blue line represents equation 4.39, obtained if the bulk parameterization of melting is used. Even though less than 8% of icebergs have radii greater than 20 km, 80% of melt comes from these icebergs, and 50 % of melt comes from icebergs with radii greater than 50 km. . . . 86

4.10 A comparison of the updated parameterization of tabular iceberg basal melt (equation 4.40, green solid lines) to the old bulk parameterization of basal melt (equation 4.6, gray dotted lines) and the in-situ melt rate calculated using the three-equation parameterization of melt (black triangles, errorbars representing two standard deviations of the observed quantity over the six-month duration of the run), (A) as the upstream flow speed $u$ is varied, and (B) as the upstream temperature $T_o$ is varied. This parameterization is proposed for use with icebergs that are large relative to the deformation radius. . . . . 88

# Chapter 1

# Introduction

## 1.1 Context

The Earth's climate is a dynamic and evolving system, forced by the input of shortwave radiation from the sun (which oscillates over time with both solar and orbital cycles), and modulated by the emission of longwave radiation from the planet's surface and the storage of heat by the atmosphere and ocean. The chemical composition of the atmosphere, the activities of the terrestrial biosphere, the circulation of the ocean, and the growth and decay of the polar ice caps, among other things, feed into this system and contribute to inter-annual, multi-decadal, and longer term fluctuations in the Earth's climate. Since the industrial revolution, humans have increasingly influenced these natural cycles by emitting greenhouse gases into the atmosphere, shifting the planet's energy balance away from the equilibrium position it has occupied for most of the Holocene, and ushering in a new era in the Earth's climate dubbed the Anthropocene (Ruddiman 2001; Marshall and Plumb 2016; Vallis 2017).

The scientific effort to understand the human impact on climate has comprised observations of the atmosphere and oceans, laboratory experiments studying envi-

ronmental processes, and theoretical modeling of the climate system. These strands are brought together in the form of global climate models (GCMs); sophisticated numerical models of the Earth's land, atmosphere, and ocean, which may be used to predict the multifaceted consequences of increasing atmospheric greenhouse gas concentrations. As computing power has grown, these models have been able to increase in resolution and complexity, covering smaller and smaller spatial scales, and resolving more and more climate processes. However, there is a fundamentally intractable problem of scale at play, with microscopic dynamical, thermodynamical, and chemical processes feeding into global climate patterns. It is not feasible to directly simulate with one model, for instance, both the turbulence of an ice shelf's melt plume and the large-scale circulation of the ocean gyre it flows into. Instead, GCMs use what are known as parameterizations to capture the bulk effect of the processes occurring on sub-gridcell scales.

This thesis is structured as a sequential exploration of one such parameterization, namely that of iceberg melt. Starting with observations of icebergs at their origin in a Greenland fjord in Chapter 2, we use a simple modeling approach to determine the dominant force balance controlling iceberg motion, and to estimate the relative velocity between icebergs and the ocean over their draft. We proceed by conducting a series of laboratory experiments to determine the influence of this relative velocity on iceberg submarine melt in Chapter 3, and subsequently extend these experiments to the case of a vertically sheared flow. Finally, we numerically model an iceberg melting in a background flow in Chapter 4, and use the results of this study to inform an improved parameterization of iceberg melt and meltwater distribution in GCMs. A concluding discussion follows in Chapter 5.

The results of Chapter 2 were presented at the 2016 International Glaciological Society meeting, and are published in FitzMaurice et al. (2016) with co-authors F. Straneo, C. Cenedese, and M. Andres. The first half of Chapter 3 is published

in FitzMaurice et al. (2017) with co-authors C. Cenedese and F. Straneo, and the second half of Chapter 3 is under review in the *Journal of Physical Oceanography* (FitzMaurice et al. Under Review), also with co-authors C. Cenedese and F. Straneo. At the time of writing, Chapter 4 has been submitted for publication in the journal *Ocean Modelling* (FitzMaurice and Stern Submitted). We thank the Cooperative Institute for Climate Science for their generous funding of this work.

## 1.2 Motivation

The Greenland and Antarctic ice sheets accumulate mass when snow falling on their surfaces does not melt over the course of the year, and compacts into ice over time. The ice sheets maintain equilibrium by losing mass through a combination of surface and subsurface melt, and discharging icebergs from their marine-terminating margins (Hanna et al. 2013). Of these processes, iceberg calving is thought to contribute approximately half the mass loss in both Greenland and Antarctica, representing a mass flux of roughly 500 $km^3yr^{-1}$ from Greenland (Enderlin et al. 2014; Rignot et al. 2008) and 1,300 $km^3yr^{-1}$ from Antarctica (Depoorter et al. 2013). With rising global temperatures there has been an observed increase in the discharge of ice from the Antarctic and Greenland ice sheets (Bamber et al. 2012; Rignot et al. 2011). This trend has motivated a focus on the study of icebergs, which act as conduits for transporting freshwater from the ice sheet margins to the ocean as they are carried away from their sources and melt.

From a climate modeling perspective, this mass flux to the ocean is of interest for several reasons. Firstly, the supply of meltwater to the ocean influences the properties of the water column, increasing stability if it is deposited in an almost undiluted surface layer, and potentially decreasing stability if it is released at depth. Increased water column stability in polar regions is associated with suppressed convection and

enhanced sea ice formation, while decreased stability promotes convection and dampens sea ice growth (Gade 1993; Stephenson et al. 2011; Helly et al. 2011; Merino et al. 2016). In terms of the influence of iceberg melt on sea surface temperature (SST) and sea ice coverage, the literature remains undecided. Some studies suggest that icebergs act to reduce SSTs and promote sea ice growth (e.g. Robinson and Williams (2012); Merino et al. (2016)), while others argue that depending on the ocean stratification this may not always be the case (Bintanja et al. 2013; Stern et al. 2016). These contradicting observations may be explained by the vertical distribution of iceberg meltwater, with less surface cooling and freshening observed when meltwater is well mixed in the water column (Stern et al. 2017). In the North Atlantic, as well as impacting sea ice formation, localized surface-concentrated freshwater fluxes can result in the capping of deep convection sites, with potential implications for the Atlantic Meridional Overturning Circulation (AMOC) (e.g. Srokosz et al. (2012), Zickfeld et al. (2007)). Accurate modelling of iceberg motion and melt is necessary to describe this meltwater flux and hence capture the ocean's response to the increased mass flux from Greenland and Antarctica.

In addition to these physical considerations, icebergs are also known to influence the oceanic nutrient distribution either through direct release or re-distribution of existing nutrients as they melt. Enhanced nutrient availability has been observed in iceberg melt plumes, which promotes blooms of ocean biology (Smith et al. 2007; Duprat et al. 2016). Despite the regional nature of this effect, it has implications for the large-scale sequestration of carbon by the ocean. To predict when and where such blooms may occur, and how their frequency and intensity may change in the future, we must first understand the underlying dynamics and thermodynamics of iceberg motion and melting. There has consequently been an increased interest in understanding iceberg trajectories and melt patterns in recent years, with a view to improving the representation of their influence on the ocean in global climate models.

The studies that constitute this thesis are a series of contributions to this continued scientific effort.

# Chapter 2

# Observations: Icebergs in a Greenland Fjord

## 2.1 Introduction

Despite icebergs' potential importance in the climate system, little has been done to validate parameterizations of their motion and melting, in large part due to the intrinsic difficulties of observing icebergs in the ocean. In this chapter, we investigate iceberg dynamics using an eight-month draft and speed record comprising 90 icebergs from Sermilik Fjord, south-east Greenland, following the methodology of Andres et al. (2015). The large number of icebergs sampled in this study, in conjunction with local ocean current and wind data, provides an unprecedented data set with which to evaluate assumptions frequently made in modelling of iceberg dynamics and melting. The standard parameterizations used to model iceberg motion and melt in Global Climate Models (GCMs) are summarized in Section 2.2, the dataset analyzed in this study is described in Section 2.3, and Section 2.4 introduces the model used to supplement these data. Results and their implications for the representation of

icebergs in climate models are presented in Section 2.5, and conclusions are drawn in Section 2.6.

## 2.2 Background

### 2.2.1 Modelling of Iceberg Motion

In climate models, the canonical equation used to describe iceberg motion is that of Bigg et al. (1997) and Gladstone et al. (2001) (building on earlier work by Smith (1993) and Mountain (1980)), in which icebergs are forced by a combination of surface currents and winds, sea ice and wave stresses, and surface pressure gradients. This leads to a momentum equation

$$M\frac{\mathrm{d}\vec{u}}{\mathrm{d}t} = -M\vec{f}\times\vec{u} + \vec{\tau_a} + \vec{\tau_o} + \vec{\tau_i} + \vec{F_w} + \vec{F_p}, \tag{2.1}$$

as in Martin and Adcroft (2010), for an iceberg of velocity $\vec{u}$ and mass $M$. Here, $\vec{f}$ is the Coriolis parameter, $\vec{\tau_a}$, $\vec{\tau_o}$, and $\vec{\tau_i}$ denote air, ocean, and ice stresses, and the wave and pressure gradient forcings are $\vec{F_w}$ and $\vec{F_p}$, respectively.

In a fjord environment, it is reasonable to simplify the above full open ocean model and assume that the motion of the icebergs in our record is predominantly governed by the air and ocean forcings alone. These assumptions are fully discussed in Section 2.4.

### 2.2.2 Modelling of Iceberg Melt

Icebergs deteriorate through surface melting from solar radiation, subsurface melting from buoyant vertical convection and forced convection, wave erosion at their margins, and calving of smaller components (El-Tahan et al. 1987; Savage 2001). Surface melt is negligible compared to subsurface melt, and calving of overhanging slabs is likewise

believed small (Savage 2001; Bigg 2016). Thus to model disintegration of icebergs, bottom melt $M_b$, subsurface side melt $M_s$, and wave erosion $M_e$ are the dominant processes that must be parameterized (Gladstone et al. 2001; Martin and Adcroft 2010; Bigg 2016). For reference, typical maximum parameterized values for basal melt, side melt, and wave erosion rates in the open ocean are 1 m $d^{-1}$, 0.2 m $d^{-1}$, and 0.5-1 m $d^{-1}$, respectively (Bigg 2016).

Typical parameterizations of bottom melt (e.g., Bigg et al. (1997); Savage (2001); Martin and Adcroft (2010); Marsh et al. (2015)) are based on studies of forced convection past a body (Weeks and Campbell 1973; El-Tahan et al. 1987), with the ambient velocity of the flow past the iceberg keel taken as the surface current speed (Martin and Adcroft 2010; Marsh et al. 2015). With this parameterization, the basal melt $M_b$ in units of m $d^{-1}$ is

$$M_b = 0.58 \ |\vec{u} - \vec{u_o}|^{0.8} \ \frac{T_o - T_i}{L^{0.2}}, \tag{2.2}$$

where $T_o$ is the surface ocean temperature (°C), $T_i$ is the ice temperature (assumed constant at $-4$°C), and $L$ is the iceberg length (m) in the direction of the flow (Weeks and Campbell 1973; Martin and Adcroft 2010). The constant 0.58 is dimensional, and incorporates the change in time units from $s^{-1}$ to $d^{-1}$, with units °$C^{-1}$ $m^{0.4}$ $d^{-1}$ $s^{0.8}$. It will be considered in depth in Chapter 4. As in equation 2.1, $\vec{u}$ is the iceberg velocity, and now $\vec{u_o}$ is the surface ocean velocity (both in units of m $s^{-1}$). For subsurface side melt, the parameterization is even more idealized than for basal melt. Explicitly, an empirically-deduced flow-independent melt rate simply a function of the sea surface temperature is generally assumed (Neshyba and Josberger 1980). The subsurface side melt parameterization will be considered in depth in Chapter 3, and the basal melt parameterization will be examined in Chapter 4.

In what follows, we consider the validity of the above melt parameterizations for Sermilik Fjord icebergs. By comparing our eight-month iceberg record to concurrent ocean current speed measurements, we examine the interplay between ocean currents and iceberg dynamics and melting, quantifying potential errors accrued by the parameterizations.

## 2.3 Data

### 2.3.1 Iceberg Record

The iceberg record considered in this study was obtained from a pressure-sensor-equipped inverted echo sounder (PIES) deployed in Sermilik Fjord in south-east Greenland between November 2011 and June 2012 (location shown in Figure 2.3). The sensor sat in the center of the fjord at a depth of approximately 860 m, emitting four 12 kHz ping bursts every ten minutes. The pings bounce off strong reflectors, and the PIES recorded the time until the first reflection from each ping arrived back at the instrument. Generally the first strong reflector encountered is the air-sea interface, but if an iceberg passes over the instrument, the first reflection may come from this instead. Consequently, iceberg transits leave distinctive parabolic signatures in the record of early pings from the PIES as they gradually move across the sensor's field of view, as shown in Figure 2.1 and in the right of Figure 2.3. From these parabolas' curvature and minima we can estimate the iceberg's speed and draft. The data collection methodology and theory underlying iceberg speed and depth estimation are described in detail in Andres et al. (2015), and intuition is provided using a toy model at the end of this subsection.

In our study iceberg transits are automatically detected in the PIES record by locating parabolic fits within a sliding window, six early echos in width, that moves through the record. Once identified, it is assumed that near the minimum of this

parabola, all pings bounced off the same point on the passing iceberg. Thus the parabola's curvature directly relates to the speed with which this point first approached, then receded from the sensor, and so may be used to calculate the iceberg's speed. A draft range may also be obtained, bounded by a minimum draft corresponding to an iceberg passing directly over the sensor, and a maximum draft corresponding to its passing the region ensonified by the PIES tangentially. The top panel of Figure 2.1 shows a typical five-day period taken from the PIES record, during which five iceberg transit events were algorithmically detected, and the parabolic fits associated with these events are shown in red.

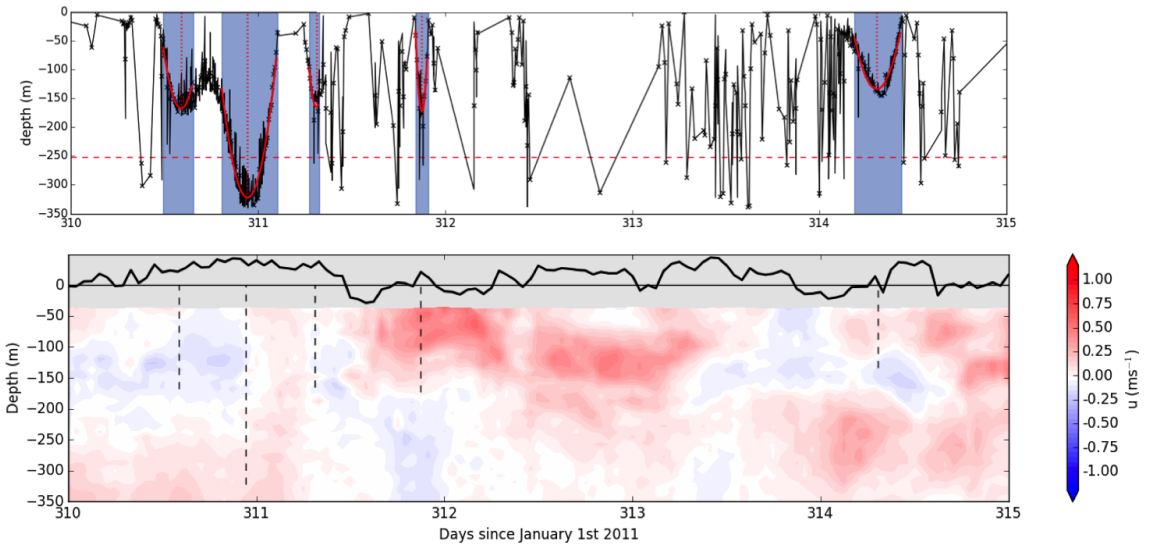



Figure 2.1: Top: A five-day segment from the PIES record, with automatically detected iceberg transit events shaded in blue, and their parabolic fits shown in red. The red dashed line indicates the average depth of the interface between the upper Polar Water and lower Atlantic Water layers in the fjord, for reference. Bottom: The corresponding period in the ocean velocity (shading) and wind (solid black line) data. The dashed vertical lines indicate the point of closest passage of the icebergs to the PIES, with the depth of the lines denoting the iceberg draft.

In order to validate the method applied to calculate iceberg speed and draft ranges from the PIES data, we produced a toy numerical model of the sensor and simulated an artificial ping record for a toy iceberg passing through the field of view of the PIES. The model took as input the dimensions of the cuboid toy iceberg (draft,

width, and length), the iceberg's start location, and a specified iceberg velocity vector over the time period of the simulation. The toy iceberg was then moved across the spatial domain ensonified by the model PIES according to this velocity vector, and the first reflection distance as measured by the toy sensor was calculated every ten model minutes to match the frequency of acoustic bursts from the PIES. The model returned the toy iceberg trajectory, the artificial PIES record, and the iceberg draft and speed estimated from the artificial pings. This could then be compared to the actual iceberg draft and speed, known from the input toy iceberg dimensions and velocity vector. Figure 2.2 shows the output from two example toy model runs, one for a shallow iceberg, and one for a deep iceberg. There is a geometrical difference between these cases as a consequence of the iceberg draft, as illustrated by the top row of the figure, which results in the icebergs being visible to the toy PIES over different spatial regions (green and red circles in Figure 2.2). In the first example run, the iceberg draft $D = 100$ m and the mean input velocity is $\bar{u} = 0.09$ m s$^{-1}$. From the artificial ping record, our methodology is able to correctly identify a draft range of 91-317 m, and predicts the iceberg velocity to be 0.08 m s$^{-1}$. In the second example run, the iceberg draft is 600 m, and the mean input velocity is 0.05 m s$^{-1}$. Again, the model correctly identified a draft range of 538-633 m, and an iceberg speed of 0.05 m s$^{-1}$.

### 2.3.2 Ocean Velocity and Wind Data

A 75 kHz RDI acoustic Doppler current profiler (ADCP) was deployed in Sermilik Fjord from August 2011 to June 2012, as described in Jackson et al. (2014). This sensor measured velocity in the water column between depths of 388 m and 40 m in 10 m bins, at hourly intervals. A five-day sample of the ocean velocity data is shown in the bottom panel of Figure 2.1. We assume that icebergs moving past the PIES feel the same ocean velocity as that recorded by the ADCP. This is reasonable

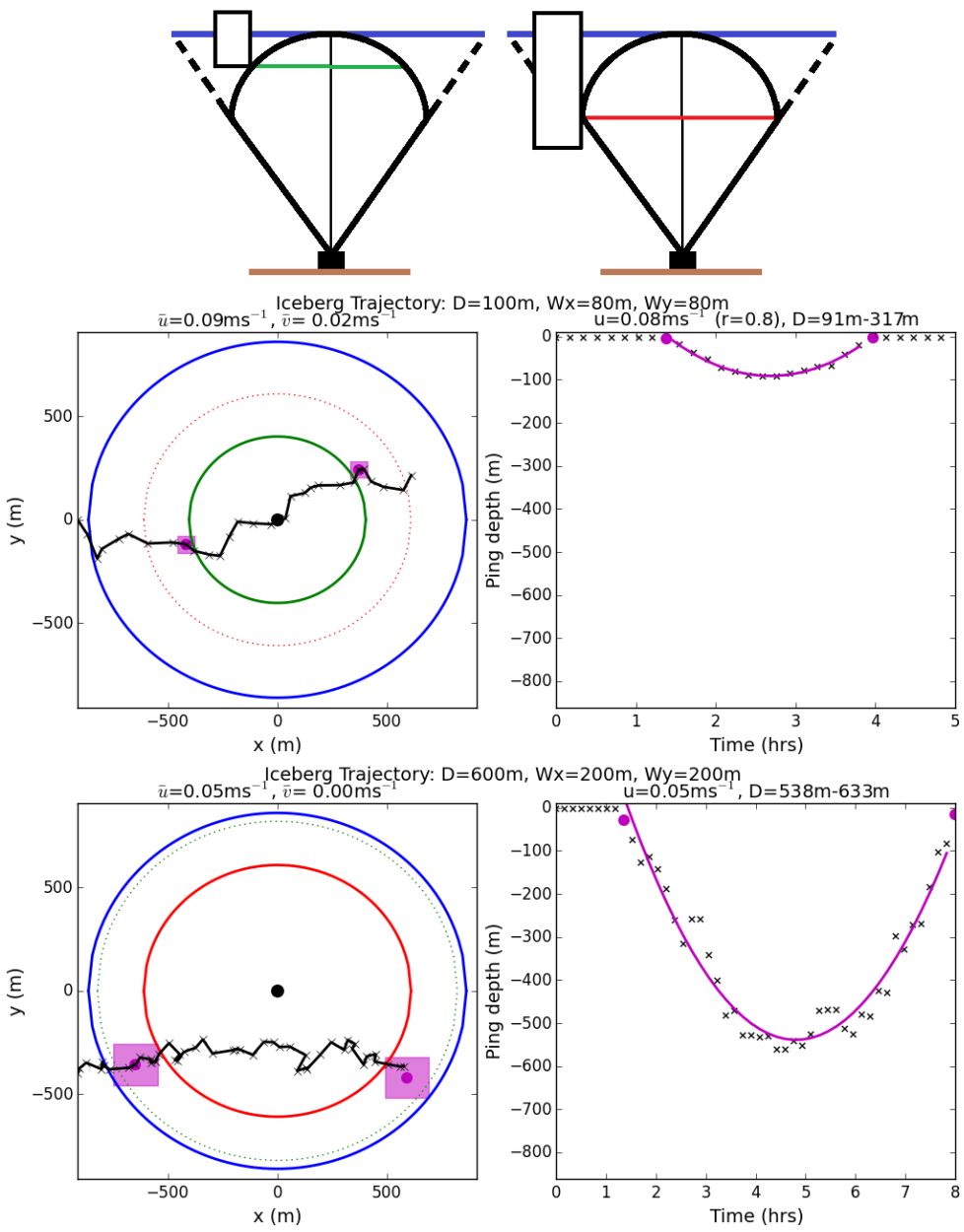



Figure 2.2: Top row: Schematic views of a shallow iceberg (left) and a deep iceberg (right) passing over the PIES. Shallow icebergs are seen over a smaller area associated with the green circle in the left panels of the rows below, while deep icebergs intersect with the ensonified cone over a larger area (red circle in the left panels of the rows below). Middle row and bottom rows, Left: A bird's eye view of the region ensonfied by the PIES (blue circle), with an artificial iceberg (magenta square) passing overhead (trajectory shown in black, with crosses indicating the timesteps at which the artificial PIES emits a ping). Middle row and bottom rows, Right: The ping record that the PIES would produce (i.e. the distance associated with the first reflection, either from the air-sea interface or from the bottom of the iceberg), and the iceberg speed and draft range calculated from the parabola fitted to this record (magenta).

since the distance between the ADCP and the PIES (2 km) is small compared to the distance over which currents vary in the fjord, and the lengthscales over which icebergs change velocity (Jackson et al. 2014; Sutherland et al. 2014).

Wind data were obtained at 10-minute intervals during the study period from the Station Coast weather station (Mernild et al. 2008; Oltmanns et al. 2015) located 25 m above sea level at the fjord mouth, 24 km from the ADCP. Ocean current and wind data were rotated into the along-fjord direction (32° from North), with flows up-fjord towards the calving face of Helheim glacier taken as positive. Figure 2.3 shows the relative positions of the PIES, the ADCP, and the weather station in Sermilik Fjord, and their combined output for a given iceberg transit event. The curvature of the parabolic fit to this event gives an iceberg speed of 0.1 m $s^{-1}$.

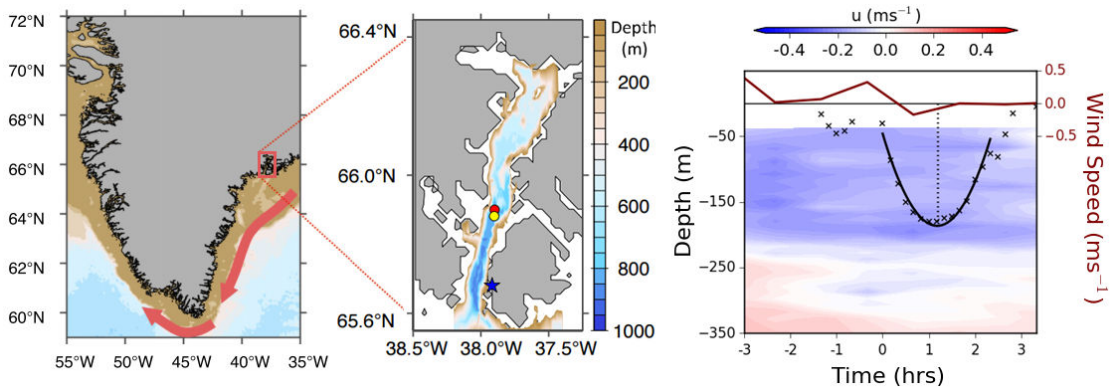



Figure 2.3: Left: Bathymetry and large-scale ocean circulation in south-east Greenland, with the red box marking Sermilik Fjord. Center: Location of the ADCP (yellow circle), PIES (red circle), and weather station (blue star) in Sermilik Fjord. Right: Sample profile of an iceberg passing over the PIES visible in early echos recorded by the sensor (black crosses), with concurrent along-fjord ocean velocity data (shading) and along-fjord wind data (red line). The solid black line indicates the parabolic fit to the early echos (from which the iceberg speed is obtained), with time 0 defined as the start of the fit, and the vertical dashed black line marking the minimum draft of the iceberg.

### 2.3.3 Behavior of Icebergs in Sermilik Fjord

During summer, the PIES record was too noisy to identify parabolic transits, possibly due to increased biology or sediment in the water column producing many early reflections. From 26$^{\text{th}}$ February to 10$^{\text{th}}$ March 2012, land-fast sea ice was present (Andres et al. 2015) and no transits were recorded. Excepting this two-week period, 90 clean transits were recorded between November and June. The average iceberg speed was 0.09 m s$^{-1}$, with range 0.02 m s$^{-1}$ to 0.24 ms $^{-1}$. The average minimum iceberg draft (obtained assuming the iceberg passed directly over the sensor) was 148 m, the total draft range was 7 m to 490 m.

Iceberg speed was strongly correlated with the ocean velocity vertically integrated over the iceberg draft (Figure 2.4A), while there was negligible correlation between iceberg speed and along-fjord wind speed (Figure 2.4B), suggesting that it is predominantly the ocean forcing that controls the iceberg motion in the fjord. Iceberg draft was uncorrelated with iceberg speed, but note that the fastest icebergs had drafts of around 180 m (Figure 2.4C), the average depth of the interface between the deeper Atlantic Water (AW) layer and upper Polar Water (PW) layer in Sermilik fjord (Jackson et al. 2014). A plausible explanation is that shallower icebergs are more easily slowed by surface drag associated with sea ice and bergy bits, and deeper icebergs experience a more greatly sheared ocean flow, enabling intermediate draft icebergs to travel the fastest.

## 2.4 Model

In Section 2.3.1, we explained how iceberg speeds and draft ranges could be deduced from the PIES early-echo record. To determine ocean relative velocity profiles felt by iceberg keels in Sermilik fjord, we must also provide a direction of motion and a single value of the draft for the icebergs. To do this, we used a one-dimensional

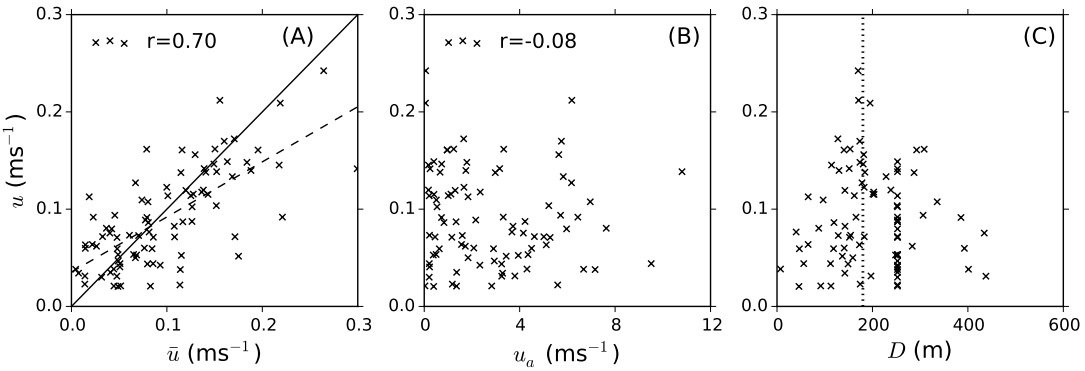



Figure 2.4: Dependence of observed iceberg speed $u$ (from parabolic fit to PIES record) on: (A) integrated ocean velocity over the iceberg draft $\bar{u}$ (dashed line indicates best fit); (B) along-fjord wind speed $u_a$ during its passage over the sensor; and (C) iceberg draft as deduced from the model in Section 2.4. The vertical dashed line marks the average depth (180 m (Jackson et al. 2014)) of the interface between the upper layer of Polar Water and the deeper layer of Atlantic Water in the fjord.

steady-state simplification of the canonical model of iceberg motion (equation 2.1) to supplement the data, and neglected Coriolis forces, wave forces, pressure gradient forces, and stresses due to the presence of sea ice. The validity of these simplifications and the assumption that icebergs may be modelled as cuboids and are in steady state with their forcings are examined in Sections 2.4.1-2.4.3.

With the above assumptions, the momentum equation (2.1) becomes

$$\tau_{\mathrm{a}} + \tau_{\mathrm{o}} = 0, \tag{2.3}$$

so wind and ocean stresses on the iceberg are balanced, and the iceberg moves at a constant speed. Stress terms $\tau_a$ and $\tau_o$ are calculated by integrating air and ocean forces over the iceberg freeboard $F$ and draft $D$ (where $D/(F+D) = 0.8$), respectively. For a cuboid iceberg of draft $D$ and velocity $u$, the stress terms have the

form

$$\tau_a = \rho_a C_a |u_a - u|(u_a - u)F, \tag{2.4}$$

$$\tau_o = \rho_o C_o \int_{-D}^{0} |u_o(z) - u|(u_o(z) - u)\, \mathrm{d}z. \tag{2.5}$$

The subscripts $a$ and $o$ indicate atmospheric and oceanic properties respectively, with $\rho$ the fluid's density, and $C$ the fluid's dimensionless drag coefficient.

Following a sensitivity analysis (see Section 2.4.3), we tuned the one dimensional model with the standard ocean and atmospheric drag coefficients of Bigg et al. (1997), with values of 0.9 and 1.3, respectively. To obtain the approximate steady state forcing on the iceberg we averaged ocean currents and winds from 6 hours prior to the iceberg's transit over the PIES, to when the iceberg left the sensor's field of view.

For each iceberg record, concurrent wind and ocean velocity data were extracted and averaged over the requisite time period. There is no ocean velocity data from the ADCP record over the top 40 m of the water column, so the velocity gradient in the three 10 m bins closest to the surface was extrapolated to obtain the velocity in this layer (as discussed in Section 2.4.1). Given the ocean and air velocities associated with the iceberg transit, an optimization algorithm was run to minimize the cost function $|\tau_\mathrm{a} + \tau_\mathrm{o}|$ for varying values of iceberg velocity $u$. This was conducted for three values of iceberg draft in the observed draft range: the minimum possible draft, the maximum possible draft, and the mean of the minimum and maximum drafts. The fitted velocity magnitude was then compared to the observed speed, and the iceberg draft was taken to be that which gave the best fit to this observed speed. Note that whereas the minimum and average drafts vary continuously, 252 m is the upper bound on iceberg draft for any shallow icebergs (Andres et al. 2015), explaining the larger number of icebergs with this draft in Figure 2.4C.

The simplified model successfully reproduced observed iceberg speeds, with a correlation coefficient of 0.8 between observed and modelled speeds (Figure 2.9). This agreement gave confidence that the model simplifications were reasonable for Sermilik Fjord, and allowed us to proceed based on the velocity signs and drafts produced by the model.

### 2.4.1 Forcing Terms

We now consider the validity of the simplifications we made to the canonical model of iceberg motion of Bigg et al. (1997) and Gladstone et al. (2001) to obtain the direction of iceberg motion and a single value of the draft for each iceberg that passed over the PIES. The first of these simplifications was that we assumed a one-dimensional along-fjord frame, in which icebergs were modelled as cuboids in steady state with the wind and ocean current forcing.

Hydrographic surveys of Sermilik Fjord (Straneo et al. 2010), the study site from which our data are drawn, show that variability predominantly occurs in the along-fjord direction, justifying the use of a one-dimensional frame. Further, except for a two-week period from 26$^{\text{th}}$ February to 10$^{\text{th}}$ March 2012, the region of the fjord containing the mooring was generally free from land-fast sea ice during the period of our study (Andres et al. 2015). The ice stress term $\vec{\tau_i}$ is negligible unless thick pack ice is present (Bigg 2016), so given the lack of land-fast sea ice, $\tau_i$ is likely to be small throughout our study. Despite the absence of land-fast sea ice, satellite imagery during the study period shows that there was ice coverage of the fjord from drifting sea ice, bergy bits and icebergs at all times. This coverage acts to rapidly damp waves in the fjord, implying a small wave radiation force $F_w$. In general, the wave radiation force is thought to account for under 5% of the iceberg force balance in the Arctic (Bigg 2016). Finally, the pressure gradient force $F_p$ results from the difference in surface pressure across the iceberg. While this is one of the dominant

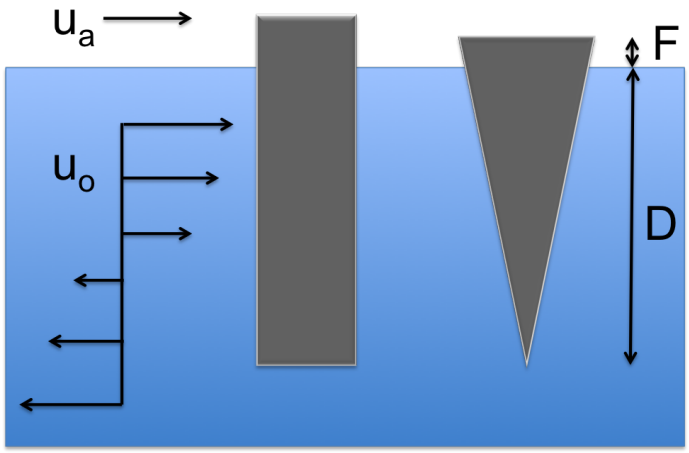



Figure 2.5: A schematic of the different iceberg shapes considered, with the draft $D$ and freeboard $F$ labeled, and the velocities of the air $u_a$ and ocean $u_o(z)$ illustrated.

terms in the force balance of large tabular Antarctic icebergs (Bigg 2016), we assume that it is relatively small for more moderately sized Greenlandic icebergs.

To determine the ocean forcing on the icebergs, it was necessary to prescribe an ocean velocity in the top 40 m of the water column, in which there is no ocean velocity data from the ADCP. To obtain the velocity in this layer, the velocity gradient in the three 10 m bins closest to the surface was extrapolated. If instead a constant velocity was assumed over the top 40 m of the water column, equal to the velocity in the shallowest ADCP bin, the correlation between the modelled and observed speeds drops from 0.80 to 0.76. There was therefore only a slight sensitivity of the data set as a whole to the method used to prescribe the surface layer velocity.

### 2.4.2 Iceberg Shape

Two shapes of iceberg were considered; cuboid icebergs (which are equivalent to cylindrical icebergs in a one-dimensional model) and conical icebergs (Figure 2.5). For a cuboid iceberg of draft $D$, freeboard $F$ and velocity $u$, the stress terms have

the form given in equations 2.4-2.5, i.e.

$$\tau_a = \rho_a C_a |u_a - u|(u_a - u)F, \tag{2.6}$$

$$\tau_o = \rho_o C_o \int_{-D}^{0} |u_o(z) - u|(u_o(z) - u)\, \mathrm{d}z. \tag{2.7}$$

The subscripts $a$ and $o$ indicate atmospheric and oceanic properties respectively, with $\rho$ the fluid's density, and $C$ the fluid's dimensionless drag coefficient. For a conical iceberg this is modified to

$$\tau_a = \rho_a C_a |u_a - u|(u_a - u)(DF + \tfrac{1}{2}F^2), \tag{2.8}$$

$$\tau_o = \rho_o C_o \int_{-D}^{0} (D - z)|u_o(z) - u|(u_o(z) - u)\, \mathrm{d}z, \tag{2.9}$$

where the freeboard $F$ of the iceberg is calculated as the solution to $F^3 + 3DF^2 + 3D^2F - D^3/9 = 0$ to ensure that 90% of the iceberg's volume is submersed.

The modelling of icebergs as cuboids versus cones was assessed by comparing the fit between $u_{\text{obs}}$ and $u_{\text{model}}$ for these two shapes. It was found that cuboid shaped icebergs had a marginally better fit than conical ones, with correlation coefficients of 0.80 and 0.72 between the modelled and PIES-observed speeds, respectively. This result suggested that the shape of icebergs is of second order importance, with the modelling of icebergs as cuboids being a reasonable assumption. There was likewise low sensitivity to the freeboard ratio $D/(F + D)$ within the plausible range of 0.8 to 0.9. In what follows, our modelling results assume a cuboid iceberg shape and a freeboard ratio of 0.8.

### 2.4.3 Drag Coefficients and Temporal Equilibration

In addition to the effect of iceberg shape, the choice of drag coefficients was assessed. Traditionally, these have been based loosely on empirical observations of the drag

coefficients for sea ice (Gladstone et al. 2001), with $C_a = 1.3$ and $C_o = 0.9$ for the face of the ice orthogonal to the flow direction. In the steady state, which is governed by a balance between $\tau_o$ and $\tau_a$, the drag coefficients only appear in the ratio $C_\mathrm{o}/C_\mathrm{a}$. The best correlation between the modelled and observed speeds (with correlation coefficient 0.8) occurred at $C_\mathrm{o}/C_\mathrm{a} = 0.75$, with this correlation dropping off to zero as the ratio decreased to zero, and asymptoting to 0.7 as the ratio tended to infinity (right panel of Figure 2.6). This asymmetry illustrates the dominance of ocean currents in determining iceberg motion. The values of the drag coefficients currently used in climate models ($C_o = 0.9$ and $C_a = 1.3$) give a ratio of $C_o/C_a = 0.69$, which is close to this best fit value, so we employ these values for the drag coefficients in our following modelling results.

To investigate the oceanic drag coefficient directly, rather than just in ratio with the atmospheric drag coefficient, a time-dependent version of the one-dimensional model introduced above may be obtained by assuming that the iceberg is initially at rest and is caused to accelerate by subsequent wind and and ocean forcing. The iceberg's response time depends on its mass, which may be related to its draft by assuming a constant aspect ratio and ice density. During our period of observation, a separate study was conducted by Sutherland et al. (2014) in Sermilik Fjord, in which they placed GPS trackers on several icebergs in the fjord. One of the tracked icebergs happened to pass in the vicinity of our ADCP, and so the velocity obtained directly from the GPS tracker on this iceberg can be compared to the velocity predicted using the ocean forcing and our one-dimensional model, for different values of the oceanic drag coefficient. This comparison is illustrated in the left panels of Figure 2.6. It is seen that there is fair agreement between the GPS velocity data and the velocity predicted by the our simplistic one-dimensional model, and that again the current standardly used value of $C_o = 0.9$ lies within the range of plausible values for this parameter.

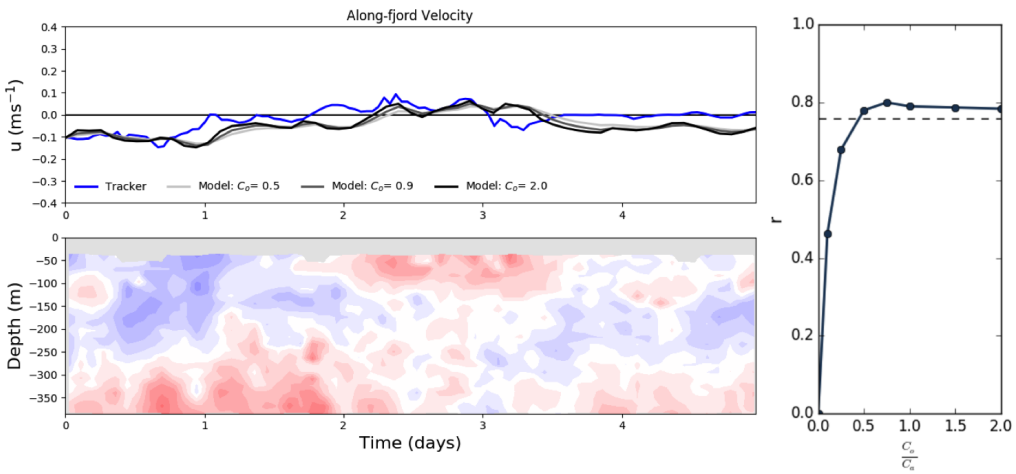



Figure 2.6: Top left: A comparison, for different values of the oceanic drag coefficient $C_o$, of the iceberg velocity directly measured using iceberg tracker data (Sutherland et al. 2014) and the model-predicted velocity of icebergs moving in the fjord at that time, from concurrent ADCP data. Bottom left: Ocean velocity data for the period over which the iceberg velocity was measured. The estimated draft of the iceberg on which the GPS tracker was placed is 300 m. Right: The correlation between the observed and modeled iceberg speeds for the entire PIES record, as a function of the drag coefficient ratio $C_o/C_a$.

As alluded to above, the value of the drag coefficients is related to the time taken for the iceberg to reach steady state and be in equilibrium with the currents and wind, with larger drag coefficients leading to faster equilibration. Considering the spin-up from a simplified momentum equation

$$\frac{\mathrm{d}u}{\mathrm{d}t} = \frac{\tau_o}{M}, \tag{2.10}$$

an iceberg of aspect ratio 2 spins up to its steady state velocity on the timescale of a day or two with the choice of drag coefficients above. The highest correlation between the modelled and observed iceberg speeds was obtained when the ocean currents and surface winds were averaged over a period beginning only 6 hours before the observed passage of the iceberg over the PIES and ending when the iceberg left the field of view of the sensor (right panel of Figure 2.7), rather than one to two days before the iceberg passed the PIES (right panel of Figure 2.7). Based on previous measurements of the

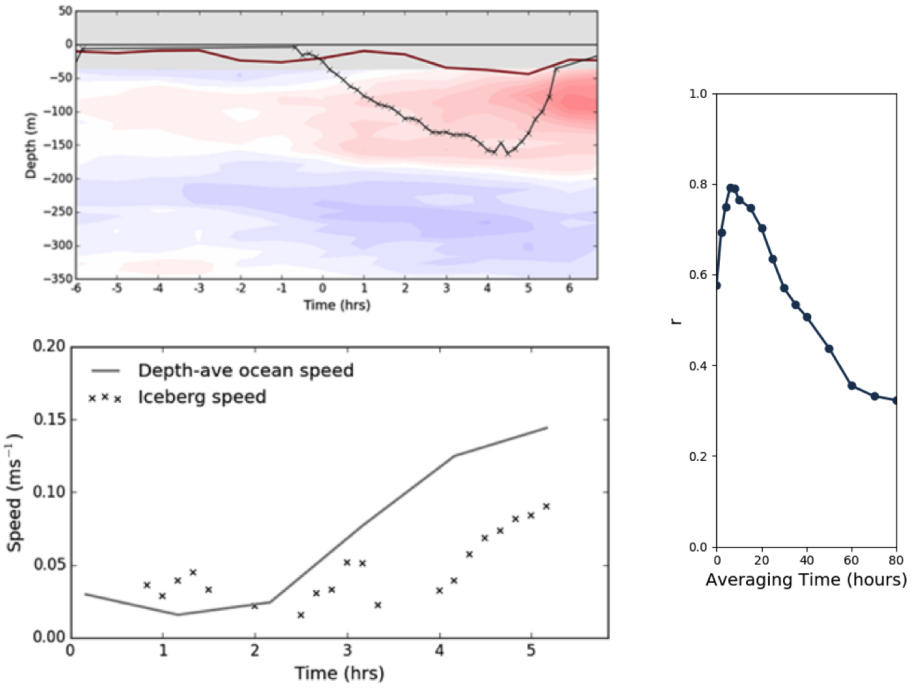



Figure 2.7: Top left: The PIES record and concurrent ADCP ocean velocity data for an iceberg passing the sensor during a period when the fjord flow was accelerating. The curvature of the PIES record is observed to increase over the observation period, indicating that the iceberg is accelerating. Bottom left: A comparison of the ocean velocity averaged over the iceberg's draft and the iceberg's speed (calculated from the curvature of the PIES record) over the event shown in the above panel. Right: The correlation between the observed and modeled iceberg speeds for the entire PIES record, as a function of the averaging time period used before the iceberg transit event.

ocean velocity during non-summer months (Jackson et al. 2014), the circulation in Sermilik Fjord is known to be dominated by shelf-forced flows, which have a timescale of several days. However, there are anomalies on top of the shelf-forced flow due to the tides and along-fjord winds (Oltmanns et al. 2015). As fjord winds and currents change on a diurnal timescale, and icebergs may accelerate or decelerate while passing the PIES (as seen in the event shown in the left panels of Figure 2.7), this favors a shorter averaging length.

## 2.5 Results

### 2.5.1 Typical Iceberg Transit Profiles

By combining our observational record of iceberg speeds and draft ranges with modelled iceberg velocity signs and precise drafts, we could fully describe icebergs' motion in the along-fjord direction during their transit over the PIES. For each iceberg passage event, we compared the iceberg's velocity and draft to the concurrent ADCP record of ocean currents to obtain the relative velocity profile felt by the iceberg.

The full distributions of the observed and modelled iceberg drafts and speeds are shown in Figure 2.8. The observed draft is the minimum possible iceberg draft, obtained by assuming the iceberg passed directly over the PIES. This is consequently skewed lower than the modelled iceberg draft with a mean of 149 m, compared to the modelled mean of 200 m. To model the iceberg draft, three drafts were considered for each observational record: the minimum possible iceberg draft associated with the iceberg passing directly over the sensor, the maximum possible iceberg draft associated with the iceberg passing tangentially to the ensonified region, and the mean of these two values. The modelled iceberg draft was taken as the one of these that gave a modelled speed closest to the observed speed. For icebergs with minimum drafts less than the critical value $d_{\text{lim}}$ defined in Andres et al. (2015), their maximum draft was equal to $d_{\text{lim}} = 252$ m. There is consequently a peak in modelled drafts around this value.

Panels C and D of Figure 2.8 show a fair qualitative agreement between the distribution of observed and modelled iceberg speeds. The correlation between the observed and modelled speeds is shown in full in Figure 2.9. The high correlation coefficient of 0.80 is supportive of the fact that a one-dimensional model of along-fjord winds and ocean currents is able to account for the leading order motion of icebergs in the fjord.

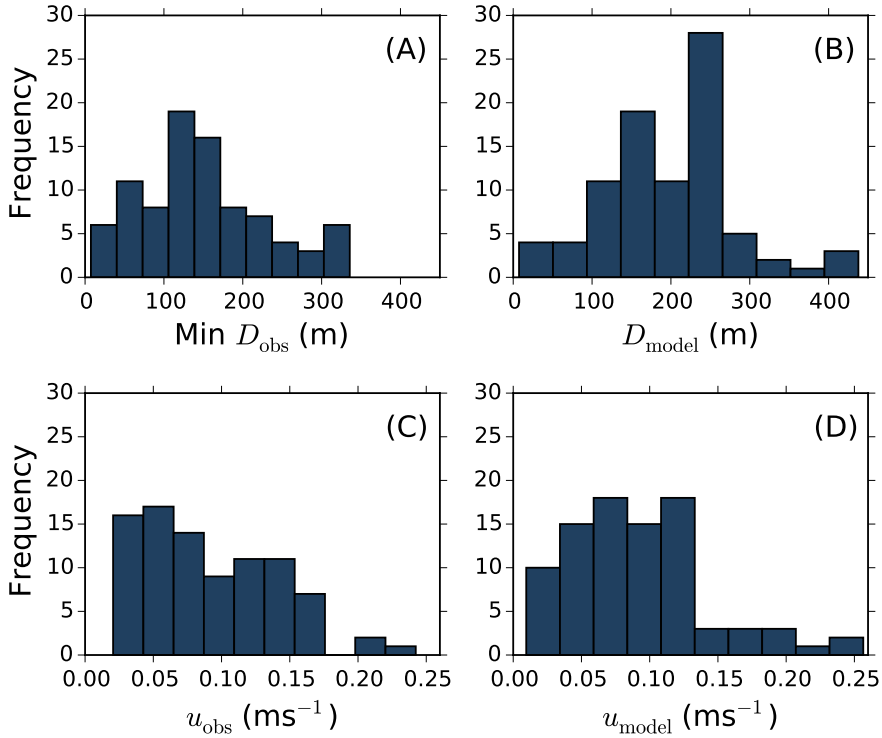



Figure 2.8: Distributions of observed and modelled iceberg speed and drafts: (A) Observed minimum iceberg draft; (B) modelled iceberg draft; (C) observed iceberg speed; and (D) modelled iceberg speed.

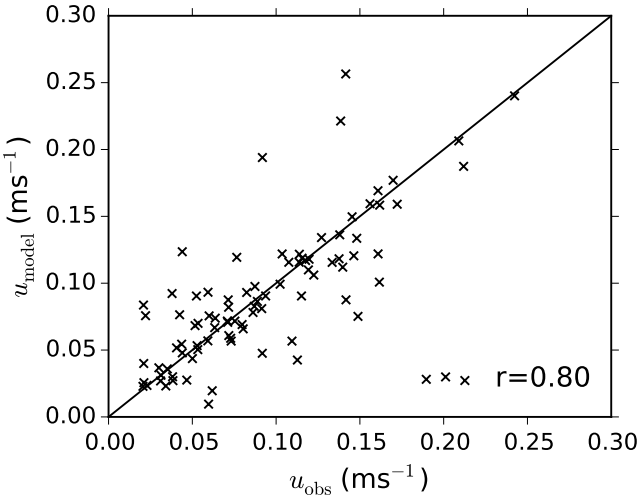



Figure 2.9: Correlation between observed and modelled iceberg speed, using the one-dimensional simplified model of iceberg motion.

A selection of typical velocity profiles felt by icebergs passing over the sensor is shown in Figure 2.10. It can be seen that, while some icebergs (e.g., Figure 2.10E and F) feel a homogeneous ocean velocity and hence experience little relative velocity with respect to the ocean, 80% of icebergs experience a range greater than 0.2 m $s^{-1}$ in ocean velocity over their draft and move with approximately the average of this profile. This average differs substantially from the surface velocity, whether taken as the velocity in the shallowest ADCP bin, or the linear extrapolation of the ADCP measurements to the surface layer. The largest vertical shear in the horizontal velocity is often associated with the transition from the PW to the AW layer in the fjord, and as such icebergs with drafts deeper than the average depth of this interface (180 m) are particularly prone to vertical shear.

Note that the velocity profiles depicted are time averages (from six hours prior to the iceberg's transit over the sensor until the time the iceberg leaves the field of view of the PIES), and instantaneous ocean velocity profiles can show even greater vertical shear. Further, even greater relative velocity magnitudes might be anticipated for grounded icebergs that no longer move with the vertically integrated ocean velocity.

### 2.5.2 Error Incurred from Neglecting Vertical Shear

Given the prevalence of vertical shear in the horizontal ocean velocity profiles from the observational record, it is of interest to iceberg modelling to quantify error incurred by using surface ocean velocities in the parameterizations of iceberg motion and melt. This can be calculated, in the case of a one-dimensional force balance model, only if neglecting wind stress. Using equation 2.5, the simplified model of iceberg motion becomes

$$\tau_o \equiv \rho_o C_o \int_{-D}^{0} |u_o(z) - u|(u_o(z) - u)\ \mathrm{d}z = 0. \tag{2.11}$$

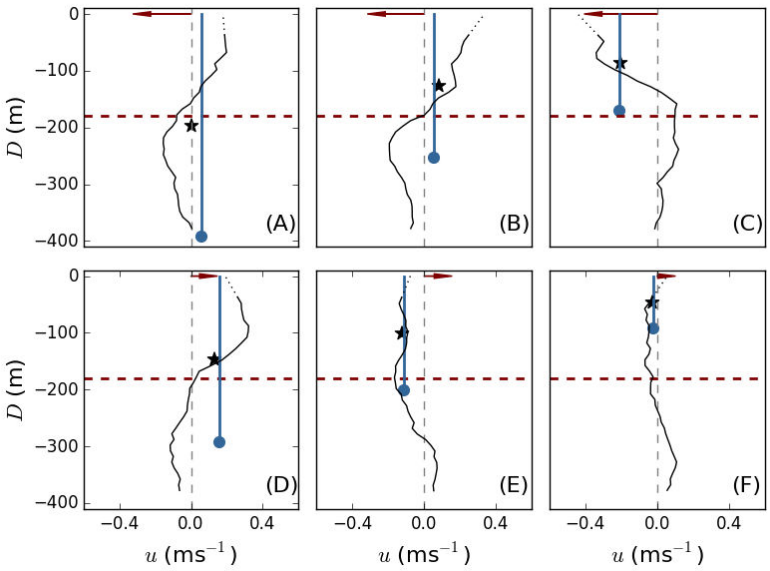



Figure 2.10: Example profiles of along-fjord velocities felt by icebergs. In each panel, the iceberg draft and velocity (from model-supplemented observations) are illustrated by the vertical blue line. The profile in black is the average ocean velocity during the passage of the iceberg over the sensor and the 6 hour period prior to its passage, with the extrapolated velocity in the top 40 m of the water column marked by the dashed extension of this profile, and the vertical average velocity over the iceberg draft marked by the black star. The wind speed and direction during the event are indicated by the red arrow (scaled by factor 5). The horizontal dashed lines indicate the average interface depth between the upper PW and deeper AW layers in the fjord (Jackson et al. 2014).

The absolute value within the integral makes this analytically intractable when $u_o - u$ changes sign over the iceberg draft, but proceeding by assuming $u_o - u$ has a constant sign, this is minimized as a function of $u$ when $u = \bar{u}$ for $\bar{u} \equiv \frac{1}{D}\int_{-D}^{0} u_o(z)\,\mathrm{d}z$. In contrast, if just the surface ocean velocity is considered, the equation of motion is

$$\tau_o \equiv \rho_o C_o D|u_s - u|(u_s - u) = 0, \tag{2.12}$$

and $u = u_s$ (where $u_s \equiv u_o|_{z=0}$). The error in iceberg speed incurred from neglecting the ocean shear is thus

$$E_u = |u_s - \bar{u}|\ . \tag{2.13}$$

We run our model twice, once calculating iceberg velocity using the full depth-varying ocean currents, and once using only the surface ocean currents. Differencing the resulting speeds gives the $E_u$, shown as a function of the theoretical error $|u_s - \bar{u}|$ in panel B of Figure 2.11. Divergences from the theoretical error may be attributed to the influence of winds in the model, not accounted for in the calculation above.

If in equation 2.2 for iceberg basal melt we assume that the relevant ocean velocity is the surface velocity and if the iceberg equations of motion are simplified as in equation 2.12, this parameterization unphysically gives that the iceberg experiences no basal melt. If instead, as observed, the iceberg moves with approximately a speed $\bar{u}$ and we consider the basal velocity $u_b = u_o|_{z=-D}$ as the relevant ocean velocity in equation 2.2, the basal melt rate (in units of m $\mathrm{d}^{-1}$) is given by

$$M_b = 0.58 \, \frac{T_o - T_i}{L^{0.2}} \, |\bar{u} - u_b|^{0.8} \, . \tag{2.14}$$

Again, 0.58 is a dimensional constant with units $^\circ\mathrm{C}^{-1}$ $\mathrm{m}^{0.4}$ $\mathrm{d}^{-1}$ $\mathrm{s}^{0.8}$. It follows that the error in the parameterized basal melt rate $E_{M_B} \sim |\bar{u} - u_b|^{0.8}$ and the largest melt rate error occurs when the basal velocity diverges significantly from the mean velocity.

The model-calculated $E_{M_b}$ is obtained by differencing the basal melt rate computed using the surface ocean velocity and assuming the iceberg feels the surface currents only in its equation of motion, and the basal melt rate computed using the ocean velocity at the bottom of the iceberg and allowing the iceberg to feel the ocean currents over its entire draft. This is compared to the difference between the average and basal velocities $|\bar{u} - u_b|$ in panel C of Figure 2.11. There is a broader spread in $E_{M_b}$ than in $E_u$ due to the dependence of $E_{M_b}$ on iceberg length $L$ through the factor $1/L^{0.2}$. In the model, $L$ is approximated as $2D$ (based on the characteristic aspect ratio of icebergs in Greenlandic fjords (Enderlin et al. 2016)). In calculating

melt rates, we assume a constant ocean temperature of 2°C, lying between that of the warmer AW and the cooler PW in Sermilik Fjord (Jackson et al. 2014). Note there are two sources of error in the parameterized basal melt rate; that incurred from moving the iceberg with just the surface currents, resulting in an incorrect iceberg speed, and that from melting the iceberg with the surface relative velocity as opposed to the basal relative velocity.

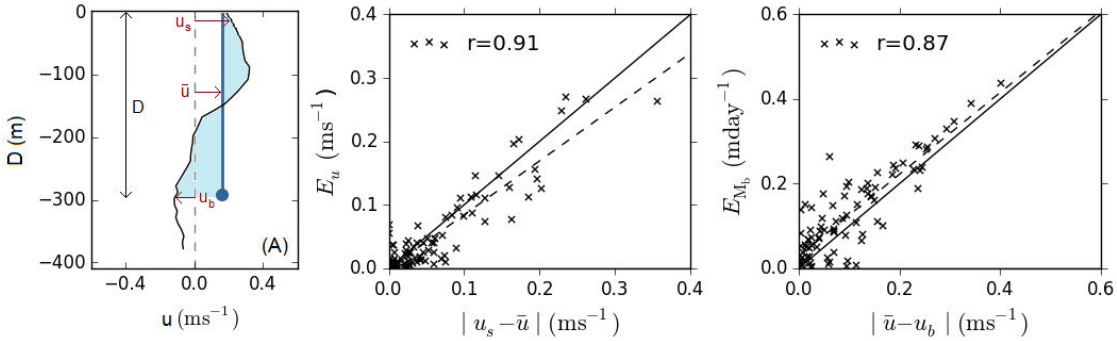



Figure 2.11: Dependence of error in iceberg velocity and melt on ocean shear. Panel A: Definition of surface speed $u_s$, average speed $\bar{u}$, and basal speed $u_b$ for an iceberg of draft $D$. Panel B: Error in iceberg speed due to applying the surface velocity as opposed to the depth-varying velocity in the model, as a function of the difference between the iceberg and the surface current $|u_s - \bar{u}|$. Panel C: Error in iceberg basal melt rate due to using the surface velocity rather than the basal velocity, as a function of the difference between the iceberg and the basal current $|\bar{u} - u_b|$. The best fits in (B) and (C) are marked with dashed lines, and the corresponding correlation coefficients labelled.

### 2.5.3 Discussion

The mean iceberg speed in our observational record was around 0.1 m s$^{-1}$, and the mean difference $|\bar{u} - u_s|$ was 0.06 m s$^{-1}$, indicating an average speed error of 60% from using, in the momentum equation, surface ocean currents as opposed to ocean currents over the full depth of the iceberg. This error increased to 0.26 m s$^{-1}$ (260% of mean iceberg speed) for the maximum difference of 0.36 m s$^{-1}$.

For the parameterization of iceberg melt in climate models, ocean velocity enters through the basal melt term $M_b$, which (using the standard parameterization) may

typically be up to 1 m $d^{-1}$ (Bigg 2016) in the open ocean. For icebergs in Sermilik Fjord, Enderlin and Hamilton (2014) estimate a total submarine melt rate of 0.39 m $d^{-1}$. Based on an ocean temperature of 2°C, the mean basal melt rate in our study when using $u_b$ for ocean velocity was 0.17 m $d^{-1}$, varying between 0.01 m $d^{-1}$ and 0.49 m $d^{-1}$. The mean $E_{M_b} = 0.12$ m $d^{-1}$ represents an error of 71% relative to this mean melt rate, and increases to a 259% error for the maximum $E_{M_b} = 0.44$ m $d^{-1}$. The total iceberg melt rate is the sum of side melt and wave erosion in addition to basal melt. Consequently the error in the basal melt term will affect more those icebergs and environments in which bottom melt dominates, namely tabular icebergs in relatively warm waters.

While there has been some recent modelling effort to include in icebergs' equation of motion the ocean currents over the range of their draft (Kubat et al. 2005, 2007; Hill and Condron 2014; Marsh et al. 2015; Merino et al. 2016), we are unaware of any effort to account for the effect of shear on iceberg melt. Here, we have limited our discussion to the effect of a sheared flow on the bottom melt of icebergs. However, it is anticipated a nonzero relative velocity will also influence the side melt of icebergs, despite this term not being present in the current parameterization. This would further add to the error incurred by using surface ocean velocities to estimate iceberg melt. The incorporation of a relative velocity into the parameterization of the side melt of icebergs is the focus of Chapter 3.

## 2.6 Conclusions

In this chapter we have discussed a unique iceberg and ocean velocity record in Sermilik Fjord, southeast Greenland. Iceberg motion in the fjord was shown to be dominated by the vertical average of the ocean currents over the draft of the iceberg. Perhaps as a consequence, icebergs with drafts close to the interface between the

upper PW and lower AW layers in the fjord had the fastest observed speeds, being least affected by the shear between the ocean layers or surface drag. It was found that strongly vertically sheared flows significantly impact iceberg velocity and basal melting, with average errors of 60% in modelled speed and 71% in modelled basal melt if this shear is neglected. These large error values highlight the importance of including depth varying ocean velocities in parameterizations of iceberg motion and melt.

The evidence presented that icebergs are subject to strongly vertically sheared flows over their draft emphasizes the need for a new parameterization of the side melt of icebergs that takes into account the effect of ambient velocity. The effect of ocean current vertical shear on icebergs may be particularly important when computing the heat and salinity budget of Greenlandic fjords, due to their strongly sheared nature and the fact iceberg melt inside these fjords is a major contributor to freshwater export (Jackson et al. 2014). Although currents around Antarctica are typically less sheared than those in Greenlandic fjords, dimensions of Antarctic icebergs can be an order of magnitude larger than those observed around Greenland (Savage 2001). The large drafts of giant icebergs calving into the Southern Ocean means that there may still be significant variation in ocean velocity over the draft of the iceberg. In such cases, a consideration of the shear felt by the iceberg may also improve the modelling of icebergs. The influence of a background velocity on iceberg melting is the focus of the following chapter.

# Chapter 3

# Laboratory Experiments: Ice Melting in a Background Flow

## 3.1 Part I: Ice Melting in a Homogeneous Flow

Analogously to tidewater glaciers, one primary mechanism involved in iceberg melt are meltwater plumes rising along the ice-ocean interface. In a recent study by Yankovsky and Yashayaev (2014), detailed surveys of two Greenlandic icebergs revealed that icebergs subject to different oceanic and atmospheric conditions may have melt plumes with very different surface expressions. Yet to date, parameterizations of iceberg melt in climate models have neglected the influence of melt plumes on Submarine Melt Rate (SMR) and the location where meltwater is discharged in the water column. Recent work indicating that icebergs in Greenlandic fjords are frequently subject to strongly vertically sheared flows (Chapter 2; FitzMaurice et al. (2016)) further highlights the need for a consistent parameterization of iceberg melt that takes the influence of ocean currents on melt plumes into account. In addition to its effect on SMR, flow past an iceberg is anticipated to alter the melt plume mixing and entrainment, and hence the intrusion depth of the modified meltwater layer.

In this chapter, we use laboratory experiments to investigate the effect of flow past an iceberg on iceberg melt plumes and the distribution of meltwater in the water column. The current state of scientific knowledge about submarine iceberg melt is summarized in Section 3.2, the experiments carried out to deduce the effect of flow past an iceberg on iceberg side melt plumes are described in Section 3.3, and their results are described in Section 3.4. An updated parameterization of iceberg side melt accounting for side melt plumes is introduced in Section 3.5.1, and is applied to observed icebergs in Section 3.5.4. Discussion and conclusions follow in Sections 3.6 and 3.7. The second half of this chapter, starting in Section 3.8, proceeds by expanding this work to the case of a vertically sheared flow.

## 3.2 Background

Our existing understanding of icebergs' submarine melting is derived from a combination of observations, laboratory experiments, and mathematical modelling. Studies of individual icebergs and iceberg distributions have allowed ballpark estimates of their melt rate and deterioration as a function of ocean temperature (Budd et al. 1980; Hobson et al. 2011) and, more recently, satellite altimetry has been used to constrain iceberg mass loss over time (Enderlin and Hamilton 2014; Enderlin et al. 2016). Hydrographic surveys conducted near melting icebergs have shown that icebergs can locally influence ocean properties, with iceberg melt plumes displaying enhanced upwelling and cooled temperatures (Josberger and Neshyba 1980; Helly et al. 2011; Stephenson et al. 2011). Laboratory experiments have investigated in depth the influence of vertical temperature and salinity gradients on SMR, the shape evolution of melting ice, and the distribution of meltwater assuming no background flow (Huppert and Turner 1980; Russell-Head 1980; Gade 1993; McConnochie and Kerr 2016).

Observational and experimental findings have informed the development of parameterizations of iceberg melt (Weeks and Campbell 1973; Neshyba and Josberger 1980; El-Tahan et al. 1987), used to predict the large-scale distribution of meltwater along modelled iceberg trajectories (Bigg 2016; Gladstone et al. 2001; Kubat et al. 2007). Current parameterizations of iceberg side melt $M_s$ separate melting into forced convection $M_b$ due to heat exchange driven by flow past the iceberg, and a velocity-independent buoyant convection term $M_v$ that is small in comparison to $M_b$ (Savage 2001). Some numerical models apply $M_v$ to calculate side melt and thus have an entirely velocity-independent side melt rate (Martin and Adcroft 2010), while others, in units of m $d^{-1}$, take

$$M_s = M_v + M_b, \tag{3.1}$$

$$= (aT_o + bT_o^2) + K\ |\vec{u_i} - \vec{u_o}|^{0.8}\ \frac{T_o - T_i}{L^{0.2}} \tag{3.2}$$

for water temperature $T_o$ (°C), ice temperature $T_i = -4$°C, $L$ being the iceberg length (m), and $|\vec{u_i} - \vec{u_o}|$ the relative speed between the iceberg and the water (m $s^{-1}$). Here, $a = 7.62 \times 10^{-3}$ m $d^{-1}$ °$C^{-1}$, $b = 1.29 \times 10^{-3}$ m $d^{-1}$ °$C^{-2}$ (Neshyba and Josberger 1980), and $K$ is a function of the water temperature (Weeks and Campbell 1973). As in Chapter 2, $K$ is a dimensional constant with units °$C^{-1}$ $m^{0.4}$ $d^{-1}$ $s^{0.8}$, and is typically taken as 0.58 for oceanic conditions (see Section 3.5.2 for details).

The form of $M_v$ was obtained from an empirical fit to observations of icebergs melting in different temperature water (Neshyba and Josberger 1980) while $M_b$ is derived from the theory of flow past an isothermal plate (Weeks and Campbell 1973), but there has been no formal consideration given to whether $M_v$ and $M_b$ are additive, or to the effect of vertical melt plumes parallel to the ice. Work has been done to explicitly account for melt plumes in the case of melt under ice shelves and at the faces of tidewater glaciers, for which the canonical parameterization is the three-equation

model of Holland and Jenkins (1999). In this parameterization it is found that the velocity along the ice face (corresponding to the melt plume velocity) can act as a strong control on the melt rate, with fast melt plumes inducing much more melting than slow melt plumes (Sciascia et al. 2013). While incorporating a velocity that is parallel to the ice face (the rising buoyant plume's velocity), this parameterization does not allow for lateral flow around the ice and perpendicular to the melt plume. It consequently does not account for the influence of a background advective velocity on melting, either directly or via the flow's interactions with melt plumes. It is the effect of such a velocity that is the focus of this study.

## 3.3 Methods

### 3.3.1 Experimental Configuration

A fresh ice block was suspended in a re-circulating flume filled with room temperature (18-21°C) seawater (salinity $S \approx 32$ g kg$^{-1}$), such that it was unable to move, so the flow was equivalent to that observed in the iceberg's frame of reference (Figure 3.1). The experiments were conducted in a 300 x 500 cm tank, in which the flow speed could be continuously adjusted between 0 and 5 cm s$^{-1}$. The ice block had width 15 cm, length 10 cm, and immersed height 10 cm, and was suspended in 20 cm of water. The ice was de-aired and dyed so the spreading of meltwater could be observed. The ice block melted over an observation period of 15 minutes, and the SMR was calculated from the ice block mass difference scaled by its average surface area, as described in Section 3.3.2. Note that this gives the total side and basal SMR, although basal melt makes a small contribution to the total mass loss (see Section 3.3.2).

The experimental configuration used in this study addresses the effect of ambient velocity on the side melt of icebergs in isolation of other factors (e.g. stratification,

ice roll-over). The ice was frozen with a slim wooden stick running down its center. This wooden stick was clamped to a bar above the tank to prevent the ice block from rolling. We hypothesize that if an iceberg rolls, its shape is changed, but the proposed side melt parameterization should still hold for the new iceberg geometry.

In the absence of a background flow, melting occurs on all sides of the ice block, with the generation of rising meltwater plumes on each of the four vertical faces of the block. These melt plumes are also fed by buoyant basal melt, and rapidly become turbulent for ice melting in room temperature water. They result in the surface pooling of meltwater, which spreads uniformly away from the ice block. By increasing the velocity of the flow past the ice block, we proceeded to test its influence on the melt plumes and SMR.

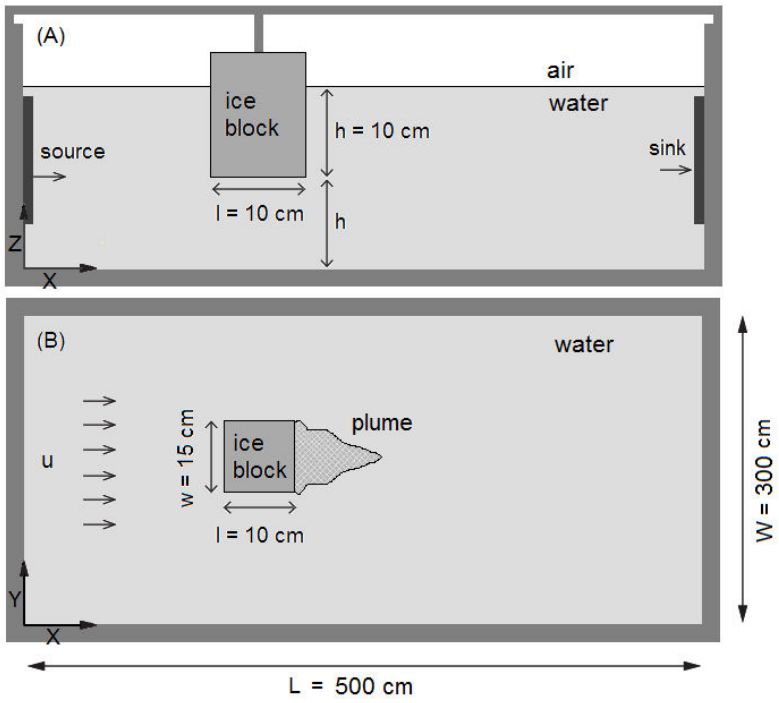



Figure 3.1: Schematic (not to scale) of the laboratory setup. (A) Side-view of the ice block suspended in the working part of the flume. (B) Birdseye view of the ice block, with the surface expression of a downstream melt plume hatched.

### 3.3.2 Calculation of SMR

The SMR (cm $\text{min}^{-1}$) was calculated using the formula

$$\text{SMR} = \frac{\text{d}W}{\rho_i A_{\text{ave}} \text{d}T,} \tag{3.3}$$

where d$W$ is the ice block mass difference (kg) over the course of an experiment of length d$T$ (min), $\rho_i \equiv 0.92 \times 10^{-6}$ kg $\text{cm}^{-3}$ is the density of the ice, and $A_{\text{ave}}$ ($\text{cm}^2$) is the average surface area of the block over the course of the experiment.

In what follows, we will assume that the measured mass loss in the present laboratory experiments is predominantly due to side melt. This is justified by the aspect ratio of the ice blocks used in our experiments, as the basal area of 150 $\text{cm}^2$ is less than one third of the side area of 500 $\text{cm}^2$. Despite the smaller basal area however, this assumption would not hold if the basal melt rate was large compared to the side melt rate. To assess this, we analyzed videos of the ice block melting to separate the total SMR into its side and basal components by tracking the edge of the ice block in each of these regions over the course of the experiments. The results of this analysis are illustrated in Figure 3.2, which shows that the basal SMR is less than the side SMR, and that the nonlinear melt behaviour discussed later in this chapter is still present in the side SMR. Note that the video-derived SMRs have a larger error than the measured SMRs as the video only shows a two-dimensional side view of the ice block, and edge-tracking loses accuracy when the ice block melts such that there is curvature in the plane perpendicular to the plane of view of the camera. The right panel of Figure 3.2 shows that the small basal melt rate acting on a small area leads to an average contribution of basal melt of just 19% to the total melt volume. This is only approximately twice the average experimental error in this study of 9%.

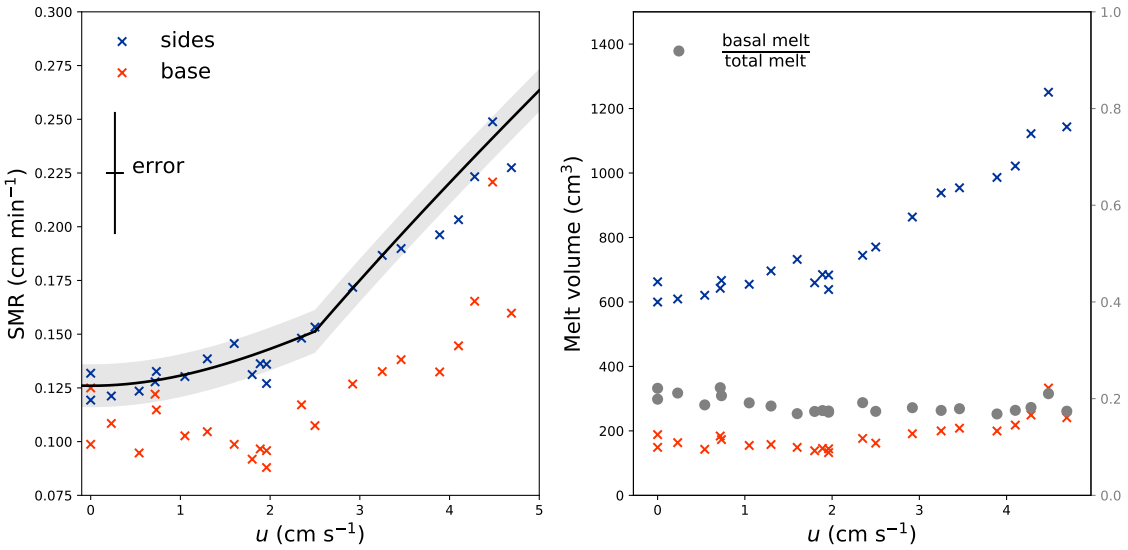



Figure 3.2: Left: Side (blue crosses) and basal (red crosses) SMRs as a function of ambient flow speed, calculated from tracking the ice edge in each of these regions in the experiment videos. The updated side melt parameterization (solid line) and laboratory error (gray shading) of the SMRs calculated from the mass loss over the course of the experiments, as discussed in Section 3.4 and seen in Figure 3.4, are shown for reference. Right: Total side and basal melt volumes as a function of ambient flow speed, calculated by scaling the SMR in the left panel by the experiment length and the side/basal area, respectively. The proportion of the basal melt to the total melt is shown by the gray circles.

## 3.4 Results

We found that in general melt rate increases with flow speed, though nonlinearly. Qualitatively, we observed that melt plume behaviour differs for low and high background flow speeds (Figure 3.3), and that this quantitatively impacts the dependence of SMR on flow speed (Figure 3.4). At low (<1.5 cm s$^{-1}$) flow speeds, the ice melted uniformly (Figure 3.3A), maintaining its rectangular profile save for a slight upward slope of the bottom face in the direction of the flow associated with vortex formation as water moved under the ice block. At these flow speeds, the meltwater rose uniformly in plumes around the ice block, and spread in a surface layer. There was some sinking observed of filaments of ambient salt water that had been more cooled

conductively than freshened by the meltwater, but the majority of the motion was upwards.

A qualitative change was observed in the profile of the ice block once the background flow speed exceeded 1.5 cm $s^{-1}$. A corner appeared on the upstream face of the ice block (Figure 3.3B), associated with the upstream melt plume being swept under and around the ice. The separation of the upstream plume meant that some of the meltwater no longer rose uniformly around the ice block to form a surface layer; rather, it began to mix with the ambient water, and enter the water column also over the full draft of the ice block. When the background flow was increased to 2.5 cm $s^{-1}$, the downstream melt plume also fully separated from the ice block, and a second qualitative change was observed in the ice block profile. The upstream corner shifted lower on the ice block, and a downstream corner appeared, giving the melted ice block a pear-shaped appearance (Figure 3.3C). At flow speeds exceeding 2.5 cm $s^{-1}$, there was a high level of mixing between the melt and ambient water downstream of the ice block, as evidenced by the highly diluted dye downstream of the ice block, and no surface pooling of meltwater.

The change in melt plume behaviour (from fully attached below 1.5 cm $s^{-1}$ to fully detached above 2.5 cm $s^{-1}$) was associated with a distinct increase in the dependence of SMR on flow speed $u$ (Figure 3.4). Physically, this results from the flow past the ice block influencing the ice block SMR in two ways. Firstly, it modulates advective heat transport to the ice surface, resulting in the observed linear increase of SMR with $u$ in each of the two melt plume regimes. Secondly, the background flow interacts with the melt plume as it rises, altering the angle the plume makes with the side of the ice block. If the plume is attached, the relatively cold water contained in the plume insulates the ice surface from the ambient water, so separating the plume from the ice enhances melting and causes the regime shift in Figure 3.4. We hypothesize that the regime transition (attached to detached plumes) occurs when the background flow

speed $u$ is of the same order of magnitude as the plume speed $w$. This is supported by the fact that the mean observed melt plume speed (calculated via feature-tracking) was 1.6 cm $s^{-1}$, with a two standard deviation range of $w \sim 1.2 - 2.2$ cm $s^{-1}$.

For tidewater glaciers it has been argued that increasing the strength (buoyancy flux) of the melt plume by supplying subglacial discharge enhances melting of the glacier face, as stronger (faster/wider) plumes entrain more warm ambient water and draw it towards the ice front (Cenedese and Gatto 2016; McConnochie and Kerr 2016). However, in the case of icebergs it is possible to detach this melt plume entirely, allowing the ice to come directly in contact with the warm ambient waters, which are consistently renewed by the advecting background flow. So while those familiar with the tidewater glacier literature correctly associate stronger melt plumes with increased melting, an entirely absent melt plume results in even greater melting, provided the warm ambient water is continually renewed.

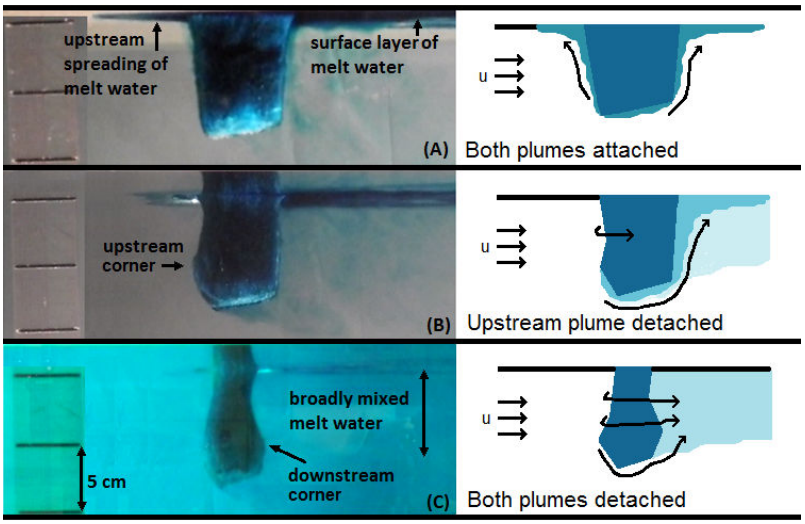



Figure 3.3: Left: Side views of ice blocks after melting for 15 min in a homogeneous flow of (A) 0.5 cm $s^{-1}$, (B) 2 cm $s^{-1}$, and (C) 4.7 cm $s^{-1}$. Scale shown by ruler with 5 cm intervals. Right: Schematic representations of left panels.

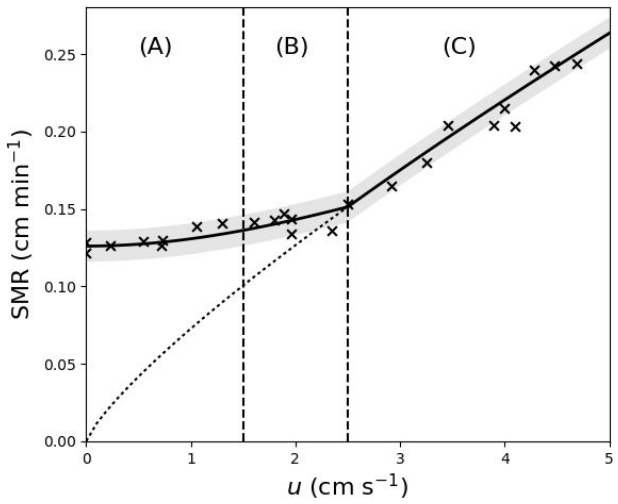



Figure 3.4: Dependence of SMR on flow speed, split into regions (A) both plumes attached, (B) upstream plume detached, downstream plume attached, and (C) both plumes detached. The parameterization proposed in equation 3.5 for an average ice temperature of -15°C is shown in black, and the shaded region depicts the experimental error (calculated from two standard deviations of 3 repeated experiments). The dashed extension of the detached regime curve is the standard parameterized value of $M_b = Ku^{0.8}(T_o - T_i)/L^{0.2}$ (where $K = 0.75$ °C$^{-1}$ m$^{0.4}$ d$^{-1}$ s$^{0.8}$, $T_o = 20$°C, $T_i = -15$°C, and $L = 0.1$ m in the laboratory setting).

## 3.5 Parameterizing Side Melt

### 3.5.1 Model

Following our experimental findings, we update the iceberg side melt parameterization to be dependent on the melt plume behavior. In developing this parameterization, we assume that side melt dominates the laboratory-measured SMR, as the aspect ratio of the ice blocks is such that the side area dominates (see Section 3.3.2). When the relative speed of the iceberg and the ambient water is less than the plume speed ($|u_o - u_i| < |w|$), i.e. when the melt plume is attached, the side melt rate is estimated using the melt parameterization due to forced convection, where the relevant speed, temperature, and lengthscale are the plume vertical speed $|w|$, the plume temperature $T_p$, and the iceberg draft $D$, respectively. For $|u_o - u_i| > |w|$, i.e. when the melt plume is detached, the side melt rate is instead estimated using the previous

standard parameterization due to forced convection with ambient relative flow speed $|u_o - u_i|$ and ambient water temperature $T_a$ past an iceberg of length $L$. We assume that the plume water is a mix of ambient water at $T = T_a$ and meltwater at $T = 0°\text{C}$, so $T_p = \alpha T_a$ with the fraction $\alpha$ of entrained water to meltwater proportional to the magnitude of the flow:

$$\alpha = \alpha_0 \sqrt{u^2 + w^2}, \tag{3.4}$$

where the constant $\alpha_0$ has units of $\text{m}^{-1}$ s, and is defined below.

With this model, the side melt rate $M_s$ in m $\text{d}^{-1}$ is

$$M_s = \begin{cases} \dfrac{K|w|^{0.8}(\alpha T_a - T_i)}{D^{0.2}} & |u_o - u_i| \leq |w| \\ \dfrac{K|u_o - u_i|^{0.8}(T_a - T_i)}{L^{0.2}} & |u_o - u_i| > |w|, \end{cases} \tag{3.5}$$

where $K$ is found to be approximately 0.58 $°\text{C}^{-1}$ $\text{m}^{0.4}$ $\text{d}^{-1}$ $\text{s}^{0.8}$ for icebergs in the ocean, and 0.75 $°\text{C}^{-1}$ $\text{m}^{0.4}$ $\text{d}^{-1}$ $\text{s}^{0.8}$ in the laboratory setting (see Section 3.5.2). With the laboratory-appropriate value of $K$, equation 3.5 gives the curve shown in Figure 3.4 for an average $T_i$ of $-15°\text{C}$. Here, $\alpha_0$ is chosen to be $1/\sqrt{2}w$ $\text{m}^{-1}$ s to ensure continuity between the two regimes in the case $D = L$. This parameterization improves upon the previous standard parameterization of iceberg side melt (equation 3.2) that does not account for the two dynamically different melt plume regimes, and unlike the three-equation parameterizations of melt (generally applied under ice shelves or along tidewater glacier faces) it considers the influence of a velocity that is normal to the plume direction, which is uniquely the case in iceberg side melt.

### 3.5.2 Parameterization Constants

The melt rate due to forced convection $M_b$ is derived from the theory of heat exchange for flow past a body of length $L$. The derivation of this parameterization is considered in depth in Section 4.4.1, but for now it suffices to note that this melt rate (in units

of m $d^{-1}$) takes the form

$$M_b = \frac{k\mathrm{Nu}(T_o - T_i)}{\rho_i \Gamma L}, \tag{3.6}$$

for thermal conductivity $k$ (W $m^{-1}$ $°C^{-1}$), water temperature $T_o$ (°C), ice temperature $T_i$ (°C), ice density $\rho_i$ (kg $m^{-3}$), and latent heat of fusion $\Gamma$ (J $kg^{-1}$) (Weeks and Campbell 1973). The Nusselt number Nu may be approximated as $\mathrm{Nu} = C\mathrm{Re}^m\mathrm{Pr}^{1/3}$, where $C$ and $m$ are functions of the Reynolds number Re and the shape of the body, and Pr is the Prandtl number. Thus substituting for Re= $|u_i - u_o|L/\nu$ (with$|u_o - u_i|$ the relative speed between the iceberg and the water in m $s^{-1}$, and $\nu$ the kinematic viscosity in $m^2$ $s^{-1}$), $M_b$ in units of m $d^{-1}$ is

$$M_b = K\ |u_o - u_i|^m\ \frac{T_o - T_i}{L^{1-m}}, \tag{3.7}$$

where

$$K = \frac{86400k\mathrm{Pr}^{1/3}C}{\rho_i \Gamma \nu^m}, \tag{3.8}$$

and the multiplicative factor 86400 is applied to convert from units of m $s^{-1}$ to the standardly used iceberg melt rate units of m $d^{-1}$. For flow past a flat plate, $C = 0.037$ and $m = 0.8$ (Weeks and Campbell 1973). So for ocean waters at approximately $T_o \sim 0°C$, for which $k = 0.563$ W $m^{-1}$ $°C^{-1}$, Pr= 13.1 and $\nu = 1.826 \times 10^{-6}$ $m^2$ $s^{-1}$, we find that $K = 0.58$ $°C^{-1}$ $m^{0.4}$ $d^{-1}$ $s^{0.8}$. In the laboratory setting ($T_o = 20°C$), the parameters instead have values $k = 0.6$ W $m^{-1}$, Pr=7.01, and $\nu = 1.004 \times 10^{-6}$ $m^2$ $s^{-1}$, giving $K = 0.75$ $°C^{-1}$ $m^{0.4}$ $d^{-1}$ $s^{0.8}$.

In the updated parameterization for submarine melting along the iceberg sides $M_s(u, T_a)$ described above (equation 3.5), it remains to specify the constant $\alpha_0$ in the expression $T_p = \alpha_0\sqrt{u^2 + w^2}T_a$. This $\alpha_0$ may be chosen to ensure continuity in the case $D = L$ by taking $\alpha_0 = 1/\sqrt{2}w$ $m^{-1}$ s. In the laboratory experiments we use $|w| = 0.024$ m $s^{-1}$, based on the observed velocity at which the regime transition is observed in the data (Figure 3.4), and $T_a = 20°C$. Under oceanic conditions, models

of the melting of ice faces have found typical plume speeds to be of order 0.05 m $s^{-1}$ (Sciascia et al. 2013), which is consistent with the plume speed of 0.07 m $s^{-1}$ observed next to a grounded iceberg by Josberger and Neshyba (1980).

### 3.5.3 Comments on the Experimental Limitations

For simplicity, we performed our experiments, which were concerned with the dynamical response of side melting to a background velocity, in an unstratified room temperature flow. We expect the occurrence of attached/detached plumes to persist at lower water temperatures. However, the melt plume velocity will be smaller at lower temperatures, due to the smaller buoyancy flux, and the transition between the attached and detached regimes is expected to occur at a lower background velocity in dimensional units (this is accounted for in the updated parameterization by non-dimensionalizing the regime transition with the plume speed). However, we still expect to observe a nonlinear dependence of side melt on the relative flow speed, even if the experiments were carried out with lower water temperatures.

The temperature of the ice was measured by inserting HOBO temperature probes near the center of the ice block. The temperature of the ice block when the experiment starts is $\sim -20°C$, and it warms from this value to $-5°C$ over the course of the experiment, maintaining an average temperature between $-10$ and $-15°C$. With this average ice temperature the updated melt parameterization accurately describes the side melt rate measured in the laboratory experiments (Figure 3.4). We performed 4 experiments, covering a range of flow speeds, in which the ice block mass difference was measured every 3 minutes throughout the 15 minute experiment. From the mass difference, the melt rate was calculated at 3-minute intervals using equation 3.3. The melt rate exhibited a slight decrease over time, however the magnitude of this decrease was within the experimental error.

### 3.5.4 Application to Observations

We apply this updated parameterization of side melt to observations of 90 icebergs from Sermilik Fjord in southeastern Greenland, described in Chapter 2 (FitzMaurice et al. (2016), hereafter). FitzMaurice et al. (2016) showed that these icebergs move predominantly with the vertical average of ocean currents over their draft. If currents are approximately uniform with depth, this means the iceberg experiences very little relative velocity with the ocean and it will be in the attached plume regime at every depth. Alternatively, if there is a shear between the upper Polar Water and lower Atlantic Water layers in the fjord, the iceberg moves at the average of the layer speeds (weighted by how much of its draft is in each layer) and experiences a high relative velocity with the ocean, so it will be everywhere in the detached plume regime. These two scenarios (approximately barotropic and linear shear, respectively) are illustrated in Figure 3.5, and are representative of the majority of the relative velocity profiles felt by the icebergs in the observational record of FitzMaurice et al. (2016). Thus, although the updated parameterization was developed for a homogeneous flow, we expect it to perform well in the real ocean as most icebergs fall into a single plume regime at every depth.

A further effect of vertical shear in the ambient current is that the parameterization will lead to an underestimate of SMR in regions where the relative speed transitions between the attached and detached regimes if an average ocean velocity is used (by the nonlinearity of equation 3.5). We therefore proceed by applying the updated paramaterization to calculate the velocity and temperature-dependent SMR at every depth. We represent the thermal stratification of the fjord via an ocean temperature of 1°C above 180 m in the Polar Water layer, and 3°C below this depth in the Atlantic Water layer (Straneo et al. 2011). Note that the schematic representations of expected melt plume behavior (Figure 3.5) assume a weakly stratified ocean, or an iceberg entirely in the homogeneous top layer of the fjord. In the presence of

a strong linear stratification the attached plume regime could lead to an intrusion at depth as opposed to a surface meltwater layer (Huppert and Turner 1980).

Figure 3.6 shows that when the melt plumes are detached, the updated parameterization is almost identical to the standard parameterization (equation 3.2), with the only difference being the small term $M_v$ (equation 3.2). However, in the attached plume regime (which constitutes 40% of the icebergs in the observational record) the inclusion of the plume velocity in the side melt parameterization approximately doubles the mean side melt, from 0.06 m $d^{-1}$ to 0.10 m $d^{-1}$, if the icebergs are assumed to have an aspect ratio equal to 1 and the ice temperature is the canonical value of $T_i = -4°C$ (Bigg et al. 1997). This parameterization is sensitive to the ice temperature, and if instead we assume that $T_i = -15°C$ as in Lüthi and Funk (2001), the mean side melt given by the updated (standard) parameterization for all icebergs increases to 0.40 m $d^{-1}$ (0.34 m $d^{-1}$). Although when both regimes are considered the updated parameterization differs less from the standard parameterization than in the attached regime alone, this latter mean value from the updated parameterization agrees more closely with area-averaged SMRs estimated for icebergs in Sermilik Fjord by Enderlin and Hamilton (2014) of 0.39 m $d^{-1}$. Variations about the mean are caused by the proportion of each observed iceberg in either fjord layer being a function of the iceberg draft, and observed icebergs being subject to different ocean velocity profiles. The side SMR suggested by this parameterization at $T_i = -15°C$ results in 146 m of side melt per year, consistent with iceberg tracking studies around Greenland (Sutherland et al. 2014) that indicate icebergs ranging in horizontal size 100 to >500 m survive for at least 80 days in Sermilik Fjord.

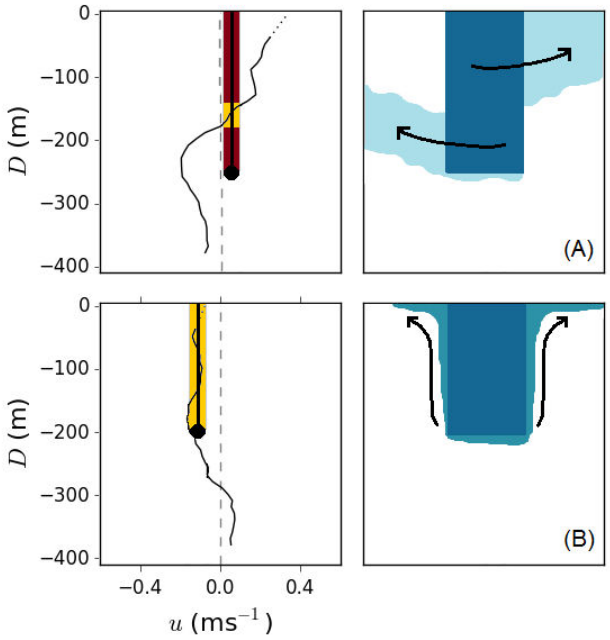



Figure 3.5: Left: Sample profiles of along-fjord velocities felt by two icebergs in Sermilik Fjord, from FitzMaurice et al. (2016), in (A) a linearly sheared flow and (B) a barotropic flow. The solid vertical line indicates the iceberg draft and velocity, and the profile (thin black line) is the average ocean velocity during and leading up to the iceberg's observation, with the dashed extension of this profile illustrating the extrapolated velocity in the top 40 m of the water column. Depths at which the relative velocity of the ocean is sufficiently low that we would anticipate an attached plume are shaded in yellow, and depths where it is high enough for the melt plume to detach are shaded in red. We assume a plume speed of 0.05 m $s^{-1}$ following the modelling of melting ice faces by Sciascia et al. (2013), which is consistent with the plume speed of 0.07 m $s^{-1}$ observed next to a grounded iceberg by Josberger and Neshyba (1980). Right: Schematics of plume regimes for (A) detached and (B) attached plumes corresponding to linearly sheared flow and barotropic flows, respectively.

## 3.6 Discussion

We began by noting the importance of understanding how icebergs melt in different ocean conditions and where this meltwater goes in the water column for predictions of future ocean circulation and biological productivity. A further consideration relates to the observed increase in Antarctic sea ice extent over the last few decades (Hobbs et al. 2016), despite rising temperatures around Antarctica. One hypothesised mechanism contributing to this trend is an increased discharge of freshwater into the Southern

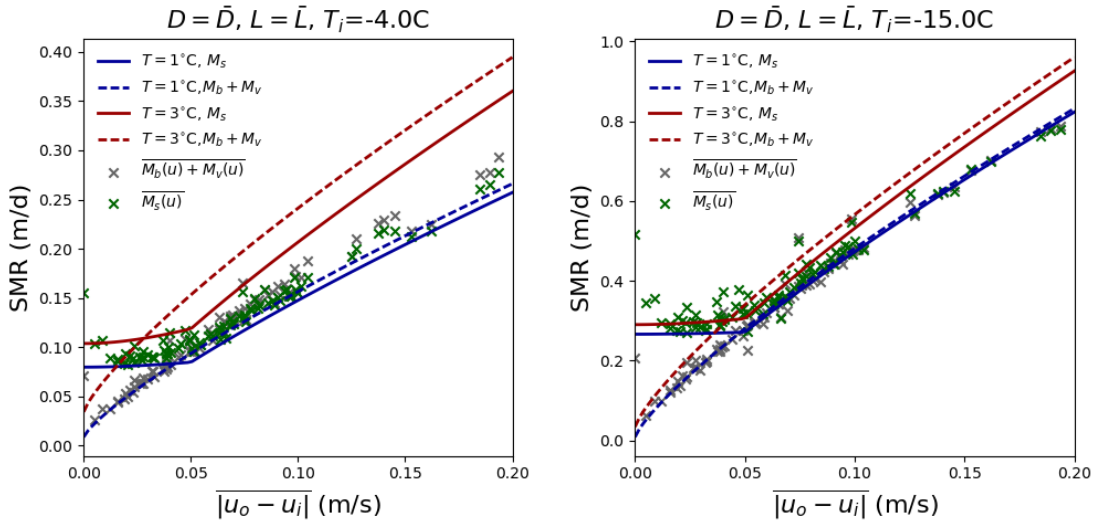



Figure 3.6: A comparison of the old (gray) and new (green) parameterized iceberg side melt rates for the 90 icebergs in the observational record presented in Chapter 2, assuming a plume speed of 0.05 m $s^{-1}$ (Sciascia et al. 2013; Josberger and Neshyba 1980). The reference curves show the melt rate parameterizations as a function of the relative ice-ocean velocity for the typical temperatures of the upper and lower layers in the fjord (1°C and 3°C, respectively (Straneo et al. 2010)), for an iceberg of the mean draft $\bar{D}$ in the observational record and aspect ratio 1, where the iceberg draft influences the proportion of the iceberg in each of the warm lower and cool upper fjord layers. The left panel assumes an internal ice temperature $T_i = -4$°C, while the right panel assumes $T_i = -15$°C. It can be seen that the main difference exists between the parameterizations in the attached plume regime, when the relative ice-ocean velocity is less than the plume speed, and that the difference between the parameterizations in this regime is a strong function of the internal ice temperature.

Ocean from ice-sheet and iceberg melt (Bintanja et al. 2013; Merino et al. 2016; Stern et al. 2016), which can promote sea-ice growth, assuming meltwater is deposited in a fresh surface layer and suppresses the upwelling of heat. If iceberg meltwater were instead to enter the water column below the surface, the mixing with warmer water at depth could act to suppress sea ice growth. It is thus of interest to determine whether icebergs generally fall into a regime where their meltwater is channelled directly to the surface via attached side melt plumes, or if meltwater mixes over a broader layer in detached melt plumes. Figure 3.5 shows that some realistic icebergs are likely in the detached plume regime, implying that their meltwater mixes in the downstream

water column over the iceberg draft, while others likely distribute their meltwater in a more undiluted surface layer (or in an intermediate intrusion layer in the case of a strongly stratified ocean) due to having side-attached melt plumes. This motivates the direct observation of iceberg melt plumes to determine their behaviour in the real ocean.

In the laboratory, it was found that at flow speeds less than $\sim 0.4|w|$, meltwater may spread at the surface upstream of the ice block as well as downstream (Figure 3.3A). This agrees with satellite observations of enhanced chlorophyll concentrations (associated with upwelling of nutrient rich water in melt plumes) around giant icebergs in the Southern Ocean. Duprat et al. (2016) observed high chlorophyll concentrations upstream and downstream of large tabular icebergs; an initially counter-intuitive result if one believes meltwater is carried downstream with the flow and there is relatively little vertical shear in the flow. Our results suggest that in low relative velocities (when the iceberg moves predominantly with the ocean currents) it may indeed be possible for meltwater to spread against the background flow due to the buoyancy-driven gravity current generated by surface-pooling of meltwater.

While our study has highlighted the importance of the flow past an iceberg on the iceberg side melt due to the ability of the background flow to interact with icebergs' melt plumes, further work remains. It is anticipated that the aspect ratio of icebergs might influence the strength of side melt plumes if these are fed by basal melt. Consequently, Greenlandic and Antarctic icebergs, which typically have very different aspect ratios, may fall into different melt regimes when subject to the same relative ocean velocity. Furthermore, in this study we have only considered relative velocities and background temperature and salinity profiles that are uniform with depth. How a sheared flow interacts with melt plumes to affect the side melting of icebergs will be the focus of the remainder of this chapter.

## 3.7 Conclusions

Novel laboratory experiments suggested that, for an ice block melting in an non-stratified homogeneous flow, melt plumes are side-attached when the plume velocity is larger than the relative velocity of the flow past the iceberg, and are detached when the relative velocity becomes larger than the plume velocity. The existence of these different regimes results in a nonlinear dependence of the iceberg melt rate on relative velocity. A further important effect of relative velocity on an ice block's melting is where the meltwater is distributed. At speeds low enough that the melt plumes are attached to the ice, the meltwater spreads in an almost undiluted surface layer. At speeds high enough that the melt plumes are detached, the meltwater is diluted downstream of the ice block, and distributed over the ice block draft.

We hypothesize that the transition between attached and detached plume regimes occurs when the magnitude of the relative velocity is of the same order as the melt plume vertical velocity. With this assumption, our updated plume-dependent melt rate parameterization may be scaled up and applied to observed icebergs. For the record of 90 icebergs with concurrent ocean velocity data presented in Chapter 2, the application of this updated parameterization doubles the mean side melt in the attached plume regime, improving agreement with local observations of iceberg melt rates. It is further shown that icebergs may exist in both the attached and detached plume regimes, which may influence whether their meltwater is distributed at the surface or mixed at depth. This motivates further observation of iceberg melt plumes in the ocean to determine their behaviour in flows that may be complicated by the presence of shear and background stratification.

## 3.8 Part II: Ice Melting in a Sheared Flow

For icebergs in an unstratified ocean subjected to a homogeneous flow, the first half of this chapter (FitzMaurice et al. 2017) has shown that if the velocity of the iceberg relative to the water (relative velocity hereafter), $u$, is of greater magnitude than the vertical velocity of its melt plumes $w$, these melt plumes detach from the face of the iceberg allowing the comparatively warm ambient fluid to be in direct contact with the iceberg. Hence, a higher submarine melt rate is observed when the melt plumes are detached compared to when they are attached to the iceberg's face. The transition, occurring when $u \approx w$, from the attached plume regime (in which the iceberg is relatively well insulated from the ambient ocean water) to the detached plume regime (where it is not) produces a highly nonlinear dependence of the side melt rate on the relative flow velocity. Further, this transition corresponds to a change in where the meltwater is distributed, from an almost undiluted surface layer of fresh meltwater in the attached plume regime, to a broad mixed region of meltwater downstream of the iceberg in the detached plume regime. If the meltwater is distributed in an almost undiluted surface layer, we would anticipate a reduced SST and an enhanced sea ice growth in the vicinity of icebergs, whereas if the meltwater is mixed in the water column this effect will be diminished. Thus the contradicting effects of iceberg melt on SSTs and sea ice growth discussed previously may be explained by the different melt plume behaviours, resulting from the influence of a background flow on the iceberg.

The study described in the first half of this chapter considered icebergs melting in a uniform background flow. However, icebergs are unlikely to feel a completely homogeneous horizontal velocity profile over their draft, especially in fjord environments where strongly sheared flows are often present (Straneo et al. 2010; FitzMaurice et al. 2016). Through a series of laboratory experiments, we investigate the behaviour of

iceberg melt plumes in a two-layer vertically sheared flow, with implications for the modelling of iceberg submarine melt rates in the real ocean.

The structure of the remainder of this chapter is as follows. Section 3.9 describes the laboratory setup and methodology, section 3.10 outlines the experimental results, a discussion follows in section 3.11, and conclusions are drawn in section 3.12.

## 3.9 Methods

A re-circulating flume (Figure 3.7) of width 38 cm and length 200 cm (of which the working part was 75 cm long), filled with room temperature (18-21°C) seawater (salinity $S \approx 32$ g kg$^{-1}$), was driven by two separate pumps with flow rates $Q_1$ and $Q_2$. Pump 1 controlled the flow rate of the upper 10 cm of the tank, while pump 2 controlled the flow rate of the lower 20 cm. Each pump could be individually set to one of 4 discrete values to give top and bottom layer flow speeds $u_1$ and $u_2$ of 0, 1.5, 3.3, or 3.7 cm s$^{-1}$. The difference in velocity between $u_1$ and $u_2$ generated a shear instability at the interface between the two layers and induced some mixing, as is the case in the real ocean.

A fresh ice block of height 20 cm was suspended in 30 cm of water, such that half of the ice was in the upper layer and half was in the lower layer (Figure 3.7). The ice block was held fixed so that the flow was equivalent to that observed in the iceberg's frame of reference. Turbulence-suppressing foam and a honeycomb lattice were inserted upstream of the ice block to ensure that the flow was laminar outside of a narrow shear layer between the upper and lower layers.

The ice block was allowed to melt over a period d$T$ =15 minutes, and the resultant mass difference d$W$ (g) was used to calculate a submarine melt rate $M$ (in units of cm min$^{-1}$) using equation 3.3 as in the first half of this chapter. To gain further understanding of where the ice melt occurs, we again analyzed videos of the ice block

melting to split the total submarine melt rate into upstream, downstream, and basal components by tracking the ice edge in each of these regions (i.e. the location of the left, right, and bottom edges, respectively, in the schematics of Figure 3.9). Recall that this methodology only allowed the tracking of the three ice edges in the plane viewed by the video camera, and requires the assumption that melting is spatially uniform in the cross-flow direction (observations of the melted ice block at the end of the experiments confirmed that this is a good assumption, at leading order). The contribution of basal melting to the total melt rate, as calculated from the videos, was removed prior to the analysis to isolate the side submarine melt rate, which is the focus of this study.

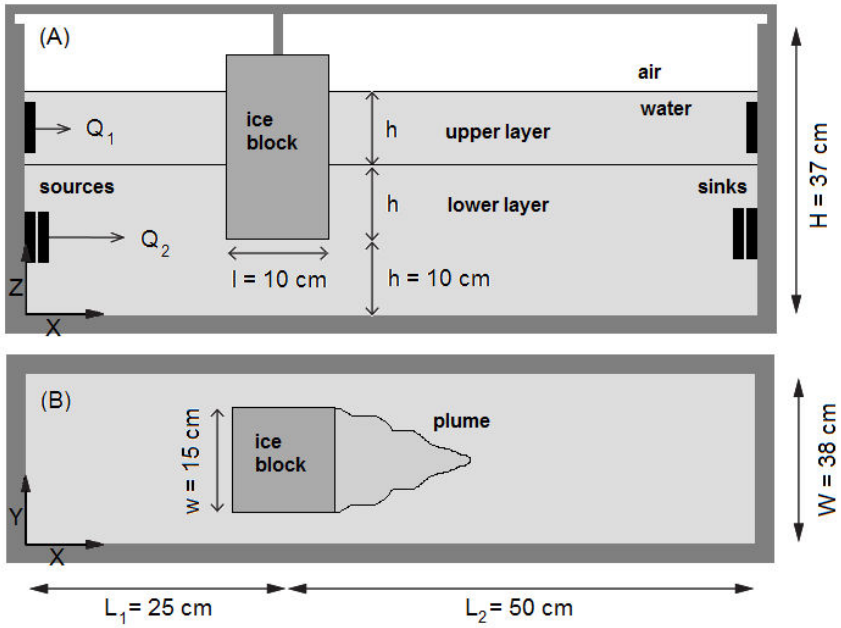



Figure 3.7: A schematic (not to scale) of the laboratory setup for the vertically sheared flow experiments. (A) A side-view of the ice block suspended in the working part of the flume. (B) A birdseye view of the ice block, with a downstream surface layer of melt plume waters.

## 3.10 Results

The study described in the first half of this chapter showed that due to the existence of two distinct regimes, i.e. side-attached and side-detached melt plumes for low and high background flows, respectively, the side melt rate of icebergs has a highly nonlinear dependence on the upstream horizontal flow velocity (black curve in Figure 3.8A). It follows that for an iceberg subject to a vertically sheared flow in which different regimes (side-attached and side-detached) occur over its draft, the side melt rate calculated using the vertically averaged horizontal flow velocity in this nonlinear parameterization will be less than the side melt rate calculated by applying the parameterization at each depth and subsequently averaging. Mathematically, this may be expressed (for an iceberg of draft $D$) as

$$\bar{M} = \frac{1}{D}\int_{-D}^{0} M(u(z))\ \mathrm{d}z \ > \ M\Big(\frac{1}{D}\int_{-D}^{0} u(z)\ \mathrm{d}z\Big) = M(\bar{u}). \tag{3.9}$$

For a two-layer vertically sheared flow, the anticipated average side melt rate $\bar{M}$ will lie at the center of the straight line drawn between the submarine side melt rates, $M(u_1)$ and $M(u_2)$, in each of the two layers (e.g. dashed line and star in Figure 3.8A). However, the laboratory results show that the measured side melt rate in a two-layer vertically sheared flow exceeds even this $\bar{M}$ (Figure 3.8A). Note that allowing for a side melt rate that continuously varies with velocity across the interfacial shear layer (which was calculated to be approximately 5 cm thick) does not significantly alter this result.

The reason for this excess in side melt rate may be understood by considering a phenomenon that was observed to occur when there was no horizontal velocity in the top layer of the flume, and a high horizontal velocity in the bottom layer of the flume. In these experiments, a small semicircular notch of vertical diameter 2-3 cm formed below the waterline across the horizontal extent of the upstream face of the

ice block (Figure 3.9B). The formation of this notch was associated with a rapidly rotating clockwise vortex located against the ice face at this level (Figure 3.9B). It was found that this vortex was a feature generated by the sheared flow encountering an obstacle, and formed near the free surface even when a wooden block (issuing no buoyancy, and no meltwater plume) of the same dimensions as the ice block was positioned in the flume in place of the ice block. The vortex was generated by the lower layer flow being diverted preferentially upwards, instead of solely horizontally around the block, when the upper layer was stationary (Figure 3.9B). When this vertical flow along the upstream face of the block encountered the free surface, it was deflected away from the block and developed a vortex (rotating in a sense counter to that of the primary flow) at the corner between the free surface and the block, which is a previously observed feature of a flow around a corner (e.g. Erturk (2009)).

In the reverse scenario, with a stationary lower layer and a fast-moving upper layer, the flow was likewise observed to be preferentially deflected vertically (this time downwards) into the stationary layer. However, the absence of a free surface at the base of the ice block prevented the formation of a basal notch similar to the surface notch observed in the the vertically reversed case. The three different scenarios (homogeneous flow, faster lower layer, and faster upper layer) are illustrated schematically in Figure 3.9. Note that the mass lost due to the formation of a notch, in the case of slow flow overlying a fast flow, accounts for the higher side melt rates observed in these experiments relative to the equivalent fast flow overlying a slow flow experiments, i.e. the white-topped square symbols in Figure 3.8A have larger submarine side melt rate than the white-bottomed symbols with the same average flow velocity.

This tendency for the flow to deflect vertically (from a fast-flowing layer into a slow-flowing layer) as opposed to horizontally around the ice block when there is vertical shear in the horizontal flow is key to understanding the enhanced melt

rates observed in sheared flows. The presence of a high horizontal velocity in one layer induces the ice surface to experience an enhanced vertical velocity in any more slowly flowing layers, and this raises the mean side melt rate above that predicted by averaging the side melt rates corresponding to each of the upstream layer velocities. This deflection effect may be quantified using the metric

$$\mathrm{d}\tilde{u} = \max\left(u_{\max} - \max(u_{\min}, w), 0\right), \tag{3.10}$$

which is the difference between the fast flow layer speed $u_{\max}$ and the effective speed in the slow flow layer (i.e. the maximum of the slow layer horizontal speed $u_{\min}$ and the vertical plume speed $w$) when this value is positive, and zero otherwise. Figure 3.8B illustrates that the difference $\Delta M$ in submarine side melt rate between the observed and predicted values (once nonlinearity has been accounted for) increases linearly as a function of $d\tilde{u}$, the measure of the effect of flow deflection around the ice block. We non-dimensionalize $\Delta M$ with the average melt rate for the experiment $\bar{M}$, and we non-dimensionalize $\mathrm{d}\tilde{u}$ with the maximum of the two layer velocities $u_{\max}$.

## 3.11 Discussion

The laboratory results presented here suggest that the way ocean currents are deflected around icebergs may have a significant impact on the iceberg side melt rate, via the relative ice-ocean velocity. This effect is likely to be not just a function of the vertical shear in the horizontal velocity profile, but also of the iceberg aspect ratio, and the particulars of its subsurface geometry. For instance, it might be anticipated that for icebergs with a cross-flow horizontal scale that is large relative to their depth, the flow will be preferentially diverted under the ice as opposed to horizontally around it. This could enhance the vertical velocity felt by the upstream ice face or, if the downward flow slows a surface-attached upstream melt plume, decrease it. Such a

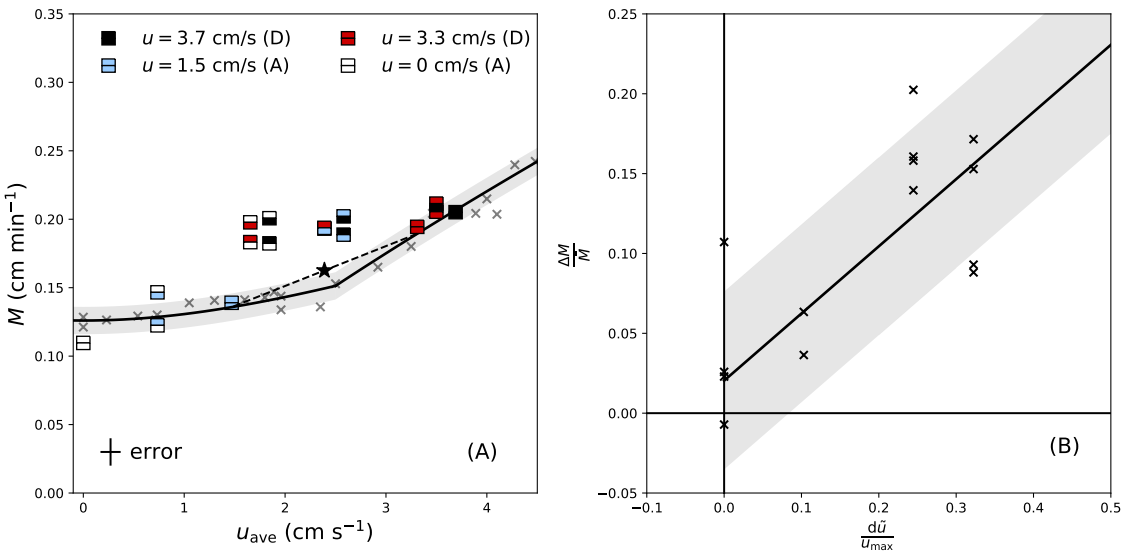



Figure 3.8: (A) Measured submarine side melt rate $M$ in the vertically sheared flow experiments, overlaid on the non-linear parameterization for iceberg side melt in a homogenous flow proposed in the first half of this chapter (FitzMaurice et al. 2017). The coloring of the top and bottom halves of the squares indicates the top and bottom layer velocities in that experiment, varying from 0 cm s$^{-1}$ (white) to 3.7 cm s$^{-1}$ (black). The lettering in the legend indicates which of these velocities would ordinarily be in the attached plume regime (A), and which would be in the detached plume regime (D). The star is the center point of the dashed line between the side melt rates $M(u_{\text{ave}} = 1.5 \text{ cm s}^{-1})$ and $M(u_{\text{ave}} = 3.3 \text{ cm s}^{-1})$, and illustrates that $\bar{M} = \frac{1}{2}\Big(M(u_{\text{ave}} = 1.5 \text{ cm s}^{-1}) + M(u_{\text{ave}} = 3.3 \text{ cm s}^{-1})\Big)$ is lower than the measured side melt rate $M$. (B) Non-dimensionalized difference $\Delta M$ between the measured submarine side melt rate and the submarine side melt rate predicted by averaging the side melt rate in each of the two layers, as a function of the non-dimensionalized difference in the layer speeds $\mathrm{d}\tilde{u} = \max\big(u_{\max} - \max(u_{\min}, w), 0\big)$. $\Delta M$ is non-dimensionalized with the experiment's average melt rate $\bar{M}$, and $\mathrm{d}\tilde{u}$ is non-dimensionalized with the experiment's maximum flow velocity $u_{\max}$. In both (A) and (B), the gray shading indicates the estimated experimental error in the measured side melt rate.

scenario would be of particular relevance to Antarctic icebergs, which generally have a large aspect ratio compared to their Greenlandic counterparts.

Chapter 2 presented observations of icebergs in a fjord environment, which suggest that icebergs move predominantly with the vertical average of the ocean currents (FitzMaurice et al. 2016). Consequently, the flows used to simulate relative iceberg-ocean velocities in the present study are unrealistic in that they do not integrate to

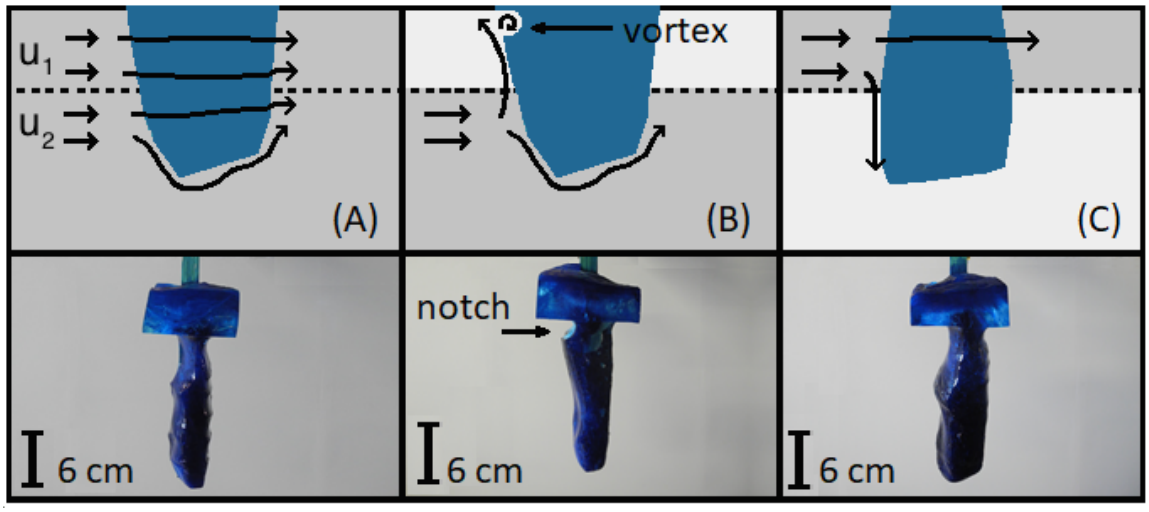



Figure 3.9: Top: Schematic of an ice block in a two-layer vertically sheared flow in which (A) $u_1 = u_2$, (B) $u_1 < u_2$, and (C) $u_1 > u_2$. In (A), the flow is predominantly around the ice block, whereas in (B)/(C) it is deflected up/down into the lower velocity layer. Bottom: Photos of the ice block after 15 minutes of melting for (A) $u_1 = u_2 = 3.3$ cm s$^{-1}$, (B) $u_1 = 0$, $u_2 = 3.3$ cm s$^{-1}$, and (C) $u_1 = 3.3$, $u_2 = 0$ cm s$^{-1}$.

zero over the iceberg draft. However, it is reasonable to assume that the directionality of the flow will only have a second order impact on the ice block melt rate, and as such the flows studied here may be considered analogous to flows in which the layers move at equivalent speeds but in opposite directions, such that the iceberg motion is given by the integrated currents over its draft. A scenario in which there is a relative iceberg-ocean velocity of uniform direction could, of course, be sustained for a grounded iceberg, or for an iceberg not moving with the vertical average ocean currents due, for example, to strong wind forcing.

The shear layer between the upper and lower velocity layers in the present experiments was observed to be approximately 5 cm thick, covering a quarter of the ice block draft of 20 cm. The vertical ocean velocity profiles shown in Figure 3 of FitzMaurice et al. (2016) show a typical shear layer thickness of order 50-100 m in Sermilik Fjord at times during which vertical shear was present in the ocean currents. The draft range of icebergs passing the sensor in that study was 7 m to 490

m. Thus the fraction of the iceberg draft influenced by the shear layer is comparable to that obtained in the laboratory experiments. This is especially true for the largest icebergs in the fjord, which contribute the largest melt flux to the ocean.

The metric $d\tilde{u}$, illustrating the flow deflection around the ice block, when appropriately non-dimensionalized with the maximum background flow speed, can be calculated for the observed relative velocity profiles experienced by icebergs in a Greenlandic fjord in Chapter 2. The shear profiles of these oceanic flows are not entirely analogous to the two-layer laboratory set-up, but by defining the oceanic $d\tilde{u}$ using the maximum and minimum relative ice-ocean velocities over the iceberg draft in equation 3.10 we can make an approximate estimate of the error incurred in parameterizing the melt rates of icebergs in sheared ocean flows. Conducting this analysis, it is found that the average oceanic $d\tilde{u}/u_{\max} = 0.48$, suggesting an average underestimate of the parameterized side melt rate by 21%. Over the full observational dataset, the oceanic $d\tilde{u}/u_{\max}$ varied between 0 and 0.86, resulting in the parameterized melt rate error ranging between 0 and 38% (Figure 3.10).

The magnitude of the melt rate enhancement due to flow deflection seen in this study is anticipated to be dependent on the height reached by the flow when it is deflected vertically by the upstream face of the ice block, which may be reduced by the stratification in the fjord. However, the deflected flow will be mixed with the buoyant water of the melt plume, so we anticipate that the upper bound on the scale height reached by the deflected flow will be the plume's level of neutral buoyancy. There is observational evidence of iceberg melt plumes reaching the ocean surface, and it is thus reasonable to assume that flow deflection effects are important on scales relevant to icebergs in the ocean.

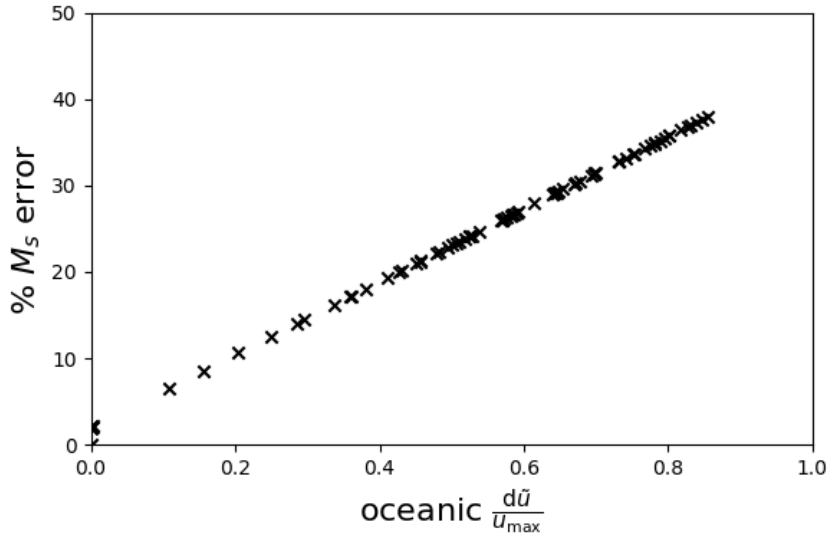



Figure 3.10: The maximum value of the non-dimensionalized oceanic deflection parameter $d\tilde{u}$ (calculated using the maximum and minimum relative ice-ocean velocities over the iceberg draft in equation 3.10) and the corresponding percentage by which the side melt rate $M_s$ may be underestimated due to the neglect of shear for the 90 icebergs observed in the PIES record of Chapter 2.

## 3.12 Conclusions

In the presence of an ambient vertically sheared flow, using the vertically averaged horizontal velocity in the nonlinear iceberg side melt parameterization proposed in the first half of this chapter (FitzMaurice et al. 2017) results in an underestimate of iceberg side melting, particularly when the shear is large. In part, this follows from the nonlinearity of the dependence of side melt on relative velocity if the velocity range spans both the attached and detached regimes (equation 3.9). However, another important contribution is the fact that the iceberg acts as an obstacle to the flow, and as such the horizontal velocity in one layer may influence the flow in a different layer. Hence, even if nonlinearity is taken into consideration by calculating the submarine side melt rate separately in each different layer and subsequently averaging the side melt rates (equation 3.9), the total submarine side melt rate is still underestimated (Figure 3.8A). In particular, if there is a fast flow in one layer and a slow flow in the

other layer, the flow around the ice block ceases to be approximately horizontal and instead is deflected vertically from the high-velocity layer to the low-velocity layer.

The difference between the observed submarine side melt rate and the average of the predicted submarine side melt rates in each of the two layers is found to be a linearly increasing function of a metric of the velocity difference between the layers. Qualitatively, then, the error introduced by not accounting for the flow deflection around an iceberg is likely to be small when the horizontal velocity profile is relatively homogeneous with depth, and large when there is a strong vertical shear. Further studies of flow past an obstacle are required to find the precise value of the correction to the side melt rate that is necessary due to the flow deflection, as it is anticipated that the specifics of this relationship will be a function not just of the vertical shear in the horizontal velocity, but also of the ice block aspect ratio and geometry. The influence of this flow deflection may cause errors of order 20% in an ocean setting (particularly in environments with large vertical shear, such as Greenlandic fjords), but will not be resolved by ocean models that do not explicitly model the flow around icebergs. It is thus important to bear in mind that iceberg melt parameterizations likely underestimate iceberg side melt rates in such scenarios.

Having investigated the parameterization of iceberg side melt rates in a laboratory setting, we now switch our focus to the parameterization of iceberg basal melt rates. Unlike side melt, when iceberg basal melt occurs, the meltwater is confined to spreading horizontally by the iceberg geometry. This makes the simulation of basal melt feasible using a hydrostatic ocean model, which will be the approach taken in the following chapter.

# Chapter 4

# Numerical Simulations: Basal Melt of Tabular Icebergs

## 4.1 Introduction

In the preceding chapters, we have considered iceberg melt rate parameterizations in isolation, and have not addressed the fact that two different parameterizations of glacial ice melting in seawater currently exist, depending on whether the ice is attached to an ice sheet (in the form of an ice shelf) or detached from it (as an iceberg that has calved into the ocean). Within the ice shelf modeling community, the three-equation model of melt (McPhee et al. 1987; Holland and Jenkins 1999) is used, while in iceberg modeling community, bulk melt rate parameterizations (Weeks and Campbell 1973; Bigg et al. 1996; Gladstone et al. 2001; Martin and Adcroft 2010) are employed to circumvent the need to explicitly resolve icebergs in the ocean. However, in both scenarios it is the same physical process, namely the melting of ice in water, that is being represented, and thus the two parameterizations should agree.

As has been previously described, the bulk iceberg melt parameterizations used in current global climate models account for iceberg decay via wave erosion at their

margins, surface melt by the air, and subsurface melt by the ocean (El-Tahan et al. 1987; Savage 2001; Bigg 2016). Of these, the rate of wave erosion is generally the largest, at $0.5 - 1$ m d$^{-1}$ even in calm ocean conditions, followed by the subsurface melt ($\leq 1$ m d$^{-1}$), and then surface melt ($\leq 0.02$ m d$^{-1}$) (Bigg 2016; Savage 2001). The process of edge wasting is parametrized as a continuous decay rate (in units of m d$^{-1}$), and this wave erosion rate is only applied to the iceberg sides, which account for a smaller area than the base for tabular icebergs. In this study, we focus on subsurface melt as opposed to edge wasting since the predominant disagreement between the representation of iceberg and ice shelf decay occurs in the parameterization of subsurface melting. Subsurface melt may further be divided into subsurface side melt and subsurface basal melt, and it is this latter process, thought to be the largest contributer to the total iceberg melt (Bigg 2016), that is the focus of this study.

It was noted in Chapter 2 that the bulk parameterization of basal melt (in units of m d$^{-1}$) is given by

$$M_b = C\frac{(T_o - T_i)|u_o - u_i|^{0.8}}{L^{0.2}}, \tag{4.1}$$

for ocean temperature $T_o$ (°C), ice temperature $T_i$ (generally taken to be constant at $T_i = -4$°C), relative ice-ocean velocity $|u_o - u_i|$ m s$^{-1}$, iceberg length $L$ (m), and dimensional constant $C = 0.58$°C$^{-1}$ m$^{0.4}$ d$^{-1}$ s$^{0.8}$ (Weeks and Campbell 1973; Bigg et al. 1996; Gladstone et al. 2001; Savage 2001; Martin and Adcroft 2010). For the bulk parameterization above, the ocean properties $T_o$ and $u_o$ are typically taken from a single grid cell (Kubat et al. 2007; Martin and Adcroft 2010), although there have been recent modifications to spatially average these properties over the surface area occupied by the iceberg (Rackow et al. 2017). In the standard bulk parameterization, the surface $T_o$ and $u_o$ are used, although some recent models have taken the values of $T_o$ and $u_o$ at the basal depth (Marsh et al. 2015; Merino et al. 2016).

While bulk parameterizations are typically employed to represent the melting of glacial ice that is in the form of icebergs in global climate models, a different

formulation of melting is generally applied to the glacial ice constituting ice shelves. This is the three-equation parameterization of melting (Holland and Jenkins 1999), which comprises equations for the freezing point dependence on pressure and salinity, the conservation of heat, and the conservation of salt. For temperature $T$, salinity $S$, and pressure $P$, these may be expressed as

$$T_b = \alpha S_b + \beta + \delta P_b \tag{4.2}$$

$$\rho_i L_\mathrm{f} M_b = \tfrac{k_i^T}{h}(T_b - T_i) + \gamma_T(T_o - T_b) \tag{4.3}$$

$$\gamma_S(S_b - S_o) = -\rho_i S_b M_b, \tag{4.4}$$

where the subscript $o$ is used to denote far field ocean properties, $b$ denotes boundary layer properties, and $i$ denotes ice properties. The heat transfer coefficient $\gamma_T$ is parameterized as a function of the velocity adjacent to the ice face, and the remainder of the variables are constants, defined in Section 4.4.1. In general, this parameterization is not applied to calculate iceberg melt, although in theory the same physics should apply to this problem as to the melting of sea ice and ice shelves. There have been recent modeling attempts to apply the three-equation parameterization to calculate iceberg melt rates (Rackow et al. 2017), but to date this has been done using far-field properties, without including an iceberg with physical mass in the flow.

In what follows, we use an idealized numerical model to compare the three-equation parameterization of ice shelf melt (Holland and Jenkins 1999) and the bulk parameterization of iceberg basal melt (Weeks and Campbell 1973), in a configuration that explicitly includes an iceberg that acts as an obstacle to the ocean flow in which it is situated. It is found that there are large discrepancies between the bulk formulation of melting and the parameterized three-equation melt rate if the far-field flow properties are used in the bulk formulation. In addition, there is a multiplicative difference between the two parameterizations even when the appropriate

basal properties are used in the bulk parameterization. We find that this difference is a result of the representation of the heat transfer coefficient differing between the two parameterizations. Consequently, an updated bulk basal melt parameterization is proposed, which accounts for the difference between the free flow and basal flow properties and this multiplicative difference.

The structure of this chapter is as follows. The numerical model used and simulations conducted are described in Section 4.2, and the results of these experiments are given in Section 4.3. Section 4.4 is a discussion of the results, in which we compare the theory underlying the three-equation and bulk models of melt to reconcile these two parameterizations, and thus make recommended adaptations to the parameterization of iceberg melt in global climate models. Conclusions follow in Section 4.5.

## 4.2 Methods

### 4.2.1 Ocean Model

We consider GFDL's ocean-only model MOM6 (Hallberg et al. 2013) in an idealized configuration, at 5 km resolution. The domain is a zonally re-entrant channel in a rotating frame (Coriolis parameter $f = -1.4 \times 10^{-4}$ s$^{-1}$) with rigid meridional boundaries, of length $X = 1500$ km, width $Y = 1000$ km, and depth $Z = 1000$ m (Figure 4.1). The flow is forced by a wind stress applied to the ocean surface of the form

$$(\tau_x, \tau_y) = \Big(\tau_0 \sin\big(\frac{\pi y}{Y}\big), 0\Big), \tag{4.5}$$

where $\tau_0 = 0.01$ Pa in the control experiment. The model is spun up for one year from an initial stationary state with a spatially uniform temperature field, of control value $T = 1°$C. The initial salinity field is horizontally uniform and increases linearly with depth, between $S = 32$ PSU at the surface and $S = 38$ PSU at the ocean bed.

### 4.2.2 Ice Model

The iceberg is modeled using GFDL's ice shelf module (Goldberg et al. 2012). This is achieved by holding the position of the iceberg fixed and considering the channel flow to be the relative velocity between the ice and the ocean, in the iceberg's frame of reference. The iceberg is positioned at $(x, y) = (250 \text{ km}, 500 \text{ km})$. The iceberg has a circular cross-section, with edges that slope linearly upwards over a horizontal lengthscale $L_{\text{side}} = 20$ km (Figure 4.1C). For our control simulation we use an iceberg of tabular dimensions, with basal radius $R = 20$ km and maximum draft $D = 400$ m, and internal temperature $T_i = -10°\text{C}$. Due to the large dimensions of the iceberg, the flow beneath it should be similar to that beneath an ice shelf, and so this is an appropriate set-up in which to conduct a comparison of the three-equation parameterization of melting and the bulk parameterization of iceberg basal melt. Iceberg melt is turned off during the model spin-up. Following this period, melt is parameterized by the three-equation model using the in-situ temperature, salinity, and velocity of the flow, but the iceberg shape does not evolve as the melting occurs.

### 4.2.3 Numerical Experiments

A series of numerical experiments are performed to test how the iceberg and ice shelf parameterizations of melt compare in different parameter regimes. In these perturbation experiments we sequentially vary the flow velocity, the ocean and ice temperature, and the iceberg radius (both in absolute terms and relative to the Rossby deformation radius, $R_d \approx 15$ km in the control simulation). The purpose of this is to test the agreement between the in-situ modeled three-equation melt rate (Figure 4.1B), and the melt rate as predicted by the bulk melt rate parameterization (equation 4.1). In the bulk melt rate parameterization, $M_b$ is a function of $|u_i - u_o|$, $T_o$, $T_i$, and $L$. By varying each of these terms in turn, we can assess the agreement of the two different parameterizations of melting across parameter space. In what

follows, diagnostics presented are six-month averages, starting from the second month after melting was turned on, unless otherwise stated.

## 4.3 Results

### 4.3.1 Control Run

Under control conditions, there is an eddying channel flow (Figure 4.1A) that induces downstream cooling and freshening as the iceberg melts (Figure 4.1D). The presence of the iceberg submerged in the flow causes a depression of the isopycnals upstream of the iceberg (Figure 4.1C), as a consequence of the surface wind forcing piling up water against the upstream face of the iceberg. This induces an anticyclonic flow around the iceberg, due to the (southern hemispheric) rotating frame, which in turn leads to the presence of a higher velocity on the southern side than the northern side of the iceberg. The melting of the iceberg is thus asymmetric, with a higher melt rate observed on the southern side of the iceberg than on the northern side (Figure 4.1B). However, the melt rate over the base of the iceberg (inner black circle in Figure 4.1B), which will be the focus of this study, is relatively spatially uniform. The melting of the iceberg results in downstream cooling and freshening at the surface (Figure 4.1D).

### 4.3.2 Perturbation Experiments

#### Varying Flow Velocity

In the first perturbation experiment, we vary the upstream flow speed while holding the ocean temperature $T_o$ and internal ice temperature $T_i$ constant at their control values. We then calculate the in-situ basal melt rate using the three-equation parameterization, and compare this with the bulk melt rate parameterization based on the upstream flow properties (Figure 4.2A). It is found that the melt rate is approx-

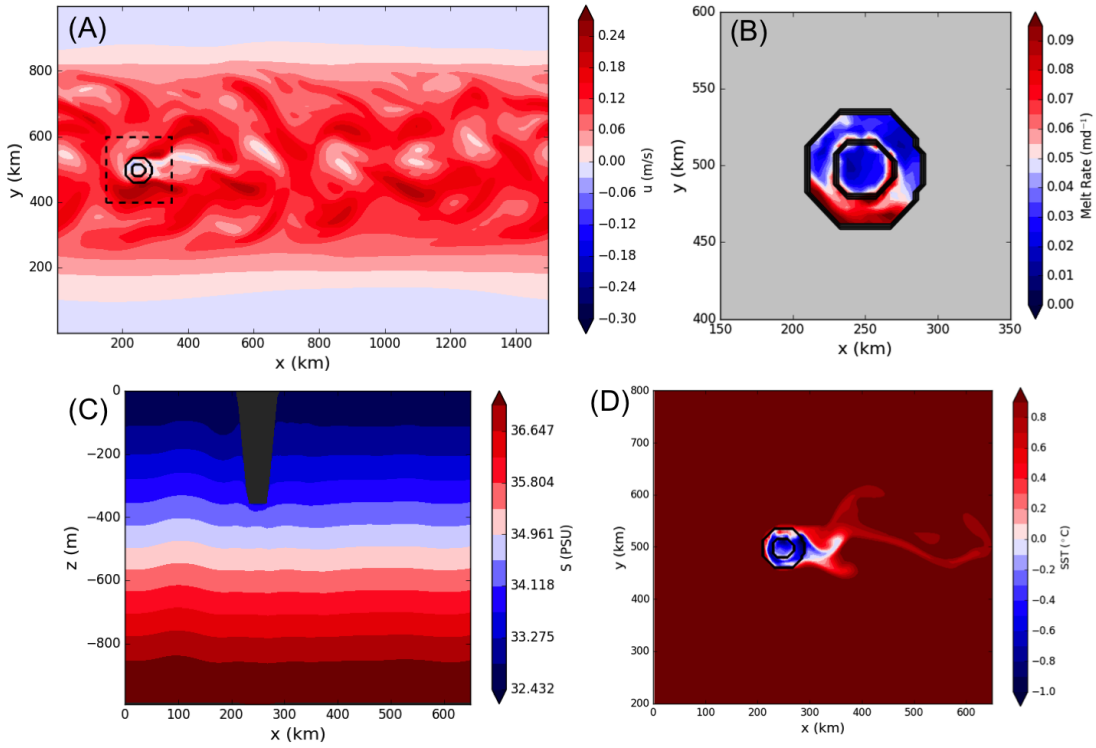



Figure 4.1: (A) A bird's eye snapshot of the modeled channel flow $u$ with an iceberg of radius 20 km situated at $(x, y) = (250, 500)$ km. The inner black ring indicates the location of the flat iceberg base at depth 400 m, and the iceberg sides slope linearly upwards from this to the surface, such that the surface iceberg area is denoted by the outer black ring. The black dashed box indicates the area represented in the right-hand panel. (B) The mean melt rate over the iceberg base and sides as modeled by the three-equation parameterization. (C) A vertical snapshot of the salinity stratification, prior to melting being switched on (the iceberg is masked in gray). (D) Snaphsot of the downstream SST after melting is switched on.

imately constant, independent of the upstream $u$, contradicting the $u^{0.8}$ dependence predicted by the bulk parameterization (equation 4.1).

The numerical configuration employed here allows us to directly examine the basal flow properties, rather than just using the upstream properties as proxies for these values. We consequently re-calculate the bulk parameterization (equation 4.1) using the basal flow speed and the basal temperature. We find that the three-equation melt rate collapses onto this bulk curve (Figure 4.2B) if two modifications are made to the standard bulk formula. Firstly, the ice temperature canonically taken to be

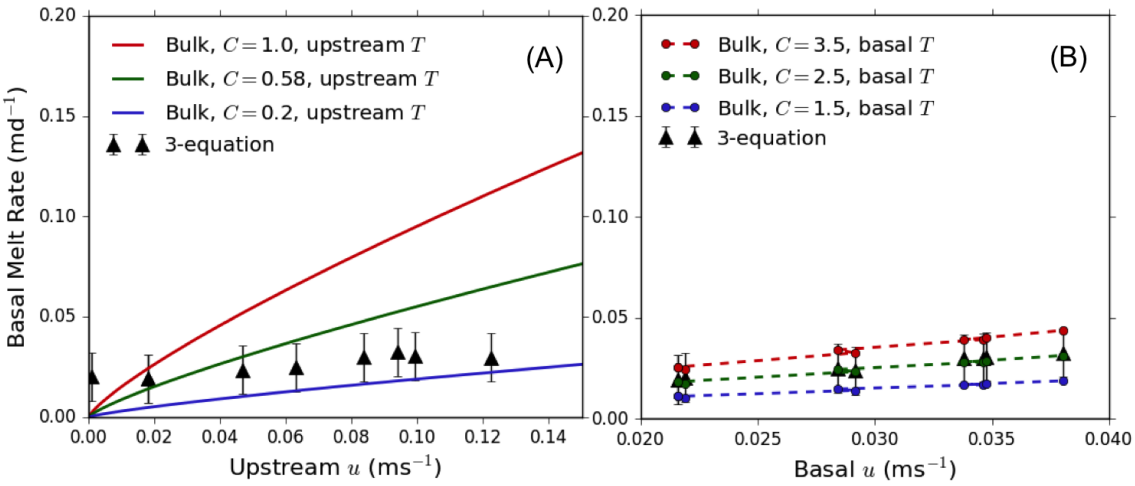



Figure 4.2: (A) The in-situ basal melt rate (triangles) calculated using the three-equation parameterization, plotted as a function of the model-calculated upstream flow speeds. The parameterizations of $M_b$ as a function of speed at different $C$ for an iceberg of radius 20 km melting in a flow at the upstream temperature are shown for reference (solid lines). (B) The in-situ basal melt rate now plotted as a function of the model-calculated basal flow speed and temperature, and the freezing temperature $T_f$ used in place of the ice temperature $T_i$ (dashed lines). The errorbars represent two standard deviations of the melt rate over the six-month duration of the run.

$T_i = -4°\text{C}$ is found to be inappropriate, and instead should be replaced by the in-situ melting temperature of ice. This may be approximated beneath an iceberg (which is generally not at great depth) as $T_f \approx \alpha S_o + \beta$, for $\alpha = -5.73 \times 10^{-2}°\text{C PSU}^{-1}$ and $\beta = 9.39 \times 10^{-2}°\text{C}$, where the upstream basal $S_o$ may be used as an adequate first-order approximation of the basal salinity (Holland and Jenkins 1999). Secondly, the multiplicative constant in the bulk melt rate parameterization, typically taken to be $C = 0.58\ °\text{C}^{-1}\ \text{m}^{0.4}\ \text{d}^{-1}\ \text{s}^{0.8}$, is found to be too low, and instead the three-equation melt rate collapses onto the bulk curve

$$M_b = C\frac{(T_o - T_f)|u_o|^{0.8}}{L^{0.2}}, \tag{4.6}$$

for $C = 2.5\ °\text{C}^{-1}\ \text{m}^{0.4}\ \text{d}^{-1}\ \text{s}^{0.8}$ (Figure 4.2B). Here, the relative ice-ocean velocity $|u_o - u_i| = |u_o|$, as the iceberg is held fixed. The dependence of the basal flow

speed on the upstream flow speed, and the multiplicative difference between the parameterizations are discussed in Section 4.4.

### Varying Ocean and Ice Temperature

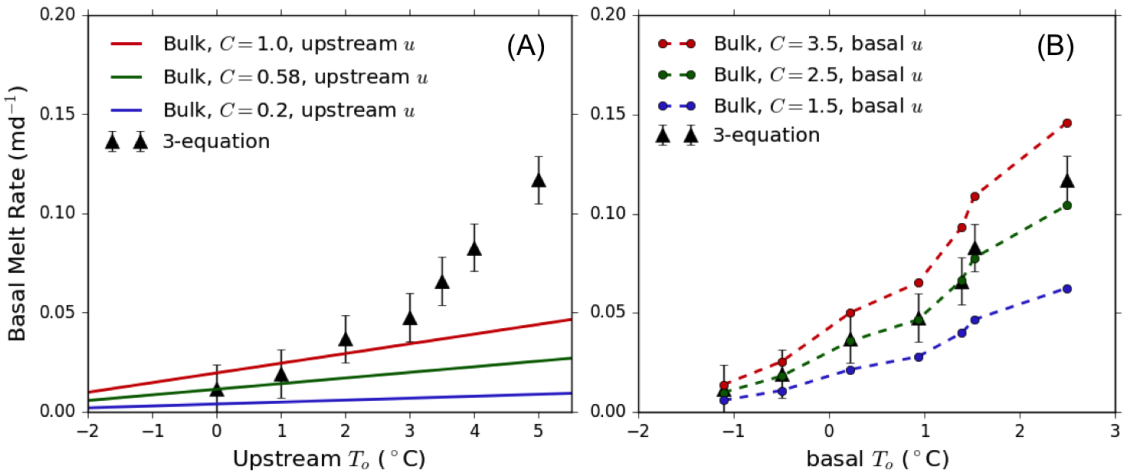



Figure 4.3: (A) The in-situ basal melt rate (triangles) calculated using the three-equation parameterization, plotted as a function of the upstream flow temperature. The parameterizations of $M_b$ as a function of temperature at different $C$ for an iceberg of radius 20 km melting in a flow at the upstream flow speed are shown for reference (solid lines). (B) The in-situ basal melt rate now plotted as a function of the model-calculated basal flow temperature, with reference curves plotted using the model-calculated basal flow speed and temperature, and the freezing temperature $T_f$ used in place of the ice temperature $T_i$ (dashed lines). The errorbars represent two standard deviations of the melt rate over the six-month duration of the run.

We next consider the influence of varying ocean temperature in the range $T_o = 0 - 4°\text{C}$ on the melt rate, holding the upstream flow speed fixed at its control value. It is found that, contrary to equation 4.1, there is a nonlinear dependence of the basal melt rate on the upstream ocean temperature in the parameterized three-equation melt rate (Figure 4.3A). This nonlinear dependence of the melt rate on temperature can be attributed to an increase in the basal flow speed as $T_o$ is increased. This is demonstrated by the fact that the three-equation melt rates collapse onto the bulk melt rate curve given by equation 4.6 for $C = 2.5\ °\text{C}^{-1}\ \text{m}^{0.4}\ \text{d}^{-1}\ \text{s}^{0.8}$ when the basal flow speed, as opposed to the upstream flow speed, is used in this parameteriza-

tion (Figure 4.3B). Again, the ice temperature $T_i$ in this parameterization has been replaced by the in-situ freezing temperature $T_f \approx \alpha S_o + \beta$.

The use of $T_f$ rather than $T_i$ in the bulk parameterization of basal melt is further supported by the fact that when the ocean temperature is held fixed at $T_o = 1°\text{C}$ and the internal ice temperature is varied between $-10$ and $0°\text{C}$ in our numerical simulations, we find that the internal ice temperature has a negligible effect on the three-equation parameterized melt rate. The three-equation parameterization calculates the melt rate from the difference between the heat flux from the ocean to the ice-ocean boundary layer, and the heat flux from the ice-ocean boundary layer into the ice (Section 4.4.1). The agreement of the bulk parameterization with the three-equation parameterization of melt when $T_i$ is replaced by $T_f$ indicates that the contribution of the heat flux from the ice-ocean boundary layer into the ice is small, and it is the heat flux from the ocean into the ice-ocean boundary layer that dominates melting.

### Varying Iceberg Radius

Finally, we consider varying the iceberg basal radius between 5 and 50 km, holding the free flow speed and the ocean temperature fixed at their control values. The bulk parameterization of basal melt (equation 4.1) predicts a length-dependence of $L^{-0.2}$ in the melt rate, but Figure 4.4A illustrates that the three-equation parameterization has a stronger dependence on iceberg radius than this. If, instead, the bulk parameterization is calculated as a function of the average velocity and temperature beneath the iceberg in the numerical model, and $T_i$ replaced with the in-situ freezing temperature $T_f$, the bulk parameterization is a good predictor of the in-situ melt rate for large ($R \geq R_d \approx 15$ km) icebergs, up to the previously discussed multiplicative factor of approximately 5 (Figure 4.4B). At small values of $R$, there is a smaller

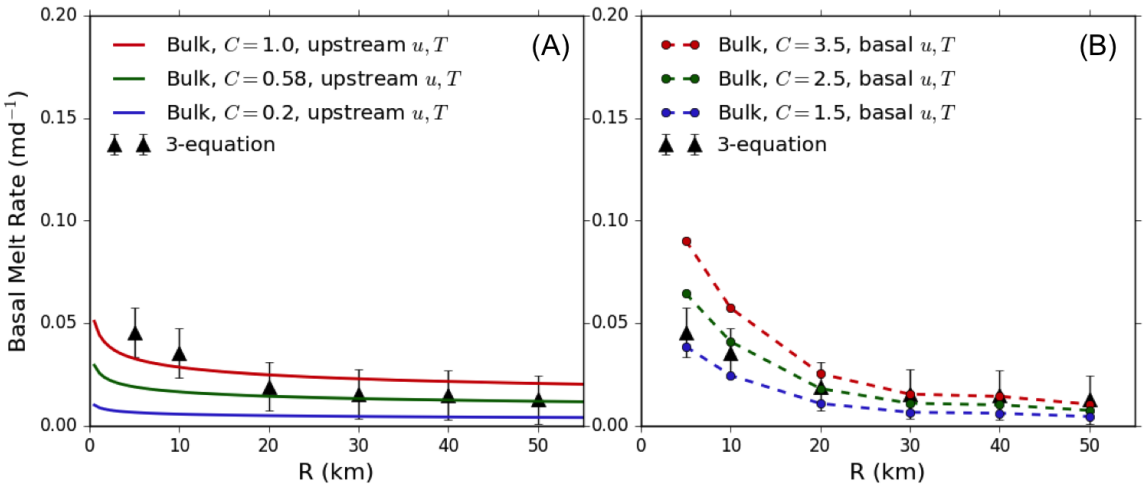



Figure 4.4: (A) The in-situ basal melt rate (triangles) calculated using the three-equation parameterization, plotted as a function of the iceberg radius. The parameterizations of $M_b$ as a function of $R$ at different $C$ for an iceberg melting in a flow at the upstream flow speed and temperature are shown for reference (solid lines). (B) The in-situ basal melt rate again plotted as a function of the iceberg radius, but with reference curves plotted using the model-calculated basal flow speed and temperature, and the freezing temperature $T_f$ used in place of the ice temperature $T_i$ (dashed lines). The errorbars represent two standard deviations of the melt rate over the six-month duration of the run.

multiplicative difference between the two parameterizations. This point is discussed in Section 4.4.1.

### Varying Ocean Stratification and Iceberg Side Slope

Although the ocean stratification and the iceberg side slope do not enter the bulk parameterization of iceberg melt, these properties are of interest because of their potential to influence the conditions downstream of a melting iceberg. In the perturbation experiments, we observed that the melting of the iceberg induced downstream cooling and freshening at the surface. It has been proposed that an iceberg melting in a cold over warm stratification might produce an increase in downstream temperature if the iceberg melt plume entrains sufficient ambient water as it rises (Stern et al. 2017).

We have not succeeded in finding a region in parameter space in which there is warming downstream of the iceberg in our numerical simulations, even in the case of a strong cold-over-warm stratification in the vertical temperature field. This may physically be because however much water a meltwater plume entrains, it entrains more as it rises, so its properties by the time it reaches the surface are dominated by the near-surface $T$ and $S$. However, the degree to which there is downstream cooling and freshening was found to be a function of the iceberg side slope, with steeper iceberg sides resulting in a meltwater layer at the surface that is more diluted by the entrainment of ambient water. In the limiting case of vertical iceberg sides, the downstream temperature and salinity anomaly tended to zero. Given the inability of the hydrostatic numerical model considered here to explicitly simulate vertical melt plumes, the feasibility of downstream warming with a plume-resolving model would be an interesting topic of future study.

## 4.4 Discussion

There are two main points that come out of the analysis in Sections 4.3.2-4.3.2. The first is that there is a multiplicative difference of approximately factor 5 between the bulk parameterization of iceberg melt and the in-situ three-equation parameterized melt rate. The second is that the upstream flow properties $u_o, T_o$ traditionally used in the bulk parameterization to calculate the basal melt rate of icebergs are not representative of the basal flow properties in reality. Figure 4.5 illustrates schematically how the basal flow might be determined by the basal melt plume properties $u_b, T_b$, rather than the upstream flow properties. We address these two points sequentially, first comparing the theory underlying the two melt rate parameterizations in Section 4.4.1 to understand the origin of the multiplicative difference between them, and sub-

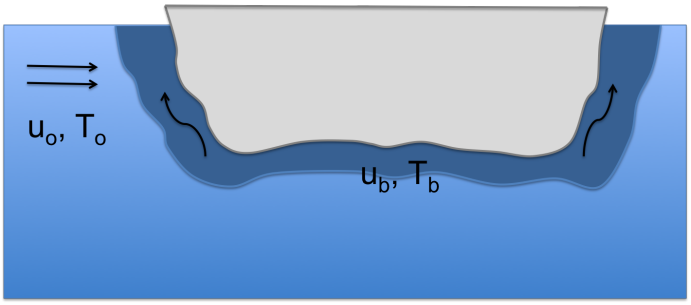



Figure 4.5: A schematic illustrating that it is the basal plume properties $u_b, T_b$ that control an iceberg's melt rate, rather than the upstream free flow properties $u_o, T_o$.

sequently addressing how the basal flow properties might be predicted as a function of the upstream flow properties in Section 4.4.2.

### 4.4.1 Theoretical Comparison of Melt Rate Parameterizations

The parameterization of iceberg basal melt originates from the theory of heat exchange for a finite flat plate in a background flow, which has been an extensively studied problem in engineering since the early twentieth century. The rate of heat exchange is described by the heat transfer coefficient $\gamma_T$, which has units of W m$^{-2}$ K$^{-1}$ and is given by

$$\gamma_T = \frac{k_o^T \bar{\mathrm{Nu}}}{L}, \tag{4.7}$$

where $k_o^T$ is the thermal conductivity of the fluid (W m$^{-1}$ °C$^{-1}$), $L$ is the length of the plate (m), and $\bar{\mathrm{Nu}}$ is the average Nusselt number over the plate. For a flat plate that is sufficiently long for both laminar and turbulent regimes to exist along its length, the average Nusselt number is given by

$$\bar{\mathrm{Nu}} = 0.037\ \mathrm{Re}^{0.8}\ \mathrm{Pr}^{1/3}, \tag{4.8}$$

where Re is the Reynold's number, and Pr is the Prandtl number of the flow (Eckert and Drake 1959).

In a 1973 paper, it was argued (Weeks and Campbell 1973) that the iceberg melt rate could be expressed as $M_b = q/\rho_i L_\mathrm{f}$ where the heat flux is $q = \gamma_T \Delta T$ (here, $\rho_i$ is the density of ice, $L_f$ is the latent heat of fusion, and $\Delta T = T_o - T_i$ is the temperature difference between the ocean and the ice). The authors proceeded by using equation 4.8 above to substitute for $\gamma_T$, and formulated the Reynolds number of the flow as Re= $uL/\nu$, where lengthscale $L$ is the iceberg length (m), velocity scale $u = |u_o - u_i|$ is the relative velocity between the ice and the ocean (m $\mathrm{s}^{-1}$), and $\nu$ is the kinematic viscosity of water ($\mathrm{m}^2$ $\mathrm{s}^{-1}$). Thus,

$$\gamma_T = \frac{0.037 k_o^T \mathrm{Pr}^{1/3}}{\nu^{0.8}} \frac{u^{0.8}}{L^{0.2}}, \tag{4.9}$$

and hence, in units of m $\mathrm{s}^{-1}$,

$$M_b = \Big( \frac{0.037 k_o^T \mathrm{Pr}^{1/3}}{\rho_i L_\mathrm{f} \nu^{0.8}} \Big) \frac{u^{0.8}(T_o - T_i)}{L^{0.2}} \tag{4.10}$$

To convert the above equation to units of m $\mathrm{d}^{-1}$, a multiplicative factor of 86400 must be applied. On applying this factor and substituting for typical polar oceanic values of $k_o^T$, Pr, and $\nu$, equation 4.10 becomes the familiar parameterization of iceberg basal melt (in units of m $\mathrm{d}^{-1}$);

$$M_b = 0.58 \frac{u^{0.8}(T_o - T_i)}{L^{0.2}}, \tag{4.11}$$

where 0.58 is a dimensional constant with units $^\circ\mathrm{C}^{-1}$ $\mathrm{m}^{0.4}$ $\mathrm{d}^{-1}$ $\mathrm{s}^{0.8}$.

The three-equation parameterization was developed specifically for the problem of ice melting in water. It originates from expressions for the freezing point dependence, the conservation of heat, and the conservation of salt (McPhee et al. 1987; Holland

and Jenkins 1999). These may be written as

$$T_b = \alpha S_b + \beta + \delta P_b \tag{4.12}$$

$$q_i^T - q_o^T = q_{\text{latent}}^T = -\rho_i M_b L_{\text{f}} \tag{4.13}$$

$$q_i^S - q_o^S = q_{\text{brine}}^S = \rho_i M_b (S_i - S_b), \tag{4.14}$$

where ocean, boundary layer, and ice properties use subscripts $o$, $b$, and $i$, respectively. Here, $\alpha$, $\beta$, and $\delta$ are constants, the variable $q$ denotes fluxes of heat (superscript $T$) or salinity (superscript $S$), and $L_f$ is again the latent heat of fusion. Note that the melt rate $M_b$ is related to the meltwater flux $w_o$ seen in other studies (Holland and Jenkins 1999) by $\rho_i M_b = \rho_o w_o$. Now,

$$q_{i,o}^T = -\rho_{i,o} c_{pi,o} \kappa_{i,o}^T \frac{\partial T_{i,o}}{\partial z} = -k_{i,o}^T \frac{\partial T_{i,o}}{\partial z} \tag{4.15}$$

(where we have used the fact that conductivity $k$ is related to diffusivity $\kappa$ by $k = \rho c_p \kappa$), so the conservation of heat may be written as

$$-\frac{k_i^T}{h}(T_b - T_i) + k_o^T \frac{\text{Nu}}{h}(T_b - T_o) = -\rho_i M_b L_{\text{f}}. \tag{4.16}$$

Here, Nu allows for turbulence in the boundary layer of thickness $h$. The parameter

$$\gamma_T = k_o^T \frac{\text{Nu}}{h}, \tag{4.17}$$

is the heat transfer coefficient, and is generally parameterized as

$$\gamma_T = \frac{\rho_o c_{po} u^*}{\Gamma_t + \Gamma_m}, \tag{4.18}$$

where $u^* = \sqrt{c_d} u$ is the friction velocity, and the $\Gamma$'s are the turbulent and molecular exchange parameters, respectively. Note that there is varied use of the parameter $\gamma_T$

in the literature, with some studies defining $\gamma_T$ as a heat exchange velocity (units m $s^{-1}$) rather than a true heat transfer coefficient (units W $m^{-2}$ $K^{-1}$), and thus omitting the factor $\rho c_p$ in the equation above (Holland and Jenkins 1999).

Substituting for the heat transfer coefficient and rearranging, equation 4.16 becomes

$$\rho_i L_\mathrm{f} M_b = \frac{k_i^T}{h}(T_b - T_i) + \gamma_T(T_o - T_b). \tag{4.19}$$

Conducting a similar analysis for the conservation of salt, and assuming that $S_i = 0$ (and thus $q_i^S = 0$) gives

$$\gamma_S(S_b - S_o) = -\rho_i S_b M_b, \tag{4.20}$$

where $\gamma_S = \mathrm{Nu}k_o^S/h$ represents the turbulent transfer as salt across the boundary layer, analogously to $\gamma_T$.

All together then, the equations become

$$T_b = \alpha S_b + \beta + \delta P_b \tag{4.21}$$

$$\rho_i L_\mathrm{f} M_b = \tfrac{k_i^T}{h}(T_b - T_i) + \gamma_T(T_o - T_b) \tag{4.22}$$

$$\gamma_S(S_b - S_o) = -\rho_i S_b M_b. \tag{4.23}$$

Note that if we assume that the ice and the boundary layer are at the same temperature and the effects of salinity are negligible, equation 4.22 reduces to

$$\rho_i L_\mathrm{f} M_b = \gamma_T(T_o - T_i), \tag{4.24}$$

which is precisely the equation $M_b = q/\rho_i L_\mathrm{f} = \gamma_T(T_o - T_i)/\rho_i L_\mathrm{f}$ used to derive the bulk melt rate.

Now it becomes clear that the two parameterizations differ primarily in their representation of the heat transfer coefficient, with

$$\gamma_{T,\text{bulk}} = \frac{k_o^T \bar{\text{Nu}}}{L} = \frac{k_o^T 0.037 \text{Pr}^{1/3} u^{0.8}}{\nu^{0.8} L^{0.2}} \tag{4.25}$$

$$\gamma_{T,\text{3EM}} = \frac{k_o^T \text{Nu}}{h} = \frac{\rho_o c_{po} \sqrt{c_d} u}{\Gamma_t + \Gamma_m}. \tag{4.26}$$

The problem of reconciling the bulk and three-equation parameterizations may now be reduced to that of determining the range of validity of the two different representations of $\gamma_T$.

The bulk heat transfer coefficient $\gamma_{T,\text{bulk}}$ was derived empirically from laboratory-scale flows, taking the Reynolds number Re$= uL/\nu$ where $L$ is the characteristic lengthscale of the flow. For flow past a finite body, this characteristic length should be taken as the length of the body, but at some point this ceases to be the appropriate characteristic lengthscale. In the ocean, this is certainly the case when the iceberg is large relative to the Rossby deformation radius. Thus at lengthscales greater than the deformation radius, there is more reason to trust the three-equation heat transfer coefficient. Conversely, the three-equation heat transfer coefficient $\gamma_{T,\text{3EM}}$ assumes fully developed thermal and turbulent boundary layers along the entire ice surface. This is not true at small lengthscales where leading edge effects are important. Thus at small lengthscales, there is more reason to trust that $\gamma_{T,\text{bulk}}$ in the representative heat transfer coefficient.

In between the limiting cases of small $R$ (laboratory scales, where $\gamma_{T,\text{bulk}}$ applies) and large $R$ (scales greater than the deformation radius, where $\gamma_{T,\text{3EM}}$ applies), there should exist a matching region between the two representations of the heat transfer coefficient. An extensive exploration of basal melt rates in this parameter space using either laboratory studies or DNS would be required to find the exact form this matching should take. One such hypothetical matching is illustrated in Figure 4.6.

Comparing the heat transfer coefficients, it is found that there is approximately a factor 5 difference between $\gamma_{T,\text{bulk}}$ and $\gamma_{T,\text{3EM}}$ in the region of parameter space covered by our numerical experiments (star in Figure 4.6). This goes some way towards explaining the discrepancy between the typically used value of $C = 0.58$ $^\circ\text{C}^{-1}$ $\text{m}^{0.4}$ $\text{d}^{-1}$ $\text{s}^{0.8}$, and the value $C = 2.5$ $^\circ\text{C}^{-1}$ $\text{m}^{0.4}$ $\text{d}^{-1}$ $\text{s}^{0.8}$ that is required for the bulk parameterization to agree with the three-equation parameterization in the numerical experiments of Section 4.3. For this experiment, the iceberg radius was greater than the deformation radius and thus outside of the range of validity of the bulk parameterization heat transfer coefficient, suggesting the three-equation melt rate be trusted in this case.

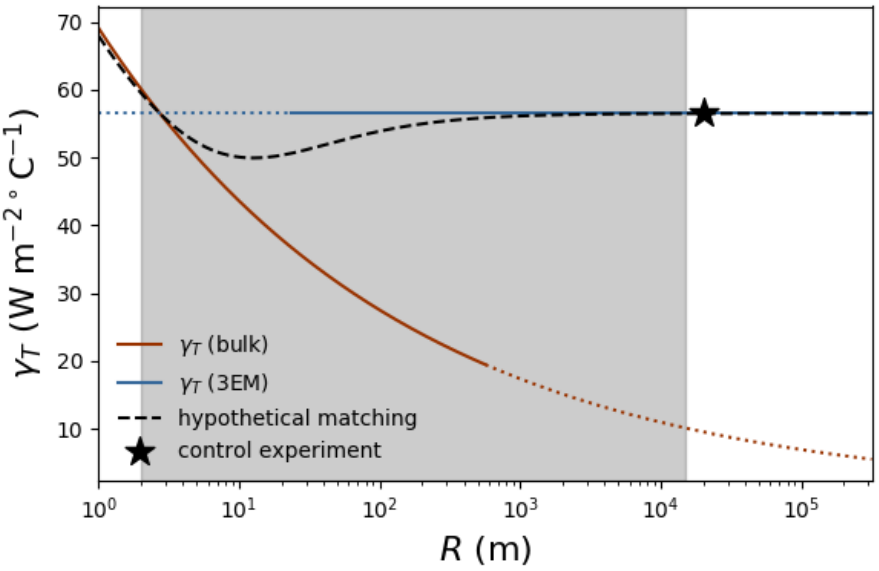



Figure 4.6: A comparison of the three-equation model heat transfer coefficient $\gamma_{T,\text{3EM}}$ (blue line) and the bulk model heat transfer coefficient $\gamma_{T,\text{bulk}}$ (red line) as a function of the iceberg radius $R$ for a flow speed of $u = 0.02$ $\text{ms}^{-1}$. Note that the values of $\gamma_T$ have been scaled by factor 86400 to produce melt rates in units of m $\text{d}^{-1}$. At small $R$, $\gamma_{T,\text{bulk}}$ is more physically relevant, while when $R$ is large (certainly when $R > R_d$), $\gamma_{T,\text{3EM}}$ is more physical. In between, a matching region should exist between the two heat transfer coefficients (gray shading). A hypothetical matching is illustrated by the black dashed line. The black star indicates the location in parameter space of the control numerical experiment conducted in Section 4.3.

### 4.4.2 Dependence of Basal Conditions on Upstream Flow Properties

Even with the correct heat transfer coefficient, the bulk melt rate parameterization requires the correct basal flow properties to be input in order for it to agree with the three-equation parameterization of the melt rate. We thus proceed by considering how the basal flow properties may be determined as a function of the upstream flow properties for the icebergs that we are interested in modeling. In the following subsections, we consider in turn the influence of the upstream flow speed, the upstream temperature, and the iceberg radius on the basal properties (Figure 4.7).

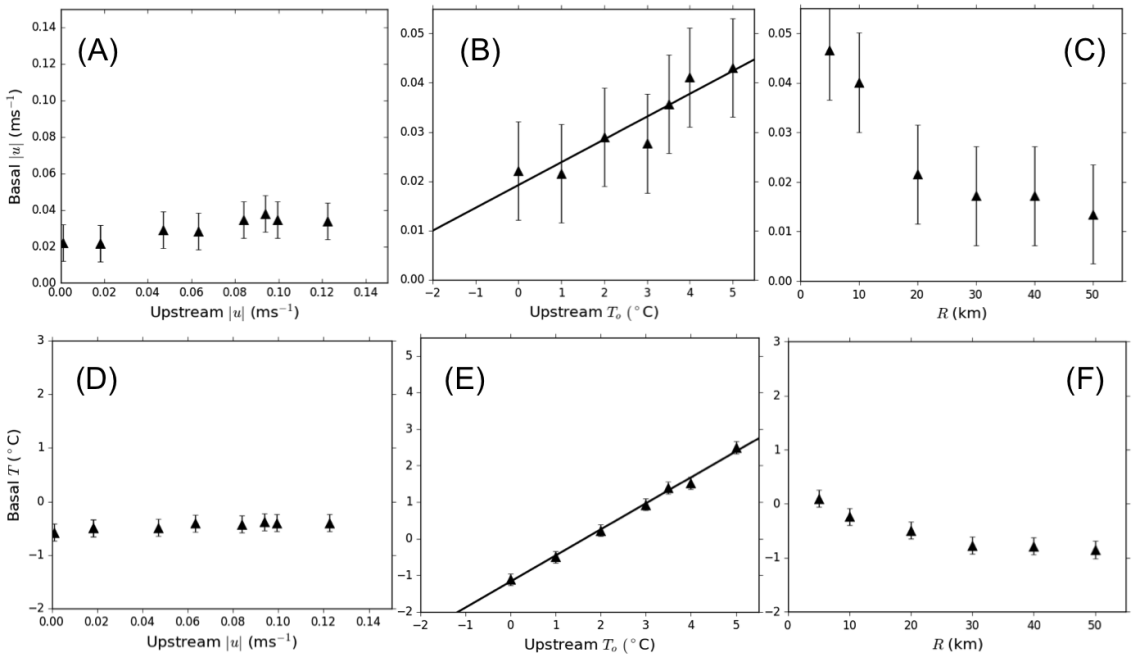



Figure 4.7: Top Row: The average model-calculated iceberg basal speed as a function of (A) the upstream free flow speed, (B) the upstream temperature, and (C) the iceberg radius. Bottom Row: The average model-calculated iceberg basal temperature as a function of (D) the upstream free flow speed, (E) the upstream temperature, and (F) the iceberg radius. The curves in (B) and (E) are the linear lines of best fit. They are described by the equations $u_b = 0.004T_o + 0.02$ and $T_b = 0.7T_o - 1.2$, respectively. In all panels, the errorbars represent two standard deviations of the observed quantity over the six-month duration of the run.

### Dependence on Upstream Flow Speed

The basal flow speed is approximately independent of the upstream flow speed (Figure 4.7A), and the basal temperature is likewise constant at a little over a degree less than the upstream temperature (Figure 4.7D). Key to understanding this is the fact that even at negligible free flow speeds the ice melting causes meltwater to flow outwards under the influence of buoyancy and produce a non-zero velocity at the iceberg base. In addition, the fact that a finite-dimensional iceberg acts as an obstacle to the flow changes the relative velocity between the ice base and the ocean. The blocking effect is enhanced by the fact that icebergs are subject to the influence of rotation, and when they become large relative to the Rossby deformation radius a Taylor column forms under the ice, reducing the relative velocity between the ice and the ocean (Figure 4.8). Thus in a rotating frame of reference, the velocity at the base of the ice is approximately constant at the speed of the meltwater layer.

The resultant melt rate dependence on velocity is comparable to that observed in laboratory studies of the dependence of the side melt rate of ice blocks on a background flow presented in Chapter 3. These experiments found that side melting is controlled by the side melt plume speed when this is higher than the background flow speed. Comparably, this study suggests that the basal melting is controlled by the basal meltwater speed when this is higher than the background flow speed (which is uniformly the case for large icebergs due to the formation of a Taylor column of reduced flow under the iceberg; see Section 4.4.2). However, the relevant velocity is now that of a horizontally spreading gravity current, as opposed to a vertical melt plume speed, so we hypothesize that it will scale as $\sqrt{g'h}$, for reduced gravity $g'$ and meltwater layer thickness $h$ (Vallis 2017).

### Dependence on Upstream Temperature

The basal flow speed is an increasing function of the upstream temperature $T_o$ (Figure 4.7B). The linear best fit to this relationship is

$$u_b = cT_o + d, \tag{4.27}$$

where $c = 0.004 \pm 0.003$ m s$^{-1}$ °C$^{-1}$ and $d = 0.02 \pm 0.01$ m s$^{-1}$. This agrees with the suggestion above that the basal flow speed is that of the meltwater layer, as at higher flow temperatures we would expect more melting, and thus a greater meltwater layer thickness $h$. We would also expect the value of the reduced gravity $g'$ to be greater due to the increased density difference between the meltwater and the ambient water at higher ambient water temperatures. Consequently, we would expect the meltwater layer velocity $\sqrt{g'h}$ to increase with $T_o$.

The basal temperature is related to the upstream temperature by

$$T_b = aT_o + b, \tag{4.28}$$

where $a = 0.7 \pm 0.1$ is dimensionless, and $b = -1.2 \pm 0.1$ °C (line of best fit in Figure 4.7E). This indicates the water in contact with the iceberg base is a mixture of the ambient water at $T = T_o$ and the meltwater with $T = T_f$.

### Dependence on Iceberg Radius

With increasing iceberg radius there is a reduction in the basal flow speed, which begins to level off at $R \approx 15$ km (Figure 4.7C). The reduction in the basal flow speed between $R = 5$ and $R = 15$ km relates to the formation of a Taylor column under the iceberg when as it approaches the scale of $R = 15$ km. We tested the robustness of this attribution by holding the iceberg radius fixed and varying the Coriolis parameter

$f$ in our numerical simulations, and found that the same reduction in basal velocity is seen as the ratio $L/R_d$ increases, where $R_d$ is the Rossby radius of deformation (Figure 4.8D). The formation of the Taylor column can be seen in sections of the zonal velocity as the Coriolis parameter $f$ is varied (Figure 4.8A-C). Once the Taylor column is fully formed, there is minimal contribution to the basal velocity from the upstream flow, and the basal $|u|$ remains constant at the speed of the meltwater layer.

In addition to the reduction in basal velocity with increasing iceberg radius, there is a reduction in the temperature at the base of the iceberg, which begins to level off at $R \approx 15$ km (Figure 4.7F). This may again be attributed to the formation of a Taylor column under the iceberg, as a similar pattern is produced by varying Coriolis parameter $f$ and considering the basal temperature as a function of $L/R_d$ (Figure 4.8E). Physically, the reduction in basal flow with the formation of a Taylor column may be limiting the exchange of ambient water with the water underneath the iceberg and thus resulting in a depressed basal temperature.

### 4.4.3 Restricting Parameter Space

We have seen that introducing an iceberg to a flow influences $u_o$ and $T_o$ at the ice-ocean interface. We have further argued that the bulk parameterization of basal melt is still applicable if the correct flow-adjusted $u_o$ and $T_o$ are used in the parameterization, the correct heat transfer coefficient is used, and the in-situ freezing point $T_f$ is used in place of the ice temperature $T_i$. Over all of parameter space, the basal properties are iceberg lengthscale-dependent functions of the upstream ocean properties

$$u_b = f_L(u_o, T_o) \tag{4.29}$$

$$T_b = g_L(u_o, T_o), \tag{4.30}$$

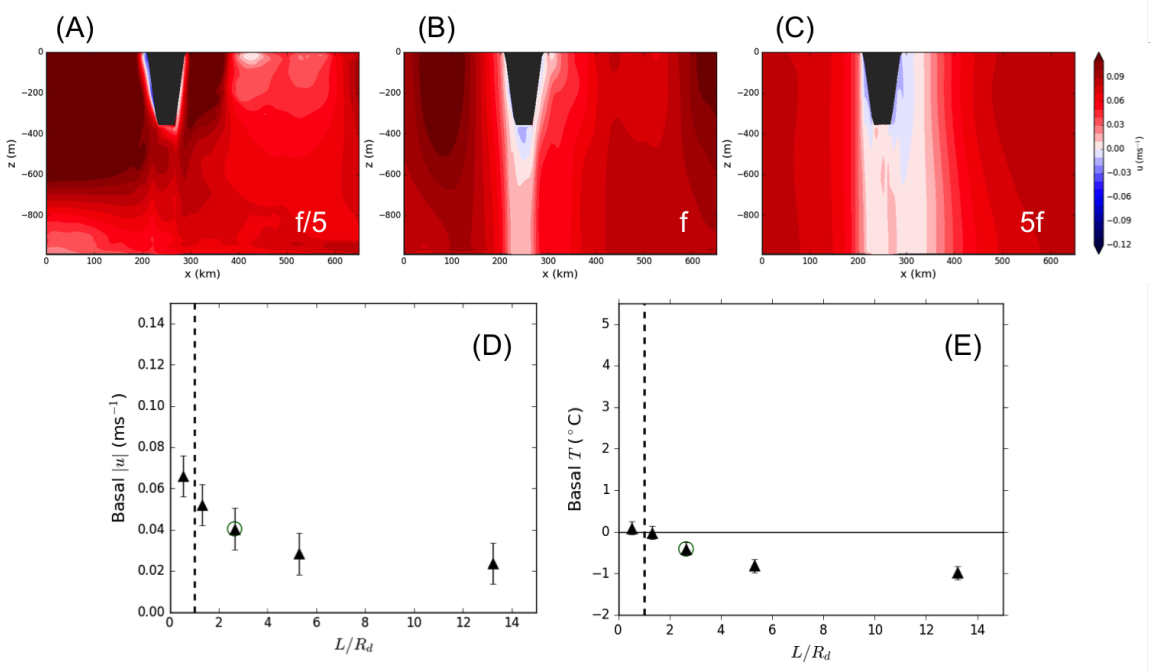



Figure 4.8: Row 1: Side plot of the six-month average zonal velocity field $u$ for $f/5$, control $f$, $5f$. Row 2: The magnitude of the basal velocity (left) and basal temperature (right) as a function of the ratio of the iceberg lengthscale to the Rossby deformation radius $L/R_d$. The Rossby deformation radius $R_d$ is 75 km, 30 km, 15 km, 8 km, and 3 km in the $f/5$, $f/2$, $f$, $2f$, and $5f$ runs, respectively, and the iceberg radius is held fixed at 20 km. The control run $f = -1.4 \times 10^{-4}$ s$^{-1}$ is circled in green in both figures.

and there is an unknown matching function between the bulk and three-equation heat transfer coefficients. So in order to parameterize iceberg melt without explicitly modeling the finite-dimensional iceberg, the two-dimensional functions $f$ and $g$ must be known for all iceberg scales $L$, and the heat transfer coefficient matching function must be known.

Our lack of knowledge of the heat transfer coefficient matching function, in particular, poses a significant barrier to our ability to parameterize iceberg basal melt rates across the full range of iceberg sizes. However, parameter space can be restricted by considering the contribution to total melt from icebergs of different size classes, and limiting our attention to those icebergs that contribute the most to the total melt. Previous studies have used observed iceberg size distributions to deduce the contri-

bution from icebergs of different size classes to the total iceberg area (Tournadre et al. 2016; Stern et al. 2016). A similar argument can be applied to show that the majority of iceberg melt comes from large icebergs, as detailed below.

The probability density function for icebergs of area $A$ is given by

$$p_A(A) \propto A^{-\frac{3}{2}}, \tag{4.31}$$

for $A \in (A_-, A_+) = (10^{-1}, 10^4)$ km$^2$ (Tournadre et al. 2016). We would like to use this distribution to estimate the proportion of melt that comes from icebergs of different radii. We start by changing variables from iceberg area $A$ to iceberg radius $R$ using the change of variables formula for probability density functions

$$p_R(R) = \left| \frac{\mathrm{d}}{\mathrm{d}R}\big(f^{-1}(R)\big) \right| \; p_A\big(f^{-1}(y)\big), \tag{4.32}$$

where $R = f(A) = A^{1/2}$. This gives a probability density function for icebergs of radius $R$ of

$$p_R(R) = p_0 R^{-2}. \tag{4.33}$$

Here, $R \in (R_-, R_+) = (10^{-1/2}, 10^2)$ km, and the constant $p_0$ is chosen as $p_0 = \big(\frac{1}{R_-} - \frac{1}{R_+}\big)^{-1}$, to ensure that the probability density function $p_R$ integrates to 1 over this range. Then to find the proportion of icebergs with radius less than any given value $R_C$ is given by the integral

$$\begin{aligned} \mathrm{prop(icebergs, R < R_C)} &= \textstyle\int_{R_-}^{R_C} \; p_0 R^{-2} \; \mathrm{d}R & (4.34) \\ &= p_0\big(\tfrac{1}{R_-} - \tfrac{1}{R_C}\big). & (4.35) \end{aligned}$$

If we assume that the basal melt flux is proportional to the iceberg basal area, the proportion of *melt* coming from icebergs with radius less than a given value $R_C$ is

given by the area-weighted integral

$$\begin{aligned} \text{prop}(\text{melt}, \text{R} < \text{R}_\text{C}) &= \int_{R_-}^{R_C} p_1 R^{-2} R^2 \, \text{d}R, & (4.36) \\ &= p_1 \big(R_C - R_-\big), & (4.37) \end{aligned}$$

where the constant $p_1 = \big(R_+ - R_-\big)^{-1}$ to ensure that the probability density function $p_1 R^{-2} R$ integrates to 1 over the range of the distribution $R \in (R_-, R_+)$. This is modified to

$$\begin{aligned} \text{prop}(\text{melt}, \text{R} < \text{R}_\text{C}) &= \int_{R_-}^{R_C} p_2 R^{-2} R^{1.8} \, \text{d}R, & (4.38) \\ &= \tfrac{D_2}{0.8} \big(R_C^{0.8} - R_-^{0.8}\big). & (4.39) \end{aligned}$$

if we assume that the melt flux is inversely proportional to $R^{0.2}$, as in the bulk parameterization of basal melt. Again, $p_2 = 0.8\big(R_+^{0.8} - R_-^{0.8}\big)^{-1}$ so that $p_2 R^{-2} R^{1.8}$ integrates to 1 over $(R_-, R_+)$. In fact, the difference between the two parameterizations on the proportion of melt coming from icebergs of different sizes is minimal, and the majority of melt comes from large icebergs, despite these representing a small proportion of the total *number* of icebergs (Figure 4.9).

From the above analysis, 80% of melt comes from icebergs with radii greater than 20 km, even though icebergs of this size represent less than 8 % of all icebergs, and half of all melt comes from icebergs with radii greater than 50 km. Thus, accurately representing the melt of large icebergs is of most importance from a modeling perspective, and we have seen that for these icebergs the basal properties are approximately independent of the iceberg lengthscale (Figure 4.7C,F).

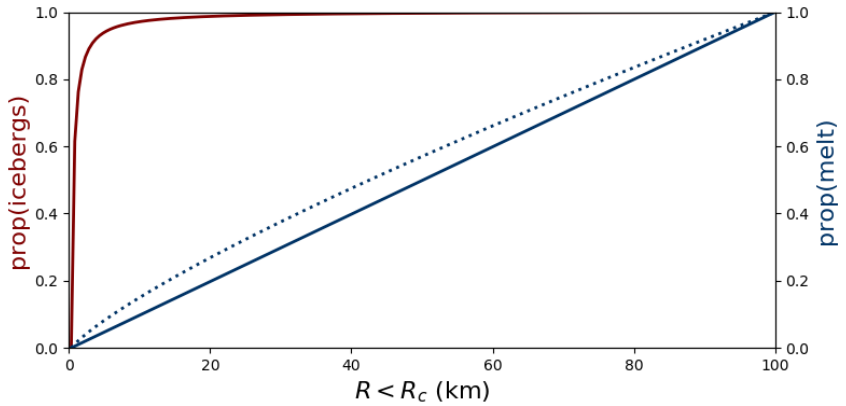



Figure 4.9: The cumulative density function for iceberg number (red) and iceberg melt (blue), as a function of iceberg radius. The solid blue line represents equation 4.37, obtained if a length-independent model of melt such as the three-equation parameterization is used, and the dotted blue line represents equation 4.39, obtained if the bulk parameterization of melting is used. Even though less than 8% of icebergs have radii greater than 20 km, 80% of melt comes from these icebergs, and 50 % of melt comes from icebergs with radii greater than 50 km.

### 4.4.4 Proposed Melt Rate Parameterization Adaptations

Our numerical experiments have shown that the bulk melt rate parameterization agrees with the three-equation parameterization of melting up to a multiplicative factor, provided the correct basal $u, T$ are used, and the ice temperature is replaced by the ocean freezing temperature $T_f$. We have argued that large (radius $R \geq R_d$) icebergs are the dominant contributors to iceberg meltwater, and thus should be the primary focus of modeling efforts. For such icebergs we have seen that the three-equation heat transfer coefficient is more physical than the bulk heat transfer coefficient. Further, for icebergs of this size, the basal flow speed is approximately constant at the meltwater layer speed, and the basal temperature is related to the upstream temperature (in °C) by $T_b = 0.7T_o - 1.2$. The meltwater layer speed (m $s^{-1}$) is related to the upstream temperature (°C) by $u_b = 0.004T_o + 0.02$.

We consequently propose the following for use in calculating the basal melt rate of large ($R \geq R_d$ km) icebergs

$$M_b = \frac{\gamma_T \Delta T}{\rho_i L_f} = \frac{\gamma_{T,3\mathrm{EM}}\big(aT_o + b - T_f\big)}{\rho_i L_f}, \tag{4.40}$$

where $T_f$ is the in-situ freezing temperature, and

$$\gamma_{T,3\mathrm{EM}} = \frac{\rho_o c_{po}\sqrt{c_d}u}{\Gamma_t + \Gamma_m} = \frac{\rho_o c_{po}\sqrt{c_d}(cT_o + d)}{\Gamma_t + \Gamma_m}. \tag{4.41}$$

Here, the heat transfer coefficient has been expressed as a function of the basal flow speed, which is given by $u_b = cT_o + d$. Note that a factor of 86400 would need to be applied to this expression to produce a melt rate in units of m d$^{-1}$ (as opposed to m s$^{-1}$). From the lines of best fit in Figure 4.7, $a = 0.7 \pm 0.1$ (dimensionless), $b = -1.2 \pm 0.1$ °C, $c = 0.004 \pm 0.003$ m s$^{-1}$ °C$^{-1}$, and $d = 0.02 \pm 0.01$ m s$^{-1}$ (equations 4.27-4.28).

For icebergs that are large relative to the deformation radius, this parameterization agrees more closely with the three-equation parameterization of basal melt than the commonly used bulk parameterization (Figure 4.10), particularly as the relative ice-ocean velocity or the ocean temperature become large. In these regimes, the old parameterization may overestimate the basal melt rate by factor $\sim 2$ when $|u_o - u_i| \approx 0.1$ m s$^{-1}$, or underestimate the basal melt rate by factor $\sim 5$ when $T_o \approx 5$°C.

While icebergs that are smaller than the deformation radius are estimated to contribute less than 20% of iceberg melt to the ocean, significant challenges remain if we do wish to accurately parameterize their basal melting. Firstly, it is unclear what form the heat transfer coefficient should take if these icebergs are larger than laboratory dimensions. It is reasonable to assume that some matching exists between the laboratory-scale bulk heat transfer coefficient and the large-scale three-equation

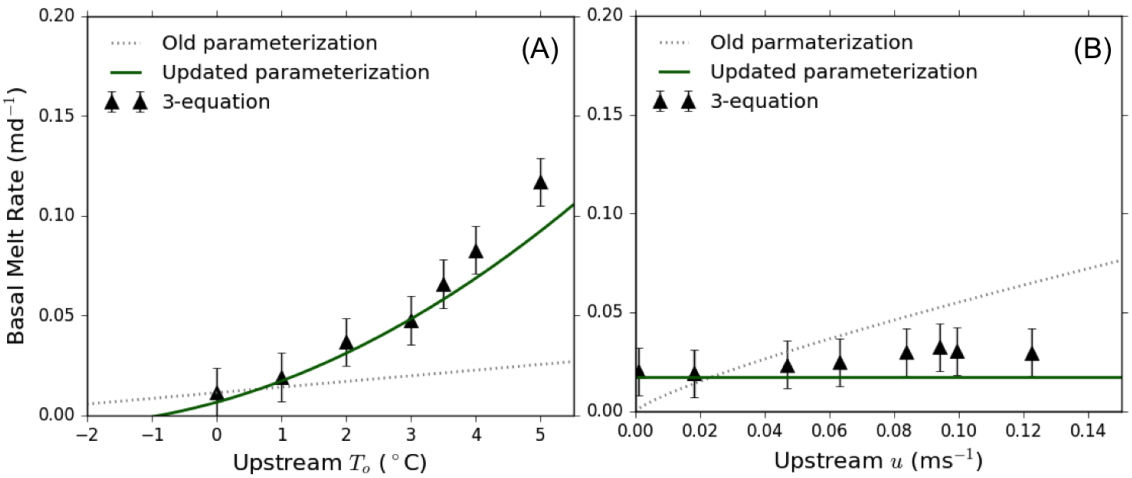



Figure 4.10: A comparison of the updated parameterization of tabular iceberg basal melt (equation 4.40, green solid lines) to the old bulk parameterization of basal melt (equation 4.6, gray dotted lines) and the in-situ melt rate calculated using the three-equation parameterization of melt (black triangles, errorbars representing two standard deviations of the observed quantity over the six-month duration of the run), (A) as the upstream flow speed $u$ is varied, and (B) as the upstream temperature $T_o$ is varied. This parameterization is proposed for use with icebergs that are large relative to the deformation radius.

heat transfer coefficient (Figure 4.6), but further studies are needed to determine the form of this matching. Secondly, even if the heat transfer coefficient were known, the basal flow properties are not lengthscale-independent functions of the upstream flow properties for small ($R < R_d$) icebergs. Thus for each iceberg lengthscale below the deformation radius, both the heat transfer coefficient and the dependence of the basal flow properties on the upstream flow properties must be found in order to parameterize the basal melt rate.

## 4.5 Conclusions

In this chapter, we addressed the fact that there are currently two different parameterizations to represent the melting of ice used in the different communities of ice shelf and iceberg modelers, respectively. The former community uses the temperature, salinity, and velocity fields adjacent to the ice to determine melt rates, and these

fields respond to the injection of meltwater as melting occurs. The latter community relies on bulk parameterizations based on the flow properties that are unaffected by the presence of a melting iceberg, in essence as though the iceberg were levitating above the ocean. These two parameterizations represent the same physical process, namely the melting of ice, and as such should agree across parameter space.

By introducing an iceberg to an idealized re-entrant channel flow using GFDL's ice shelf model, we directly compared the melt parameterized using the three-equation parameterization to that predicted by the bulk parameterization of melt using the upstream flow properties (i.e. the flow unmodified by the physical presence of the iceberg). It was found that there are three sources of discrepancy between the two parameterizations. Firstly, the upstream flow properties are not representative of the basal flow properties when an iceberg occupying physical space is introduced to the flow, and thus the bulk parameterization of basal melt diverges from the three-equation parameterization of melt if the correct basal properties are not used. Secondly, even when the correct basal $u$ and $T$ are applied in the bulk parameterization of melt, there is approximately a factor 5 difference between this and the three-equation parameterization of melt for an iceberg of the control dimensions. Thirdly, the temperature that governs the rate of heat flux from the ocean to the ice is the in-situ freezing temperature $T_f$, rather than the internal ice temperature.

To understand the discrepancy between the melt parameterizations, we returned to the theoretical formulation of the two parameterizations and found that they differ in their representations of the heat transfer coefficient $\gamma_T$. We argued that the use of a Reynolds number based on the lengthscale of the iceberg in the bulk parameterization of melt is inappropriate for tabular icebergs, given their large scale, and that this leads to the observed multiplicative difference between the heat transfer coefficients in the two parameterizations. Conversely, the use of the three-equation heat transfer coefficient would be unphysical at small iceberg scales, for which the

thermal and turbulent boundary layers are not fully formed over the majority of the ice length, and leading edge effects are still important to the mean melt rate. A matching between the two representations of the heat transfer coefficient is required at intermediate scales, and remains an important topic of future study.

In the absence of a known matching between the heat transfer coefficients, we proceeded by restricting our consideration to large icebergs ($R > R_d$), which we showed probabilistically to be the dominant contributers of iceberg melt to the ocean. Due to the formation of a Taylor column under such icebergs, we found that the basal flow speed was approximately independent of the upstream flow speed, and instead was simply a linear function of the ambient water temperature. The basal temperature was likewise a linear function of the upstream temperature. We thus propose an updated parameterization to calculate the basal melt rate of tabular icebergs (equation 4.40), which is independent of the upstream flow speed, and which is based on the (more physical at this scale) three-equation heat transfer coefficient.

Finally we noted that there is downstream cooling and freshening at the surface associated with the melting of an iceberg with physical size in these numerical runs. However, the degree to which this cooling and freshening occurs is a function of the iceberg side slope, with the downstream SST and SSS anomalies tending to zero as the iceberg slope becomes infinite. This leaves reason to suppose that downstream warming may have been possible if the model had explicitly resolved vertical, entraining melt plumes. The occurrence of calving at an iceberg's margins is likely to result in iceberg side slopes being sufficiently steep that a hydrostatic ocean model will not be able to resolve the iceberg's side melt plumes. This is in contrast with the melt plumes underneath ice shelves, which typically have a shallow horizontal slope, except at the calving face of the ice shelf.

# Chapter 5

# Conclusion

## 5.1 Summary of Findings

The mass flux to the ocean from the Greenland and Antarctic ice sheets comprises surface melt leaving the ice sheets as runoff and subglacial discharge, subsurface melt where the ice meets the ocean, and the calving of icebergs directly into the ocean. Of these processes, iceberg calving constitutes a combined annual mass flux of roughly 1800 $km^3$ to the ocean (Enderlin et al. 2014; Depoorter et al. 2013), and as such icebergs act as a significant distributed source of freshwater as they are carried away from their source regions and melt along their trajectories. Where and how icebergs melt has the potential to affect both ocean stratification and local productivity (through, for example, the upwelling of nutrient-rich water) (Smith et al. 2007; Duprat et al. 2016). Despite the regional nature of such effects, they have implications for the large-scale ocean circulation and sequestration of carbon by the ocean (Böning et al. 2016; Sgubin et al. 2017), which makes understanding iceberg melting a priority in a globally warming climate.

The focus of this work has been improving the parameterization of iceberg melting in GCMs, through a combination of observational, experimental, and numerical stud-

ies. In Chapter 2, we began by processing the output of an acoustic sensor (PIES) located in Sermilik Fjord, southeast Greenland, to obtain a record of speed and draft for 90 icebergs that passed over the sensor during its seven-month deployment. A concurrent record of the along-fjord currents was collected from an ADCP stationed within 2 km of the PIES, and a record of the along-fjord winds was obtained from a local weather station. This provided a large observational dataset with which to assess the role of the ocean and the atmosphere in forcing icebergs in the fjord.

It was found that a rudimentary one-dimensional force balance model reproduced the observed iceberg speeds to a good degree of accuracy (with correlation coefficient $r = 0.8$ between modeled and observed iceberg speeds). The influence of the iceberg shape (conical or cuboid) on this correlation was negligible, and the model results were consistent with the standardly used values of the oceanic and atmospheric drag coefficients. The oceanic term dominated the atmospheric term in explaining the variation in the observed iceberg speeds. It is common practice in GCMs to only use surface ocean properties to calculate iceberg motion and melt rates, but a comparison between the iceberg speeds calculated using the surface currents in the fjord and those calculated using the ocean velocity profile over the entire iceberg draft revealed an average error of 60% in the modeled iceberg speed under this modeling simplification. Under this same simplification, the average error in the basal melt rate was 71%.

Having observed the importance of vertical variations in ocean currents on iceberg motion and melt rates, we proceeded to conduct an experimental study of the response of ice side melt rates to a background flow. Physically, the melting of icebergs differs from that of sea ice, marine-terminating glacier faces, or ice shelves, in the ability of the flow to pass around the body of an iceberg. We found that this produced a previously unobserved nonlinearity in the dependence of iceberg side melt rates on a background flow, as a consequence of the interaction between the background flow and the vertically rising melt plume. At low background flow speeds, melt plumes

are attached to the face of the melting ice, insulating it from the ambient water. However, when the horizontal background flow speed becomes large relative to the vertical plume speed, the melt plume separates from the face of the ice, allowing the ambient water into contact with the ice face and increasing the side melt rate.

The newly observed nonlinear dependence of ice side melt rates on a background flow was used to update the standardly used iceberg side melt rate parameterization. This new parameterization agrees closely with the standard parameterization in the detached plume regime, but predicts a non-zero melt rate as the background flow speed is reduced to zero, in contrast to the existing parameterization. On applying the new parameterization to the observational record of icebergs presented in Chapter 2, it was found that icebergs exist both in a predominantly attached and in a predominantly detached plume regime. Further, the new parameterization predicted a doubling in the mean melt rate within the attached plume regime.

In addition to the laboratory-measured effect of the background flow on the ice melt rate, it was observed that the regime transition that occurred as the background flow was increased altered how the meltwater was distributed in the water column. In the detached plume regime, the meltwater was broadly mixed in the water column downstream of the ice, as opposed to being funneled into a relatively undiluted surface layer, as was the case in the attached plume regime. This result is of especial interest as it pertains to modeling the impact of iceberg melt on upwelling, sea surface temperature, and sea surface salinity, and is thus relevant to predicting the occurrence of oceanic biological blooms and the formation of sea ice.

While our initial experiments considered ice melting in a homogeneous vertical velocity profile, it was observed in Chapter 2 that icebergs may experience considerable shear in the ocean currents over their draft. Given the existence of two different regimes of melting for ice in the presence of a homogeneous background flow depending on the horizontal flow speed relative to the vertical ice melt plume speed, the effect

of vertical shear in the horizontal velocity on ice melt rates is nontrivial. We thus introduced a novel laboratory set-up to investigate the effect of a two-layer shear flow on ice melting. Our experiments revealed that ice melting in such a flow experiences a side melt rate greater than that predicted, even accounting for the nonlinearity in the updated side melt rate parameterization. We showed that this is a consequence of the flow being deflected vertically on encountering a vertical ice face when there is large vertical shear in the background horizontal velocity profile, which increases the relative ice-ocean velocity in the more slowly flowing layer. Scaling this effect to the observations presented in Chapter 2 indicates that neglecting flow deflection may result in the underestimation of iceberg side melt rates by order 20%.

Having assessed the parameterization of iceberg side melting using laboratory experiments, Chapter 4 considered the basal melt rate of tabular icebergs. The large scale of the tabular icebergs of interest when considering basal melt, and the hydrostatic nature of flow beneath such icebergs, enabled this problem to be approached using numerical simulations with GFDL's ocean model MOM6. In particular, we considered whether the three-equation parameterization standardly applied to calculate melt rates beneath sea ice and ice shelves agrees with the bulk parameterization of iceberg basal melt, when the flow beneath tabular icebergs is directly simulated.

We found that the bulk parameterization of basal melt can be made qualitatively consistent with the three-equation parameterization of melting if the correct basal flow speed and temperature are used, and the in-situ freezing temperature is used in place of the ice temperature in the forced convection equation. However, the two parameterizations still differ quantitatively due to their different representations of the heat transfer coefficient. We argued that the three-equation parameterization's representation of the heat transfer coefficient is more appropriate at scales of relevance to tabular icebergs, but a matching is needed between the two heat transfer coefficients to accurately represent iceberg melting across parameter space. We fur-

ther presented functional dependencies of the basal flow speed and basal temperature underneath icebergs of tabular dimensions for use in the bulk formulation of iceberg melting.

In summary, then, this thesis proposes that the following updated parameterizations be used to calculate iceberg melt rates in GCMs. The side melt rate (most applicable to non-tabular icebergs, with length $L$ the same order of magnitude as draft $D$) should be calculated, in units of m d$^{-1}$, as

$$M_s = \begin{cases} \dfrac{0.58|w|^{0.8}(\alpha T_o - T_i)}{D^{0.2}} & |u_o - u_i| \leq |w| \\ \dfrac{0.58|u_o - u_i|^{0.8}(T_o - T_i)}{L^{0.2}} & |u_o - u_i| > |w|, \end{cases} \tag{5.1}$$

where $\alpha = \frac{1}{\sqrt{2}w}\sqrt{u^2 + w^2}$, for relative ice-ocean velocity $u = |u_o - u_i|$ and plume speed $w \approx 0.05$ m s$^{-1}$. This choice of $\alpha$ ensures continuity in the parameterization at $|u_o - u_i| = |w|$. The ocean and ice temperatures $T_o$ and $T_i$ are in °C, the iceberg draft $D$ and length $L$ are in m, and the constant 0.58 has dimensions °C$^{-1}$ m$^{0.4}$ d$^{-1}$ s$^{0.8}$. We caution that this may underestimate the melt rate by order 20% in flows with large vertical shear due to the dynamics of flow-splitting around the iceberg in these cases. The basal melt rate (most applicable to tabular icebergs with $L >> D$), again in units of m d$^{-1}$, is

$$M_b = \frac{\gamma_T \Delta T}{\rho_i L_f} = \frac{\gamma_{T,\mathrm{3EM}}\big(aT_o + b - T_f\big)}{\rho_i L_f}, \tag{5.2}$$

where $T_f$ is the in-situ freezing temperature, and

$$\gamma_{T,\mathrm{3EM}} = \frac{\rho_o c_{po}\sqrt{c_d}u}{\Gamma_t + \Gamma_m} = \frac{\rho_o c_{po}\sqrt{c_d}(cT_o + d)}{\Gamma_t + \Gamma_m}. \tag{5.3}$$

Here, $a = 0.7 \pm 0.1$ (dimensionless), $b = -1.2 \pm 0.1$ °C, $c = 0.004 \pm 0.003$ m s$^{-1}$ °C$^{-1}$, $d = 0.02 \pm 0.01$ m s$^{-1}$, and $T_f$ is the in-situ freezing temperature. We further

have shown evidence that the meltwater should be distributed in an undiluted surface layer when the relative ice-ocean velocity is $u < w \approx 0.05$ m s$^{-1}$, and mixed in a layer as deep as the iceberg draft otherwise. These recommended modifications are practically implementable in GCMs, and will improve the ability of such models to assess the effects of iceberg discharge on local and global ocean properties.

## 5.2 Implications

The result of this work is a set of concrete recommendations for the representation of icebergs in GCMs. We must consider the full vertical velocity profile to determine an iceberg's motion, and account for the nonlinear dependence of the submarine melt rate on this background velocity to accurately predict the iceberg's melt rate. This melt rate is further modified by the deflection of the flow around the iceberg, and this comes into its own when the iceberg is large relative to the Rossby deformation radius, and the formation of a Taylor column reduces the flow under the iceberg. In general, the presence of melt plumes spreading along the iceberg base and vertically up the iceberg sides creates a lower bound on the relative velocity between the ice and the ocean, and thus on the submarine melt rate. By taking a probabilistic approach to the observed distribution of icebergs, we were able to determine that our primary focus should be on large (radius $R \geq R_d$) icebergs, and by considering such icebergs in a numerical model, we determined a relationship between the upstream flow properties and the basal conditions for such icebergs, and used this to propose a modified parameterization of iceberg melt.

Future work should focus on implementing the parameterizations given in equations 5.1 and 5.2 in GCMs, and studying the effects of these modified melt parameterizations on physical and biological ocean properties. Allowing for the mixing of meltwater in the water column down to the draft of the iceberg in the detached plume

regime will likely reduce the surface freshening and surface temperature depression associated with iceberg melt. This may limit sea ice growth, which is promoted by the existence of undiluted cold, fresh meltwater at the surface. The rate of iceberg melt is also of interest, as this determines how far icebergs travel from their calving locations before entirely disintegrating, and thus controls the areal extent of icebergs' influence on the ocean. Chapter 4 showed that current iceberg meltrate parameterizations likely overestimate basal meltrates in strong background flows, as they do not account for the formation of Taylor columns underneath large icebergs, but that current parameterizations significantly underestimate basal meltrates in warm ocean conditions, due to their misrepresentation of the heat transfer coefficient. This latter effect will presumably act to limit the lifespan of icebergs if they drift equatorward from their source regions, and thus locally restrict the emission of iceberg meltwater. In particular, this may limit the ability of meltwater from Greenlandic icebergs to cap deep convection sites in the North Atlantic. These ramifications are speculative at present, and merit further investigation via the implementation in GCMs of the parameterizations presented here.

While this thesis has focused on the melting of icebergs in the ocean, it may be considered representative of a methodology that may be applied to understand and represent any of the multitude sub-gridscale processes whose effects influence global climate. Firstly, we began by observing icebergs, and placing leading order constraints on their behavior. This informed the development of laboratory studies that enabled us to develop a physical understanding for how icebergs melt in a background flow. Armed with this knowledge, we were able to configure a numerical model to simulate this melting and the subsequent distribution of meltwater in the water column, and propose improved iceberg melt parameterizations for use in GCMs.

The complexity of climate is such that we must be able to represent processes across disparate scales to project with any degree of accuracy the potential outcomes

of anthropogenic climate change. The melt of an individual iceberg may, quite literally, be a drop in the ocean, but that drop has a host of knock-on effects; from influencing the sea ice cover and thus planetary albedo, to promoting phytoplankton blooms and the sequestration of atmospheric carbon by the ocean. No single tool can fully elucidate such a complex system. Rather, we must combine the different approaches available to us; observation, experimentation, and modeling, to incrementally improve our understanding, and better assess our influence as a species on the planet.

# Bibliography


Andres, M., Silvano, A., Straneo, F., and Watts, D. R. Icebergs and sea ice detected with inverted echo sounders. *Journal of Atmospheric and Oceanic Technology*, 32 (5):1042–1057, 2015.

Bamber, J., den Broeke, M., Ettema, J., Lenaerts, J., and Rignot, E. Recent large increases in freshwater fluxes from greenland into the north atlantic. *Geophysical Research Letters*, 39(19), 2012.

Bigg, G. *Icebergs: their science and links to global change*. Cambridge University Press, 2016.

Bigg, G. R., Wadley, M. R., Stevens, D. P., and Johnson, J. A. Prediction of iceberg trajectories for the north atlantic and arctic oceans. *Geophysical research letters*, 23(24):3587–3590, 1996.

Bigg, G. R., Wadley, M. R., Stevens, D. P., and Johnson, J. A. Modelling the dynamics and thermodynamics of icebergs. *Cold Regions Science and Technology*, 26(2):113–135, 1997.

Bintanja, R., Van Oldenborgh, G., Drijfhout, S., Wouters, B., and Katsman, C. Important role for ocean warming and increased ice-shelf melt in antarctic sea-ice expansion. *Nature Geoscience*, 6(5):376–379, 2013.

Böning, C. W., Behrens, E., Biastoch, A., Getzlaff, K., and Bamber, J. L. Emerging impact of greenland meltwater on deepwater formation in the north atlantic ocean. *Nature Geoscience*, 9(7):523–527, 2016.

Budd, W., Jacka, T., and Morgan, V. Antarctic iceberg melt rates derived from size distributions and movement rates. *Annals of Glaciology*, 1(1):103–112, 1980.

Cenedese, C. and Gatto, V. M. Impact of two plumes interaction on submarine melting of tidewater glaciers: a laboratory study. *Journal of Physical Oceanography*, 46(1):361–367, 2016.

Depoorter, M. A., Bamber, J., Griggs, J., Lenaerts, J., Ligtenberg, S. R., Van den Broeke, M., and Moholdt, G. Calving fluxes and basal melt rates of antarctic ice shelves. *Nature*, 502(7469):89, 2013.

Duprat, L. P., Bigg, G. R., and Wilton, D. J. Enhanced southern ocean marine productivity due to fertilization by giant icebergs. *Nature Geoscience*, 9(3):219–221, 2016.

Eckert, E. and Drake, R. *Heat and Mass Transfer*. McGraw, 1959.

El-Tahan, M., Venkatesh, S., and El-Tahan, H. Validation and quantitative assessment of the deterioration mechanisms of arctic icebergs. *Journal of Offshore Mechanics and Arctic Engineering*, 109(1):102–108, 1987.

Enderlin, E. M., Howat, I. M., Jeong, S., Noh, M.-J., Angelen, J. H., and Broeke, M. R. An improved mass budget for the greenland ice sheet. *Geophysical Research Letters*, 41(3):866–872, 2014.

Enderlin, E. M., Hamilton, G. S., Straneo, F., and Sutherland, D. A. Iceberg meltwater fluxes dominate the freshwater budget in greenland's iceberg-congested glacial fjords. *Geophysical Research Letters*, 43(21), 2016.

Enderlin, E. and Hamilton, G. Estimates of iceberg submarine melting from high-resolution digital elevation models: application to sermilik fjord, east greenland. *Journal of Glaciology*, 60(224):1084–1092, 2014.

Erturk, E. Discussions on driven cavity flow. *International Journal for Numerical Methods in Fluids*, 60(3):275–294, 2009.

FitzMaurice, A. and Stern, A. Parameterizing the basal melt of tabular icebergs. *Ocean Modelling*, Submitted.

FitzMaurice, A., Straneo, F., Cenedese, C., and Andres, M. Effect of a sheared flow on iceberg motion and melting. *Geophysical Research Letters*, 43(24), 2016.

FitzMaurice, A., Cenedese, C., and Straneo, F. Nonlinear response of iceberg side melting to ocean currents. *Geophysical Research Letters*, 44(11):5637–5644, 2017.

FitzMaurice, A., Cenedese, C., and Straneo, F. A laboratory study of iceberg side melting in vertically sheared flows. *Journal of Physical Oceanography*, Under Review.

Gade, H. G. When ice melts in sea water: A review. *Atmosphere-Ocean*, 31(1): 139–165, 1993.

Gladstone, R. M., Bigg, G. R., and Nicholls, K. W. Iceberg trajectory modeling and meltwater injection in the southern ocean. *Journal of Geophysical Research: Oceans*, 106(C9):19903–19915, 2001.

Goldberg, D., Little, C., Sergienko, O., Gnanadesikan, A., Hallberg, R., and Oppenheimer, M. Investigation of land ice-ocean interaction with a fully coupled ice-ocean model: 1. model description and behavior. *Journal of Geophysical Research: Earth Surface*, 117(F2), 2012.

Hallberg, R., Adcroft, A., Dunne, J. P., Krasting, J. P., and Stouffer, R. J. Sensitivity of twenty-first-century global-mean steric sea level rise to ocean model formulation. *Journal of Climate*, 26(9):2947–2956, 2013.

Hanna, E., Navarro, F. J., Pattyn, F., Domingues, C. M., Fettweis, X., Ivins, E. R., Nicholls, R. J., Ritz, C., Smith, B., Tulaczyk, S., et al. Ice-sheet mass balance and climate change. *Nature*, 498(7452):51, 2013.

Helly, J. J., Kaufmann, R. S., Stephenson, G. R., and Vernet, M. Cooling, dilution and mixing of ocean water by free-drifting icebergs in the weddell sea. *Deep Sea Research Part II: Topical Studies in Oceanography*, 58(11):1346–1363, 2011.

Hill, J. C. and Condron, A. Subtropical iceberg scours and meltwater routing in the deglacial western north atlantic. *Nature Geoscience*, 7(11):806, 2014.

Hobbs, W. R., Massom, R., Stammerjohn, S., Reid, P., Williams, G., and Meier, W. A review of recent changes in southern ocean sea ice, their drivers and forcings. *Global and Planetary Change*, 143:228–250, 2016.

Hobson, B. W., Sherman, A. D., and McGill, P. R. Imaging and sampling beneath free-drifting icebergs with a remotely operated vehicle. *Deep Sea Research Part II: Topical Studies in Oceanography*, 58(11):1311–1317, 2011.

Holland, D. M. and Jenkins, A. Modeling thermodynamic ice–ocean interactions at the base of an ice shelf. *Journal of Physical Oceanography*, 29(8):1787–1800, 1999.

Huppert, H. E. and Turner, J. S. Ice blocks melting into a salinity gradient. *Journal of Fluid Mechanics*, 100(2):367–384, 1980.

Jackson, R. H., Straneo, F., and Sutherland, D. A. Externally forced fluctuations in ocean temperature at greenland glaciers in non-summer months. *Nature Geoscience*, 7(7):503, 2014.

Josberger, E. G. and Neshyba, S. Iceberg melt-driven convection inferred from field measurements of temperature. *Annals of Glaciology*, 1(1):113–117, 1980.

Kubat, I., Sayed, M., Savage, S. B., Carrieres, T., et al. An operational model of iceberg drift. *International Journal of Offshore and Polar Engineering*, 15(02), 2005.

Kubat, I., Sayed, M., Savage, S. B., Carrieres, T., Crocker, G., et al. An operational iceberg deterioration model. In *The Seventeenth International Offshore and Polar Engineering Conference*. International Society of Offshore and Polar Engineers, 2007.

Lüthi, M. P. and Funk, M. Modelling heat flow in a cold, high-altitude glacier: interpretation of measurements from colle gnifetti, swiss alps. *Journal of Glaciology*, 47(157):314–324, 2001.

Marsh, R., Ivchenko, V., Skliris, N., Alderson, S., Bigg, G. R., Madec, G., Blaker, A. T., Aksenov, Y., Sinha, B., Coward, A. C., et al. Nemo–icb (v1. 0): interactive icebergs in the nemo ocean model globally configured at eddy-permitting resolution. *Geoscientific Model Development*, 8(5):1547–1562, 2015.

Marshall, J. and Plumb, R. A. *Atmosphere, ocean and climate dynamics: an introductory text*, volume 21. Academic Press, 2016.

Martin, T. and Adcroft, A. Parameterizing the fresh-water flux from land ice to ocean with interactive icebergs in a coupled climate model. *Ocean Modelling*, 34 (3):111–124, 2010.

McConnochie, C. D. and Kerr, R. C. The turbulent wall plume from a vertically distributed source of buoyancy. *Journal of Fluid Mechanics*, 787:237–253, 2016.

McPhee, M. G., Maykut, G. A., and Morison, J. H. Dynamics and thermodynamics of the ice/upper ocean system in the marginal ice zone of the greenland sea. *Journal of Geophysical Research: Oceans*, 92(C7):7017–7031, 1987.

Merino, N., Le Sommer, J., Durand, G., Jourdain, N. C., Madec, G., Mathiot, P., and Tournadre, J. Antarctic icebergs melt over the southern ocean: Climatology and impact on sea ice. *Ocean Modelling*, 104:99–110, 2016.

Mernild, S. H., Hansen, B. U., Jakobsen, B. H., and Hasholt, B. Climatic conditions at the mittivakkat glacier catchment (1994–2006), ammassalik island, se greenland, and in a 109-year perspective (1898–2006). *Geografisk Tidsskrift-Danish Journal of Geography*, 108(1):51–72, 2008.

Mountain, D. On predicting iceberg drift. *Cold Regions Science and Technology*, 1 (3-4):273–282, 1980.

Neshyba, S. and Josberger, E. G. On the estimation of antarctic iceberg melt rate. *Journal of Physical Oceanography*, 10(10):1681–1685, 1980.

Oltmanns, M., Straneo, F., Seo, H., and Moore, G. The role of wave dynamics and small-scale topography for downslope wind events in southeast greenland. *Journal of the Atmospheric Sciences*, 72(7):2786–2805, 2015.

Rackow, T., Wesche, C., Timmermann, R., Hellmer, H. H., Juricke, S., and Jung, T. A simulation of small to giant antarctic iceberg evolution: Differential impact on climatology estimates. *Journal of Geophysical Research: Oceans*, 122(4):3170–3190, 2017.

Rignot, E., Box, J., Burgess, E., and Hanna, E. Mass balance of the greenland ice sheet from 1958 to 2007. *Geophysical Research Letters*, 35(20), 2008.

Rignot, E., Velicogna, I., van den Broeke, M. R., Monaghan, A., and Lenaerts, J. T. Acceleration of the contribution of the greenland and antarctic ice sheets to sea level rise. *Geophysical Research Letters*, 38(5), 2011.

Robinson, N. and Williams, M. Iceberg-induced changes to polynya operation and regional oceanography in the southern ross sea, antarctica, from in situ observations. *Antarctic Science*, 24(5):514–526, 2012.

Ruddiman, W. F. *Earth's Climate: past and future*. Macmillan, 2001.

Russell-Head, D. The melting of free-drifting icebergs. *Annals of glaciology*, 1(1): 119–122, 1980.

Savage, S. Aspects of iceberg deterioration and drift. *Geomorphological Fluid Mechanics*, pages 279–318, 2001.

Sciascia, R., Straneo, F., Cenedese, C., and Heimbach, P. Seasonal variability of submarine melt rate and circulation in an east greenland fjord. *Journal of Geophysical Research: Oceans*, 118(5):2492–2506, 2013.

Sgubin, G., Swingedouw, D., Drijfhout, S., Mary, Y., and Bennabi, A. Abrupt cooling over the north atlantic in modern climate models. *Nature Communications*, 8, 2017.

Smith, K. L., Robison, B. H., Helly, J. J., Kaufmann, R. S., Ruhl, H. A., Shaw, T. J., Twining, B. S., and Vernet, M. Free-drifting icebergs: hot spots of chemical and biological enrichment in the weddell sea. *science*, 317(5837):478–482, 2007.

Smith, S. D. Hindcasting iceberg drift using current profiles and winds. *Cold regions science and technology*, 22(1):33–45, 1993.

Srokosz, M., Baringer, M., Bryden, H., Cunningham, S., Delworth, T., Lozier, S., Marotzke, J., and Sutton, R. Past, present, and future changes in the atlantic meridional overturning circulation. *Bulletin of the American Meteorological Society*, 93(11):1663–1676, 2012.

Stephenson, G. R., Sprintall, J., Gille, S. T., Vernet, M., Helly, J. J., and Kaufmann, R. S. Subsurface melting of a free-floating antarctic iceberg. *Deep Sea Research Part II: Topical Studies in Oceanography*, 58(11):1336–1345, 2011.

Stern, A., Adcroft, A., and Sergienko, O. The effects of antarctic iceberg calving-size distribution in a global climate model. *Journal of Geophysical Research: Oceans*, 121(8):5773–5788, 2016.

Stern, A., Adcroft, A., Sergienko, O., and Marques, G. Modeling tabular icebergs submerged in the ocean. *Journal of Advances in Modeling Earth Systems*, 2017.

Straneo, F., Hamilton, G. S., Sutherland, D. A., Stearns, L. A., Davidson, F., Hammill, M. O., Stenson, G. B., and Rosing-Asvid, A. Rapid circulation of warm subtropical waters in a major glacial fjord in east greenland. *Nature Geoscience*, 3 (3):182–186, 2010.

Straneo, F., Curry, R. G., Sutherland, D. A., Hamilton, G. S., Cenedese, C., Våge, K., and Stearns, L. A. Impact of fjord dynamics and glacial runoff on the circulation near helheim glacier. *Nature Geoscience*, 4(5):322, 2011.

Sutherland, D. A., Roth, G. E., Hamilton, G. S., Mernild, S. H., Stearns, L. A., and Straneo, F. Quantifying flow regimes in a greenland glacial fjord using iceberg drifters. *Geophysical Research Letters*, 41(23):8411–8420, 2014.

Tournadre, J., Bouhier, N., Girard-Ardhuin, F., and Rémy, F. Antarctic icebergs distributions 1992–2014. *Journal of Geophysical Research: Oceans*, 121(1):327–349, 2016.

Vallis, G. K. *Atmospheric and oceanic fluid dynamics*. Cambridge University Press, 2017.

Weeks, W. F. and Campbell, W. Icebergs as a fresh-water source: an appraisal. *Journal of Glaciology*, 12(65):207–233, 1973.

Yankovsky, A. E. and Yashayaev, I. Surface buoyant plumes from melting icebergs in the labrador sea. *Deep Sea Research Part I: Oceanographic Research Papers*, 91: 1–9, 2014.

Zickfeld, K., Levermann, A., Morgan, M. G., Kuhlbrodt, T., Rahmstorf, S., and Keith, D. W. Expert judgements on the response of the atlantic meridional overturning circulation to climate change. *Climatic Change*, 82(3-4):235–265, 2007.